Advanced Implant Encapsulation Concept with Integrated Humidity-Monitoring Sensor

Von der Fakultät für Ingenieurwissenschaften,
Abteilung Elektrotechnik und Informationstechnik
der Universität Duisburg-Essen

zur Erlangung des akademischen Grades

Doktor der Ingenieurwissenschaften

genehmigte Dissertation

von

Özgü Dogan, M.Sc.

aus

Hildesheim

1. Gutachter: Prof. Dr.-Ing. Holger Vogt
2. Gutachter: Prof. Dr. rer. nat. Wilfried Mokwa

Tag der mündlichen Prüfung: 11.07.2019

DOI: 10.17185/duepublico/70711
URN: urn:nbn:de:hbz:464-20201207-075729-1

Dedicated to my parents.

Acknowledgement

Firstly, I would like to express my sincere gratitude to my advisor Prof. Vogt for the continuous support of my Ph.D. study and for his patience and immense knowledge. His guidance helped me in all the time of research and writing of this thesis. Besides, I would like to thank Prof. Mokwa sincerely for his interest and support in my thesis and related research.

My special thanks also go to my colleagues Dr. Christian Walk, Michael Knier, Dr. Jens Weidenmüller, Peter Fürst, Dr. Pierre Gembaczka, Dr. Nicolas Schierbaum, Prof. Karsten Seidl and my supervisor Michael Görtz for the insightful comments, stimulating discussions and their precious support.

I thank all my fellow labmates in the cleanroom for their support and experienced advice for my process- or hardware-related issues. My special thanks go to Dr. Dorothee Dietz, responsible engineer for the ALD system, who always had time for discussions and sacrificed many hours on the development of experimental and non-conventional ALD processes with me.

Thank you very much, Marina Wirtz and Renate Kirtz, for the your help and support with the SEM images. Your patience was remarkable while preparing and mocroscoping my samples.

My thanks also go to my colleagues from the doctoral coaching team headed by Dr. Hartwig Junge. The constructive advice, as well as the mutual encouragement in a friendly atmosphere were a great help to me. I also want to thank Rowena Potthoff for the linguistic corrections and suggestions for improvement.

Last but not the least, I would like to thank my parents, my brother and my sisters for their emotional support. Each one of them always had an open ear and loving words of encouragement for me throughout working on this thesis.

Abstract

Subject of this work is the development of an advanced encapsulation concept for active implants which features an all-around enclosing humidity-monitoring sensor layer with a hermetic sealing. The encapsulation consists of functional thin-films deposited by CVD and ALD. Due to the high isotropy of these deposition methods, each layer encloses the surface of the substrate so that a miniaturised 3D encapsulation is achieved.

The substrate, a fully assembled implant, is coated with a 3 to 5 µm thick parylene F layer which isolates the electronic components and smooths sharp edges on the substrate as a preparation for following thin-film depositions. For the sensor layer, a sandwich type structure with resistive sensing mechanism is chosen. Two metal layers surround the humidity-sensitive film as electrodes. ALD composites of semiconducting ZnO and dielectric Al_2O_3 grains are developed as the sensitive film. For this purpose, the phenomenon of island growth at small numbers of deposition cycles is used. Various ZnO to Al_2O_3 ratios are evaluated with test structures which are exposed to water droplets. Adsorption of water molecules at the grain boundaries leads to a significant decrease in total resistivity of the composite. This sensitive behaviour is proven by measured current and respectively resistance changes of up to five orders of magnitude. Electrical connection between the electrode layers and respective contact pads on the substrate are attained through openings in the insulating parylene F and ALD composite layers. Local removal of these insulating films is achieved by laser ablation with a 355 nm UV laser. A biocompatible and ceramic Ta_2O_5 film encloses the whole implant as final and hermetic layer of the encapsulation stack.

Single developments of this work are presented and evaluated. Additionally, three-dimensional implementation of the concept is demonstrated with all-around encapsulated substrates which are tested both in the dry and immersed condition. While undamaged encapsulations demonstrate constant resistance values, some structures with damaged encapsulations, such as scratches, reveal resistance decreases by 74 % in case of immersion. Thus, even small defects in the hermetic sealing can be detected. The results of this work prove the feasibility of a hermetic implant encapsulation with humidity-detecting function as a self-monitoring feature.

Zusammenfassung

Gegenstand dieser Arbeit ist die Entwicklung eines Verkapselungskonzepts für aktive Implantate mit einer umschließenden, feuchteüberwachenden Sensorschicht mit hermetischer Versiegelung. Die Verkapselung besteht aus funktionalen dünnen Schichten, welche mittels CVD und ALD Verfahren abgeschieden werden. Durch die hohe Isotropie dieser Abscheideverfahren umschließt jede Schicht die Implantatoberfläche, sodass eine miniaturisierte 3D-Verkapselung erzielt wird.

Das Substrat, ein bestücktes Implantat, wird zunächst mit Parylene F beschichtet, welches die elektronischen Komponenten isoliert und scharfe Kanten des Substrats als Vorbereitung für weitere Dünnfilmabscheidungen ebnet. Für die Sensorschicht wird ein Sandwich-artiger Aufbau mit resistivem Sensormechanismus bevorzugt. Zwei Metalllagen umschließen die feuchteempfindliche Schicht und agieren als Elektroden. Sensitive ALD-Gemische mit halbleitenden ZnO- und dielektrischen Al_2O_3-Körnern werden mithilfe des Inselwachstums bei wenigen ALD Zyklen entwickelt. Diverse ZnO zu Al_2O_3 Verhältnisse werden mithilfe von Teststrukturen evaluiert, welche Wassertropfen ausgesetzt werden. Durch die Adsorption von Wassermolekülen an den Korngrenzen steigt die elektrische Leitfähigkeit des Gemisches, sodass Strom- bzw. Widerstandänderungen um fünf Größenordnungen messbar sind. Die elektrische Kontaktierung der Elektroden mit entsprechenden Pads auf dem Substrat erfolgt durch lokale Öffnungen in den isolierenden Parylene F und ALD Schichten. Diese Öffnungen werden durch ein Laser-Ablationsverfahren mit einem 355 nm UV-Laser fabriziert. Ein biokompatibler und keramischer Ta_2O_5-Film umschließt das ganze Implantat und dient als finale und hermetische Schicht des Verkapselungsstapels.

Einzelne Entwicklungen dieser Arbeit sind präsentiert und evaluiert. Die 3D-Implementierung des Konzepts wird mithilfe von rundum verkapselten Substraten demonstriert, welche im trockenen und im eingetauchten Zustand getestet werden. Während Widerstandswerte bei unbeschadeten Verkapselungen konstant bleiben, zeigen einige Strukturen mit kleinen Defekten in der Verkapselung, beispielsweise Kratzer, einen Widerstandsverlust um 74 %, sobald sie eingetaucht werden. Die Ergebnisse dieser Arbeit beweisen die Umsetzbarkeit einer hermetischen Implantat-Verkapselung mit feuchtigkeitsdetektierender Funktion für den Zweck einer Verkapselungsüberwachung.

CONTENTS

Acronyms and Symbols

Acronyms

AH	absolute humidity
ALD	atomic layer deposition
ASIC	application specific integrated circuit
CMOS	complementary metal oxide semiconductor
CVD	chemical vapour deposition
DI	deionised
dpi	dots per inch
GPC	growth per cycle
HFE	hydrofluoroether
HMS	humidity monitoring system
IC	integrated circuit
IDE	interdigitated electrodes
ILC	inter-layer connection
IPA	isopropanol
IUPAC	international union of pure and applied chemistry
MEA	multi-electrode array
MEMS	micro-electro-mechanical system
PBS	phosphate-buffered saline
PCB	printed circuit board
PECVD	plasma enhanced chemical vapour deposition
ppm	parts per million
RH	relative humidity
SEM	scanning electron microscopy
TCO	transparent conductive oxides

TOF-SIMS	time of flight - secondary ion mass spectrometry
USG	undoped silicon glass
YAG	yttrium aluminium garnet

Symbols

A	area
h	height
l	length
M	molecular weight of water
n	number of atomic layer deposition (ALD) deposition cycles
n_c	number of ALD deposition cycles for start of island coalescence
P	water-vapour pressure
P_S	water vapour pressure at saturation
R	ideal gas constant
r	island radius
r_0	initial island radius
Δr	increase in island radius
r_K	Kelvin radius
SC	super-cycle
T	temperature
γ	surface tension of water
ρ	density of water
ρ_x	specific resistivity of metal x
w	width

1 Introduction - State of the Art and Aim of This Work

Active implants like approved systems for monitoring or stimulation purposes are becoming more and more popular as they allow direct and long-term treatment of corresponding diseases [1]. In addition to the electronic components of active implants, encapsulation materials and techniques also play a major role, since hermetic and biocompatible sealing are required.

Usually, application specific integrated circuit (ASIC)s or sensor chips are fabricated by microelectronics and feature common materials such as SiO_2 or Si_3N_4 on the chip surface for passivation purposes. Especially Si_3N_4 is a state-of-the art sealing material in micro-electro-mechanical system (MEMS) technologies due to good diffusion barrier properties for gases such as H_2, N_2 or He [2, 3, 4, 5]. Nevertheless, the biostability of SiO_2 and Si_3N_4 is poor [6], so that both passivation materials tend to dissolve if contact with ionic body fluids exists. As a result, acidic and corrosive substances can be formed [7, 8] which firstly can attack the surrounding tissue and secondly destroy the implants functionality.

In order to protect both the surrounding tissue and the implant from these effects, biocompatible and biostable sealing of the active components is mandatory, which is the reason why hermetic sealing materials and advanced encapsulation concepts are under continuous development. According to [9, 10], sealing materials like glasses, ceramics and metals show better hermeticity than silicones or epoxies (see Figure 1.1).

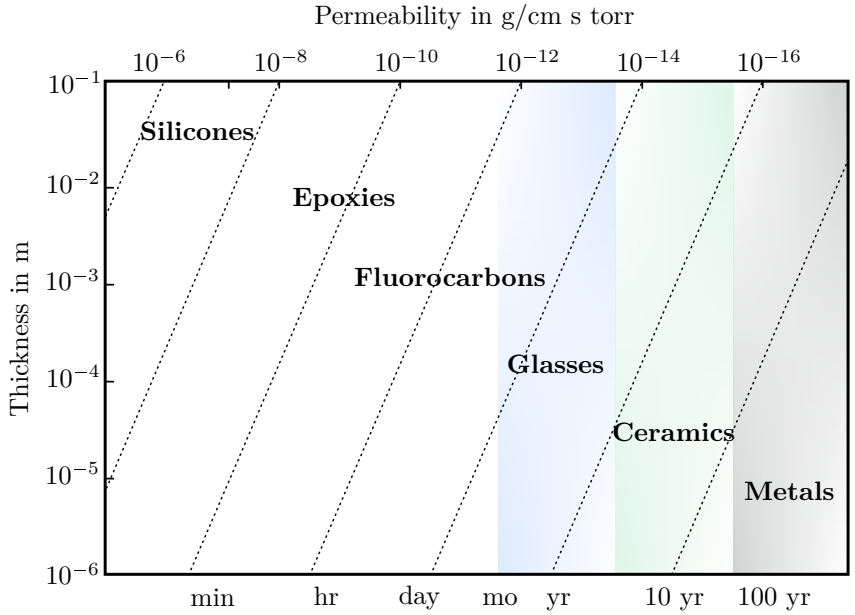

Figure 1.1: Simplified overview of the moisture permeability properties of various packaging materials, after [10].

Contemporary hermetic encapsulations on system level are exemplarily presented in Figure 1.2. Figure 1.2 a. demonstrates a lead-less, permanently implantable intramuscular stimulator. The device is mainly encapsulated with a thin-walled glass housing which contains feedthroughs to the electrodes. According to [10], ceramics feature better humidity barrier properties which enables the use as implant encapsulation material. In Figure 1.2 b. a cochlear implant is shown in which the circuitry of the implant is protected by a ceramic housing. Particularly metals, for example titanium, offer excellent sealing properties and fulfil long-term biocompatibility and biostability requirements, which is why they are used most frequently as implant housings for e.g. implantable defibrillators or pacemakers. The world's smallest pacemaker, according to the manufacturers [11], with a miniaturised metal housing is presented in Figure 1.2 c..
However, these popular hermetic encapsulation concepts also feature some disadvantages due to limited potential for smaller designs and the stiffness of the materials. Moreover, considering steadily diminishing sizes of integrated circuit (IC)s, electronic components and circuit boards, encapsulation techniques become the limiting parameter for further miniaturisation of implantable devices.

a.

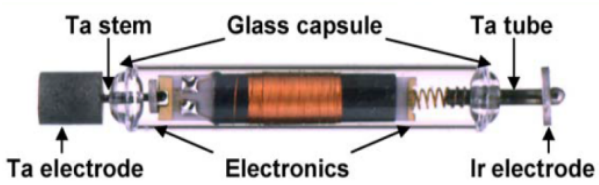

b.

c.

Figure 1.2: a. Intramuscular implant by BION with glass capsule [12], b. Pulsar cochlear implant by MEDEL providing ceramic housing [13] and c. Micra pacemaker by MEDTRONIC with miniaturised metal housing [11].

Depending on where the implant is applied, bulky and stiff encapsulations cannot be used, for example within the eyeball. In Figure 1.3 a., a retina implant with a coil for energy and data transmission (on the right side) and a multi-electrode array (MEA) for electrical nerve stimulation (on the left side) is presented. The polyimide foil with printed metallisation is mainly encapsulated with a very thin and flexible polymer. A similar example is presented in Figure 1.3 b., in which an intraocular pressure transducer implant can be seen. A polymer is also chosen as coating material for this device in order to keep the encapsulation flexible and miniaturised. The flexibility even supports accurate pressure measurements since the polymer may serve as a transmitting medium on top of sensitive pressure sensor membranes.

For these uses, biocompatible polymers are the material of choice as they enable flexible encapsulation without using rigid housings on system level. Thus, a miniaturisation of encapsulation volume can be ensured whereby whole implant size can decrease. In addition to implants with applications in the eye, implants surrounded by very sensitive tissue, such as in fine vessels, also require

miniaturised and flexible encapsulations. Miniaturisation is required for easy adaptation of the implant in the surrounding tissue. Flexibility allows the implant to be folded or curled up, so that smaller surgical incisions are needed and implantation procedures are less invasive.

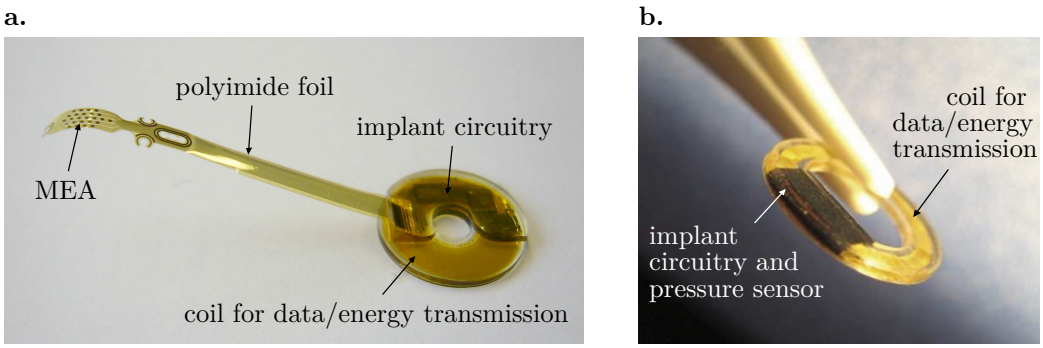

Figure 1.3: a. Retina implant with flexible polymer encapsulation, after [14], b. intraocular pressure transducer encapsulated in silicone rubber, after [15].

Due to the higher moisture permeability properties of polymers, such a polymer encapsulation cannot be sufficiently hermetic for long-term applications, compared to glasses, ceramics, or metals [16]. Therefore, several concepts have been developed in order to improve polymer-based encapsulation techniques in terms of long-term hermeticity in recent years. The most common approach is the reduction of moisture ingress by modifying polymers used and improving their water vapour barrier properties, for example by implementation of multi-layer stacks. Simple layer stacks utilise one thin ceramic layer, for example tantalum pentoxide (Ta_2O_5) by Atomic Layer Deposition (ALD). This ceramic layer is deposited between the electrical components and the encapsulating silicone and serves as additional hermetic sealing to the non-hermetic encapsulation on system level [6, 17, 18].

More complex stacks utilise the integration of several alternately applied polymer and hermetic layers, such as parylene C [19, 20], and metals, e.g. titanium [21], or ceramics, e.g. aluminum oxide (Al_2O_3) [22]. This implementation allows a significant reduction of water vapour absorption. These additional sealing layers (metals or ceramics) are applied very thinly (approximately between 100 nm [6] and 800 nm [23]) in order to fulfil the miniaturisation requirements. Small dimensions of sealing layers may yet result in critical disadvantages if local defects

occur, for example by flawed coating processes or mechanical impacts. These defects would act like weak points and corrode even faster [24]. Nevertheless, long-term performances of modified polymers or complex multi-layer stacks are still unclear, which limits the use of polymer encapsulated implants.
Instead of precise predictions of the time of degradation, the aim could be timely detection of humidity within the encapsulation so that the exact time of degradation could be determined. For this purpose, monitoring of water vapour diffusion into the encapsulated system is used. This information can be utilised to remove the implant only if the encapsulation is not working sufficiently and, thus, to maximise implantation time of silicone encapsulated devices. The general approach of humidity-monitoring encapsulation concepts with system level or component level encapsulations has been adopted by some research groups in the last two decades. Their work is presented in Chapter 1.1.

1.1 State-of-the-Art Approaches for Humidity-Monitoring Encapsulation

State-of-the-art approaches for humidity-monitoring encapsulations can be divided into two types which are distinguished by the encapsulation levels: system level and component level.
The first type, which is presented in Figure 1.4 a., consists of a hermetic package on system level and an optional silicone coating for an appropriate streamlined shape. A standard relative humidity (RH) sensor continuously measures the humidity level within the hermetic capsule and, thus, monitors the sealing quality of the hermetic package (metal, ceramic or glass capsule).
The second type, which is presented in Figure 1.4 b., consists of a non-hermetic silicone encapsulation on component level. Here, the encapsulation polymer also serves as sensitive material on top of interdigitated electrodes (IDE) which are often processed directly on top of the implant circuit board. Resistive or capacitive sensor signals reveal the grade of degradation in the silicone due to absorbed water. An additional hermetic metal or ceramic layer and a second silicone layer may be used optionally for improved humidity barrier properties and appropriate shape of the implant encapsulation. For both types of encapsulation monitoring concepts, examples are presented below.

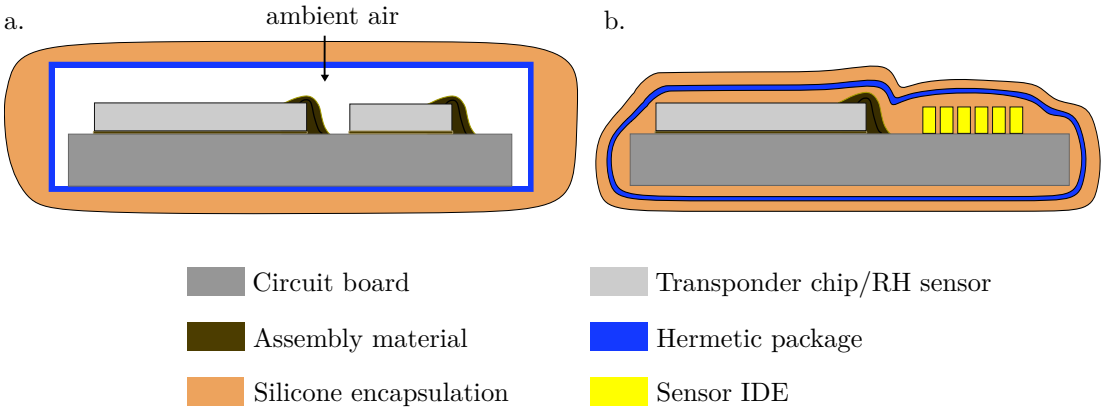

Figure 1.4: Encapsulation types for active implants with humidity-monitoring function: a. hermetic package on system level with optional silicone coating for appropriate, streamlined shape, RH sensor reacts to changes in relative humidity within hermetic package; b. silicone encapsulation on component level, RH sensor reacts to absorbed water in the silicone, optionally with additional stack of hermetic layer for advanced humidity barrier properties and second silicone layer for a streamlined shape; adapted from [16, 21].

First, developments regarding hermetic system level encapsulations with a humidity-monitoring function are discussed.
In 2001, M. Dokmeci and K. Najafi presented a high-sensitivity polyimide capacitive RH sensor which should be used to monitor anodically bonded micropackages. The sensor had a surface area of 1 mm^2 and consisted of two stacked aluminum electrodes with a spin-coated CU1512 polyimide of 300 Å to 1200 Å thickness in between. A simplified cross-section of the RH sensor is presented in Figure 1.5 a., whereas an optical photograph is shown in Figure 1.5 b.. Characterisation was performed at 37 °C within a climate chamber at humidities from approximately 30 % to 70 % with increments of 10 %. Sensors with 300 Å polyimide film revealed a sensitivity of 3.4 pF per %RH, sensors with 1200 Å showed a sensitivity of 0.86 pF per %RH. Figure 1.5 c. shows a 300 Å-thick sensor which is wire-bonded on a silicon substrate on top of a printed circuit board (PCB). This testing set-up presents the actual packaging substrate. Comparable sensitivities were achieved by exposing this device (without any encapsulation) to ambient humidity of 30 %RH to 60 %RH. [25]
As a follow-up work, T.J. Harpster and S. Hauvespre joined their colleagues' work in 2002 and published a humidity monitoring system (HMS) consisting of a silicon substrate, an IC, the previously presented polyimide capacitive humidity sensor and a receiving coil.

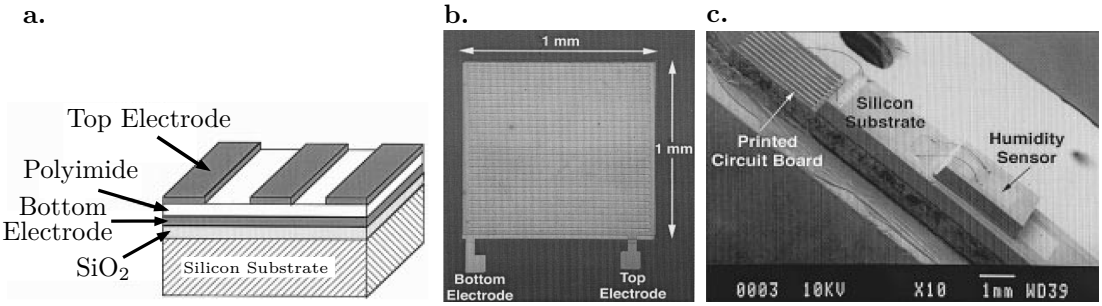

Figure 1.5: High-sensitivity polyimide capacitive humidity sensor for monitoring anodically bonded hermetic micropackages: a. simplified drawing of the sensor cross-section; b. photograph of the 1 mm^2 RH-sensor; c. scanning electron microscopy (SEM) image of the RH-sensor assembled on a silicon substrate for testing purposes; after [25].

An anodically bonded glass capsule shielded the inner volume from humidity and served as a hermetic and biocompatible long-term encapsulation. The humidity level inside the glass capsule was monitored by the capacitive humidity sensor which, together with the receiving coil, formed an oscillating circuit. The resonant frequency of this LC circuit changed with response to changes in humidity. Thus, the 7 x 1.2 x 1.5 mm^3 implantable device allowed continuous (wireless) remote monitoring of humidity changes inside the micropackage with sufficient resolution. Figure 1.6 a. shows a conceptual drawing of the passive system, whereas Figure 1.6 b. shows a photograph of the HMS, enclosed with the glass-silicon package, and an external ferrite core readout antenna. A 60 % change in RH resulted in a resonant frequency shift of about 0.2 MHz. [26]
Long-term test results were obtained with the presented hermetically-sealed glass-silicon micropackages. Room temperature soak tests in phosphate-buffered saline, accelerated soak tests in heated saline and even in-situ hermeticity and biocompatibility tests with packages implanted in guinea pigs for up to 22 months were accomplished. Each tested package remained hermetically sealed, which was wirelessly monitored biweekly by the polyimide capacitive humidity sensor. [27]

The integration of a capacitive humidity sensor inside the micropackage (presented in [25, 26, 27]) allows the monitoring of the sealing qualities of the anodic bonded glass capsule on a silicon substrate. The fabrication of these sensors is separated from the assembly process of the housing. Even though the results are positive and promising, the aspect of further miniaturisation of the implant housings is not considered in this approach.

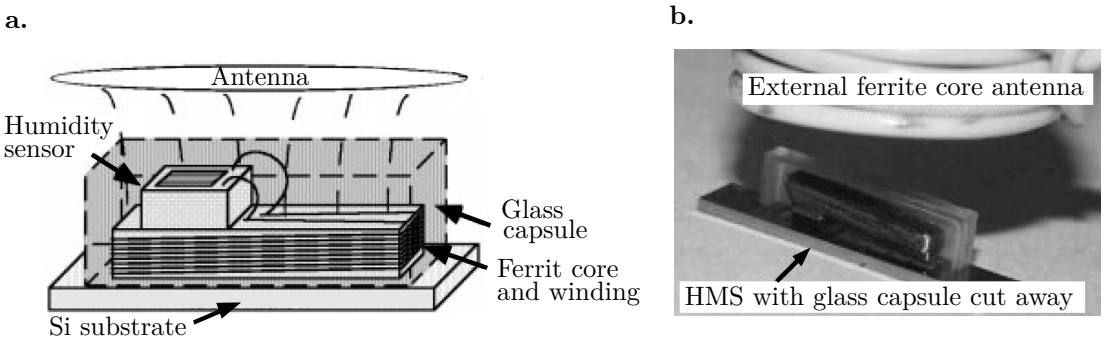

Figure 1.6: Passive humidity-monitoring system for in-situ remote wireless testing of micropackages: a. conceptual drawing of the passive system; b. photograph of the HMS with glass-silicon package (external ferrite core antenna serves as readout device); after [26].

Since miniaturised and flexible encapsulations can be achieved by coatings with biocompatible polymers, there have also been approaches for component level encapsulation with humidity-monitoring function in recent years. Some of these approaches, which utilise the encapsulating silicone as the sensitive sensor layer, are discussed.

In 2007, R.P. von Metzen and T. Stieglitz presented a wireless system for monitoring polymer encapsulations which detected changes in the electrical properties of insulating polymers for electrically active implants. IDE were coated with this polymer and formed an oscillating circuit whose resonant frequency was detuned when exposed to defined levels of humidity. Measurable detuning of this oscillating circuit could be interpreted as a capacitive or resistive sensor signal. Depending on the amount of adsorbed water vapour, detailed information about the metal/polymer interface could be obtained. This enabled the monitoring of the encapsulation and revealed information about its stability, degradation, delamination or even about the corrosion of the metallisation underneath the polymer encapsulation. According to the authors, this method can be used for in-situ monitoring of the stability of implant encapsulations to predict failures, even before they occur. [28]
The drawback of this work is the limited area in which humidity could be detected. Only if the ingress of water occurs in closest proximity to the IDE, a change of the sensor signal could be observed.

A similar approach was presented by M. Weinmann and colleagues in 2012 and 2013. By combining carefully-selected biocompatible polymers and inorganic bar-

rier layers, the group implemented a flexible and hermetic encapsulation concept for electrically active implants. Therefore, a hybrid stack of parylene C, an approximately 800 nm thick sputtered Au- or Ti-humidity-barrier layer and again parylene C, as additional sealing layer, was used. Furthermore, a flexible thin-film humidity sensor was presented in order to monitor the impermeability of the implemented encapsulation stack. This humidity sensor consisted of a thin, sputtered Ti/Au bottom electrode, a sensitive polyimide layer, which is deposited by spin-coating, and a perforated top electrode, also thinly sputtered. Structuring of metal electrodes was achieved by means of photo-lithographic patterning and etching steps. A top-view SEM-image of the perforated top electrode is presented in Figure 1.7 a., whereas Figure 1.7 b. shows a schematic oblique view of the presented thin-film humidity sensor.

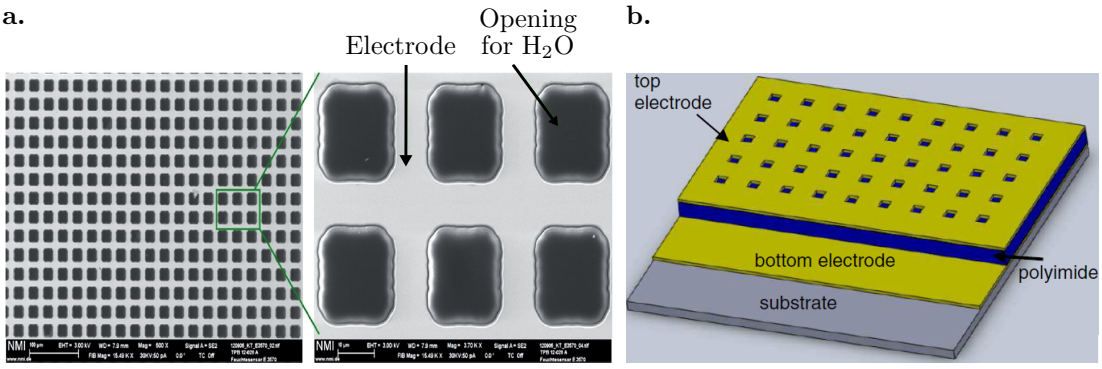

Figure 1.7: Thin-film humidity sensor for the integration into polymer-based long-term stable hermetic active implant encapsulation layers: a. SEM-image of perforated top electrode; b. schematic of presented thin-film humidity sensor; after [23].

Before being coated with parylene C and a humidity-barrier layer, the sensor was tested regarding sensitivity and response time. A linear sensor response with a sensitivity of up to 0.84 pF per %RH could be achieved between approximately 10 %RH and 85 %RH. Even after a subsequent annealing step at 350 °C for an hour, which corresponded to the temperature stress of further processing with polymer and humidity-barrier-layers, the sensor showed comparably sensitive behaviour. Additionally, the dynamic behaviour of the sensor was tested successfully by the application of water to the sensor surface. As expected, the uncoated sensor reacted immediately. A saturation of the capacitive sensor signal was achieved after three minutes. In contrast, the sensor, which was coated with a biocompatible polyimide only, achieved sensor signal saturation after five

hours, whereas the sensor with polyimide and titanium coating did not show any reaction within the investigation time of seven hours. Thus, the applicability of presented encapsulation stack and functionality of the developed capacitive humidity sensor was proven. As an outlook, the authors claim to integrate this humidity sensor into the flexible polymer encapsulations of real active implants. [21, 23]
Nevertheless, the presented encapsulation concept can only be implemented using processes of microsystem technology, for example spin-coating of polyimide or sputtering and patterning of Au-layers, which are not transferable to three-dimensional substrates with complex topographies.

Both types of humidity-monitoring implant encapsulations feature advantages and disadvantages. Hermetic packages on system level, which are also called type 1 in the following, feature following properties:

Advantages of hermetic packages on system level (type 1):

- Excellent hermeticity
- Long-term stability
- Bicompatibility and biostability
- No further silicones for implant coating are needed.
- Fabrication of humidity sensing element is independent from implant assembly or encapsulation.

Disadvantages of hermetic packages on system level (type 1):

- Miniaturisation of encapsulation volume is limited by size of hermetic package.
- Rigid materials are not very appropriate for the use within the body.
- In case of degradation of the hermetic sealing: damage to electrical components of the implant occurs immediately.

Compared to type 1 encapsulations, silicone encapsulations on component level show some improvements regarding encapsulation volume. These encapsulations, also called type 2 in the following, also feature drawbacks in other aspects.

Advantages of silicone encapsulations on component level (type 2):

- Biocompatibility and biostability
- Minimised encapsulation volume
- Integration of hermetic layers (metal/ceramic films) is possible.
- Good humidity barrier properties if hybrid layers (polymers with integrated hermetic sealing) are used
- In case of degradation of the hermetic sealing: damage to electrical components of the implant occurs slowly (depending on the water diffusion velocity through the silicone).

Disadvantages of silicone encapsulations on component level (type 2):

- Poor hermeticity on component level due to insufficient humidity barrier properties of silicones
- The fabrication of the humidity sensing element is integrated into implant assembly and encapsulation.
- Presented technologies of state-of-the-art approaches are not transferable to three-dimensional substrates with complex topographies.
- Detection of humidity is only possible in close proximity to IDE.
- Silicone encapsulation of implant circuit boards with electrically active components (for example sensor chips or readout ASICs) is not established yet (except in research [29, 30, 31]).

By combining the advantages and avoiding the disadvantages of both encapsulation types, an advanced and improved encapsulation concept can be developed.

1.2 Aim of this Work

The aim of this work is to develop an advanced encapsulation concept for active implants which features a humidity-monitoring sensor layer within the encapsulation stack. In order to obtain a miniaturised encapsulation volume, component level encapsulation is chosen. Individual layers of the three-dimensional encapsulation stack serve different purposes such as hermetic sealing, immediate detection of moisture within the encapsulation through an all-round enclosing humidity sensor layer, and isolation of electrical components. The concept should allow further coatings with shaping silicone by injection moulding processes easily.
A hermetic layer, which is the top layer of the stack, protects the implant from body fluids, even if a silicone coating above is saturated with humidity over time. In case of a mechanical defect in the hermetic sealing, body fluids will diffuse into the encapsulation stack. As soon as the sensitive material of the humidity detection layer is reached, a significant change in resistivity occurs which leads to a change in sensor signal. Thus, exceeding of a specific threshold value can be interpreted as a degradation of the encapsulation stack. Even in case of water ingress, electrical components of the implant are protected by the isolating polymer underneath the humidity detecting layer. This polymer features sufficient barrier properties so that further water ingress can be stopped for a specific period of time. Thus, electrical components of the implant are protected from humidity until the implant can be removed before risks for the patient arise.

Implementation of such a concept poses various challenges in the technological field. Since all layers of the encapsulation stack should be applicable three-dimensionally, only isotropic deposition methods with very high step coverage can be used. Only in this way, an all-round humidity detecting function can be guaranteed. The humidity sensitive layer should enable localisation of defects within the hermetic sealing anywhere in the implant encapsulation and not only in closest proximity to IDE on a specific spot of the circuit board. Additionally, in order to support highest possible miniaturisation, encapsulation stack layers should be deposited thinly and conformally.
Further challenges arise due to temperature limitations, which are not only set by CMOS components of the implant. In addition, operation temperatures of

assembly materials which are needed for implant assembly, limit processes that could be considered for this encapsulation concept.

This novel encapsulation concept combines all the advantages of the presented types of self-monitoring encapsulations. Required biocompatibility and biostability can be guaranteed by the choice of used encapsulation materials. Drawbacks in state-of-the-art approaches, such as small local resolution of the humidity sensing element or quickly occurring damages on electronic components in case of water ingress, can be overcome by the three-dimensional component level encapsulation concept consisting of the above-mentioned functional layers.
The objective of this work will be the implementation of individual layers of the encapsulation stack regarding suitable materials and process limitations. Especially the development and characterisation of a thin-film humidity sensitive layer which should enclose the total implant surface and show significant change in resistivity when adsorbing water, is the main focus.

2 Theory of Measuring Humidity and Microsystem Techniques used

2.1 Theory of Measuring Humidity

Sensors for humidity measuring are widely used since monitoring of environmental humidity plays a significant role in various application fields, mainly for industrial processes [32]. In particular, the use of humidity control systems has increased for quality control purposes in the production processes of electronic devices, precision instruments, textiles and foodstuff [33].

With increasing diversity of application fields, the diversity of requirements increases as well for example stability against high temperatures or harsh environments, or with regard to sensor properties, such as accuracy or sensitivity. Considering these requirements, it is important to choose a sensor with suitable sensor material and properties in order to monitor the needed measurand.
The definition of humidity is categorised into absolute humidity (AH) and RH, whereby

- AH reveals the amount of water vapour in the air without considering the temperature (expressed as grams per cubic meter of air g/m^3) and
- RH reveals the amount of water vapour relative to the current temperature and pressure of the air (expressed as a percentage % of the total amount which could be held).

Thus, humidity sensors are also categorised into AH sensors, also called hygrometers, and RH sensors. Measuring the total amount of water vapour in air is implemented by a dew/frost point detection which determines the temperature (above 0 °C) at which water vapour condenses to liquid water (dew point) or (below 0 °C) at which water vapour condenses to ice (frost point). Dew/frost point

hygrometers often utilise a chilled mirror, a light source and photo-detector with which the moment of dew can be determined optically. Dew/frost point detection depends on the current pressure, but is independent of temperature. Another unit for absolute humidity measurement is parts per million (ppm) which represents water vapour content by volume fraction and has extensive applications in industry [34]. Relative humidity, however, is the most monitored type of humidity. The amount of adsorbed water vapour, which is equivalent to relative humidity, changes electrical or mechanical properties of the sensitive material through which the water vapour amount in the surrounding air can be monitored. RH-sensors are classified according to the sensitive material which is utilised.
In the presented encapsulation concept of this work, the hermeticity of a material stack shall be monitored by a sensitive thin-film layer which also changes electrical properties after adsorbing water molecules. Therefore, materials and measuring mechanisms of RH-sensors are discussed in more detail in the following chapters for the development of such a thin-film material.

2.1.1 Classes of Humidity Sensing Materials

General requirements for humidity sensing materials are high sensitivity, short response times, reproducibility, durability and minimal dependency on temperature. Further demands, such as chemical or physical stability, may be required regarding specific conditions of sensor application. Thus, the choice of sensitive materials enables a pre-selection of required properties. Three classes of humidity sensor materials which serve for various methods of transduction types and sensing mechanisms are:

- inorganic ceramics,
- organic polymer-based materials and
- inorganic-organic hybrid materials.

Sensors with these materials are also distinguished by properties like fabrication technology, costs, and specifications. Table 2.1 provides a simplified overview with processing techniques and transductions types.

Specific advantages and disadvantages of materials have to be taken into account for the selection of a suitable sensor material. Not only sensing qualities

Table 2.1: Technologies and Specifications of different relative humidity measuring sensor materials, after [35].

Technology	**Specification**						
	Sensing material			**Transduction type**		**Sensing mechanism**	
	Polymer	Hybrid	Ceramic	Resistive	Capactive	Electronic	Protonic
Conventional ceramic/ semiconductor processing	Not available	Available	Available	Available	Available	Ceramic	Ceramic and Hybrid
Thick/ thin film	Available	Available	Available	Available	Available	Ceramic	Polymer, Hybrid, Ceramic

but also circumstances of manufacturing steps are relevant. For example, workability or stability at temperatures up to 300 °C, which represents the highest applied temperature of the following processes, have to be considered. The most important properties of polymers, metal oxides and semiconductors are listed in Table 2.2.
Even though polymers provide good sensitivity and selectivity, fabrication technology is generally not suitable with conventional semiconductor processing. Hence, manufacturability is lowered and costs are comparatively increased. Additionally, polymers cannot withstand elevated temperatures for long periods [36]. This property is unproblematic for the later application but very critical for the manufacturing process of the encapsulation concept presented in this work. Therefore, ceramics are considered as humidity-sensitive materials. This selection not only demonstrates sufficient sensitivity and stability, but also enables conventional semiconductor processing methods at temperatures of at least up to 400 °C.

Nevertheless, a suitable ceramic as humidity-sensitive material has to be developed in this work in order to fulfil specific requirements regarding not only regarding process limitations for a three-dimensional encapsulation concept, but also for appropriate sensitivity. As a main focus of this thesis, the development of such a humidity-sensitive ceramic is presented and discussed in Chapter 3.2.3 and Chapter 3.3.4 and verified in Chapter 4.1.
Previously, sensing mechanisms of common ceramic humidity sensors are discussed. For impedance-sensitive type humidity sensors, the decrease of electrical

Table 2.2: General advantages and disadvantages of various materials for gas sensor applications, after [37, 35].

Properties	Materials		
	Polymers	Metal oxide ceramics	Semiconducting ceramics
Stability	Very poor	Very good	Poor
Sensitivity	Good	Good	Average
Selectivity	Very good	Poor	Poor
Operating temperature	up to 200 °C	up to 800 °C	up to 400 °C
Manufacturability	Average	Very good	Average
Costs	Medium	Low	Low
Suitability for this work	-	+	+

impedance or the increase of conductance of the sensing material is crucial. For capacity-sensitive type humidity sensors, the increase of the dielectric constant is considered. These changes in electrical properties are proportional to the amount of adsorbed water molecules with which the sensor layer interacts. Resistive humidity sensing mechanisms of metal oxide ceramics and semiconducting ceramics are explained in the following Chapter 2.1.2.

2.1.2 Humidity Sensing Principles

Ceramic type sensors can be designed by using dielectric metal oxides or semiconductors. Metal oxides serve as ionic-type humidity sensors, while semiconducting ceramics serve for electronic-type humidity sensors. The humidity sensing principles of both sensor material types differ and need to be discussed first.

Sensing Mechanism of Metal Oxide Ceramics

There are two types of impedance-sensitive sensor materials which are classified by the mechanism of the electrical transport of charge carriers, ones with protonic conduction and ones with electronic conduction. Regardless of the sensing or conduction type of the sensor material (protonic or electric impedance-sensitive or capacitive), the sensing mechanism of ceramic humidity sensors is based on water vapour adsorption. For enhanced adsorption, granular or porous materials are preferred. Inter-grain gaps and pores increase the capacity for the adsorption of water molecules, which is schematically presented in Figure 2.1.

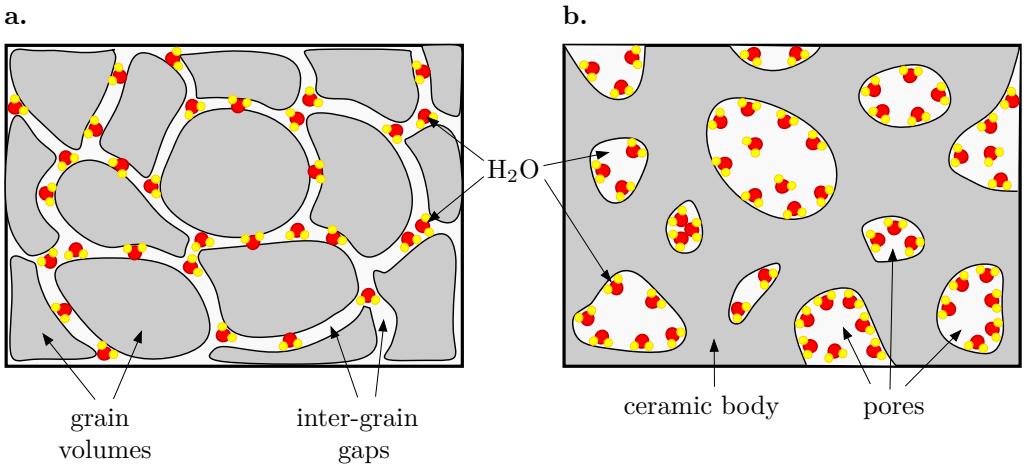

Figure 2.1: Simplified illustration of water vapour adsorption: a. shows the adsorption of water molecules within the inter-grain gaps of granular ceramics (water molecules permeate into the ceramic along the grain boundaries); b. shows the adsorption of water molecules within capillary pores of porous ceramics (water molecules permeate into the ceramic through the pores), after [35].

The water vapour adsorption occurs in two subsequent steps which arise when a granular or porous ceramic film is exposed to humid atmosphere [38]:

1. Chemical adsorption (chemisorption) on the surface of crystalline grains,
2. Physical adsorption (physisorption) on the generated hydroxyl groups after chemisorption.

Chemisorption

The surface layer of a metal oxide's grains is covered by ions which feature high local charge density and a strong electrostatic field. When the metal oxide is exposed to humid atmosphere (even at low humidity), these ions serve as active sites for water molecules which quickly occupy available sites (chemisorption) and form hydroxyl (OH^-) groups on the grain boundary surfaces [39, 40]. This chemisorbed layer is not further affected by exposure to humidity and remains unchanged. It is presented in Figure 2.2 a. using the example of a semiconducting ZnO surface.

Physisorption

After the completion of the chemisorbed layer, subsequent water vapour molecules can be physically adsorbed on the previously formed hydroxyl layer by the van der

Waals force (physisorption) and form new hydroxyl groups (Figure 2.2 b.). Continuous exposure to water vapour allows the adsorption of further water molecules via double hydrogen bondings to two neighbouring hydroxyl groups so that further physisorbed layers occur and the monolayer physisorption changes to a multilayer (Figure 2.2 c.). Water molecules in the following layers may be singly (not doubly) bonded to local hydrogens, which is why second and further physisorbed layers are less ordered than the first one. The formation of physisorbed multilayers of water molecules leads to an increase of the dielectric permittivity [41].
With an increasing number of physisorbed layers of water molecules, molecules in upcoming layers show single hydrogen-bonds and form aquatic layers by capillary condensation at the grain boundaries and pores of the ceramic.

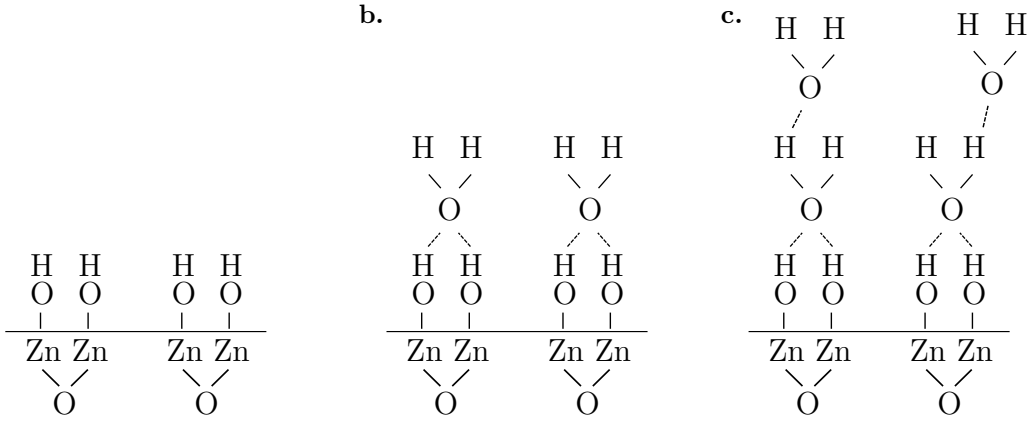

Figure 2.2: Adsorption of water vapour molecules on the surface layer of ZnO: a. Chemisorption of water molecules at metal oxide's ions at the surface layer and formation of hydroxyl groups, b. physisorption of subsequent water molecules on the present hydroxyl groups and forming first physisorbed monolayer, c. formation of physisorbed multilayers, water molecules in the following layers are only single-bonded, after [34, 35].

Capillary condensed water film

For ionic sensing materials (which are generally porous metal oxides), protons can tunnel from one water molecule to the neighbouring water molecule through hydrogen bondings. The mechanism of proton tunneling is called the Grotthuss mechanism [42]. This proton transfer, or proton conduction, appears between the H-bonded networks between water molecules [43] and is presented in Figure 2.3.

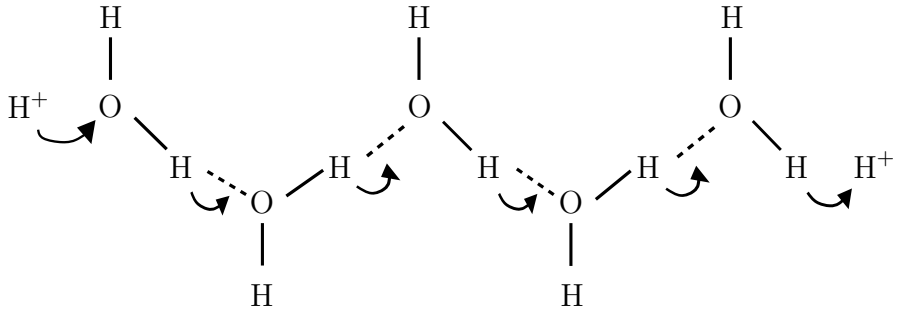

Figure 2.3: Grotthuss mechanism: proton tunneling from one water molecule to the next via hydrogen bonding, after [34].

Thus, protons are the dominant carriers responsible for electrical conductivity if a thin water film is developed on the surface at high humidity levels. If the surface of a sensing material is not completely covered (at lower humidity levels), proton transfer only occurs between neighbouring water molecules within a cluster. Here, the dominant conductivity is due to diffusion of hydronium ions (H_3O^+) on hydroxyl groups. A water molecule renders a hydrogen ion (H^+) to become a hydroxide ion (OH^-):

$$H_2O \longleftrightarrow H^+ + OH^-. \tag{2.1}$$

The released hydrogen binds to another water molecule immediately and forms a hydronium ion. This water vapour interaction can thus be described as:

$$H_2O + H_2O \longleftrightarrow H_3O^+ + OH^-. \tag{2.2}$$

Charge transfer is guaranteed by H_3O^+ releasing a proton to an adjacent water molecule which forms a new hydronium ion:

$$H_3O^+ \longleftrightarrow H_2O + H^+. \tag{2.3}$$

This mechanism is called proton hopping and continues from one water molecule to another. The proton hopping influences the electrical properties of the porous metal oxide ceramic by increasing its conductivity. Thus, current flow on the surface of the sensing material is facilitated.

Sensing Mechanism of Semiconducting Ceramics

Wide-bandgap semiconducting ceramics in granular form, such as ZnO, SnO_2 and In_2O_3, are widely used as humidity sensing materials. Basically, a change in conductivity of the semiconducting grains is caused by trapping electrons from adsorbed water molecules which results in a band bending [44]. Increasing water vapour amount leads to conductivity increase for n-type and decrease for p-type semiconductors [45, 46]. For n-type semiconductors, water molecules act like electron donors when they are chemisorbed at the surface [38, 47, 48].
In ambient air with a low humidity level, oxygen molecules are chemisorbed at the grain surfaces and receive free electrons from the negatively-doped semiconductor.

$$O_2 + e^- \longrightarrow {O_2}^-. \tag{2.4}$$

This leads to a depletion region (also called space charge region) at the grain boundaries, as presented in Figure 2.4 a.. The capturing of electrons leads to band bending over the depletion region which is smaller than the grain size. With an increasing level of humidity, water molecules replace oxygen molecules by forming hydrogen peroxide (H_2O_2) and releasing electrons which are donated to the depleted region. Electron release is explained by the following equation.

$$2\,H_2O + {O_2}^- \longrightarrow 2\,H_2O_2 + e^- \tag{2.5}$$

Thus, the amount of free electrons in the semiconductor grain increases whereby the depletion region shrinks and band bending is less pronounced (see b. in Figure 2.4). Consequently, a change in conductivity of the single grains occurs so that current flow through the grain volumes is facilitated. Even an enriched surface with accumulated electrons is formed if the potential barrier height at the grain boundaries is reduced to zero. Thus, a change in conductivity of the whole granular ceramic is achieved.

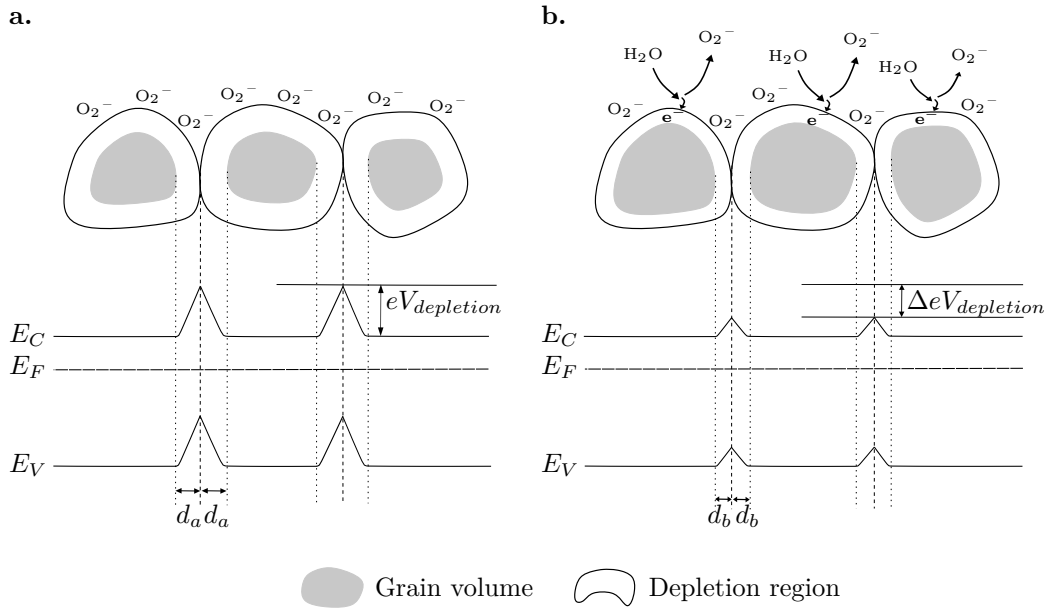

Figure 2.4: Simplified model of an n-type semiconductor with potential barriers at the grain boundaries and respective band diagram, adapted from [47, 44]: a. Adsorbed oxygen molecules at the grain surfaces trap free electrons which causes a depletion region and equivalent band bending, potential barrier height and length being $eV_{depletion}$ and d_a, respectively. b. Water molecules replace adsorbed oxygen molecules by releasing free electrons to the depletion region which shrinks to a length of d_b. Band bending is reduced by $\Delta eV_{depletion}$ which increases conductivity of each grain.

Additional to the increasing conductivity due to interaction between metal cations and chemisorbed hydroxide ions at lower degrees of relative humidity, pysisorption and capillary condensed water films also occur at higher degrees of relative humidity. This leads to:

- electric conduction with increasing conductivity due to electron donation of adsorbed water molecules at low levels of relative humidity and
- additional proton conduction due to proton tunneling between neighbouring water molecules (Grotthuss mechanism) at higher levels of relative humidity.

Thus, semiconductor humidity sensors may utilise both conduction methods. Nevertheless, geometric parameters of sensitive semiconductors (such as surface area or average particle size) have less influence on sensing characteristics in electronic-type humidity sensors than in the ionic-type humidity sensors [36].

Influence of Porosity

The interaction of ceramics with water molecules depends strongly on the surface structure and thus on the amount of active sites on the surfaces of single grains. These active sites allow the adsorption of water molecules and thus influence sensor sensitivity. For polycrystalline semiconductors, junctions between the grains serve as permeation channels for water vapour [32, 34]. This effect can be enhanced through additional hetero junctions if a ceramic composition is used [49]. For the ionic type humidity-sensing principle with single-crystal ceramics (for example SiO_2) or amorphous ceramics (for example Al_2O_3), porosity of the ceramic is required for sufficient sensor performance. A sponge-like surface allows enhanced permeability and condensation of water vapour in capillary pores. Thus, adsorption of water vapour is promoted by increased granularity for polycrystalline semiconducting ceramics and porosity for single-crystal ceramics. The more complex structure of the ceramics elevates the number of active sites for water molecule adsorption on the surface of grains or pores, increasing sensor sensitivity.

Pores with diameters from 2 nm to 10 nm promote the sensing mechanism at low levels of humidity and pores with diameters from 20 nm to 100 nm promote the sensing mechanism at high levels of humidity [50]. Regarding the definition by the international union of pure and applied chemistry (IUPAC), in which *micropores* show diameters $\leqslant 2$ nm, *mesopores* show diameters between 2 nm and 50 nm, and *macropores* show diameters $\geqslant 50$ nm, at least mesopores and macropores are necessary for the detection of low and high levels of humidity [51].

The amount of capillary condensed water is dependent on three parameters: the volume of open pores, the pore radius and the distribution of open pores. The pore size, at which capillary condensation occurs at different temperatures (T), can be determined by means of the Kelvin equation 2.6:

$$r_K = \frac{2\gamma M}{\rho RT \cdot ln(P_S/P)} \ , \tag{2.6}$$

where r_K is the Kelvin radius, P is the water-vapour pressure and P_S is the water vapour pressure at saturation [33]. γ, ρ and M are surface tension, density and molecular weight of water, respectively. R is the ideal gas constant.

2.2 Microsystem Techniques used

In this chapter, microsystem techniques are described and explained which not only found application in this work but also played an important role due to their special features such as excellent deposition conformities and die-level processing. This includes chemical vapour deposition (CVD) processes (Gorham process and ALD) and patterning through laser-based micromachining.

2.2.1 Deposition Processes

Considering the substrate used in this work, which is a silicon substrate with metallisation, CMOS-chips, bonding wires and assembly materials, deposition methods at low temperatures (approximately up to 300 °C) and with high film conformity are required. Due to the complex topography of the substrate, sufficient step coverage with outstanding film quality is needed. A comparison of different deposition methods regarding typical materials, deposition temperatures, and film conformities is presented in Table 2.3.
By providing good and excellent film conformities, respectively, only CVD and ALD techniques are suitable for the coating of such a complex substrate which is why these processes are utilised in this work. Both techniques are highly isotropic and benefit from properties like uniformity and purity. Additionally, material selection and process temperatures are suitable for this work.

Chemical Vapour Deposition (CVD)

A CVD process is a common thin film deposition technique in which precursor gases are transferred to the substrate to be coated. Chemical reactions, which occur on the substrate surface, form a thin and solid film. These chemical reactions are initiated by process temperature, frequency of radiation or use of plasma. These attributes are used to differentiate CVD processes into thermal CVD, photo-assisted CVD, and plasma enhanced chemical vapour deposition (PECVD), respectively. Film growth rates for thermal CVD primarily depend on substrate temperature, but also on process pressure and composition of the precursor gas. [53]

Table 2.3: Comparison of different deposition methods regarding typical materials, deposition temperatures, and film conformity [52].

Layer Deposition Method	Typical Materials	Typical Deposition Temperature	Film Conformity	Suitability for this work
CVD	Si, SiO_2, Si_3N_4, etc.	up to 400 °C	Good	+
PECVD	SiO_2, Si_3N_4, etc.	150 °C	Poor	-
Sputtering	Mo, Al, Au, etc.	50 °C	Poor	-
Spinning	Photo resist	100 °C	Poor	-
ALD	Metal oxides, metal nitrides, noble metals, transparent conductive oxides (TCO), etc.	Typically 200 °C to 400 °C, but even down to room temperature and up to 800 °C, depending on the process reactants	Excellent	++

In this work, the Gorham process is used for the vapour-deposition of parylene which is schematically presented in Figure 2.5. The solid dimer material is placed into the vaporiser, where it evaporates to dimer gas at approximately 175 °C. Passing through a very high temperature pyrolysis at 680 °C, dimer gas molecules are split into monomer gas molecules.

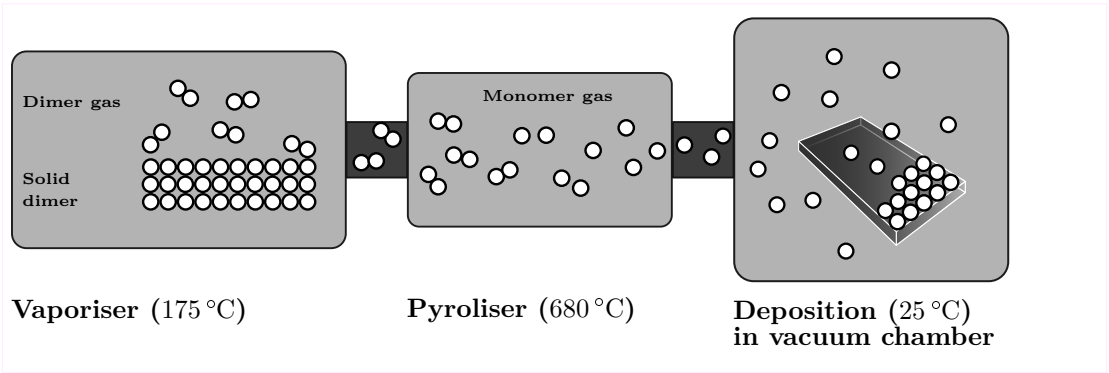

Figure 2.5: Gorham process - CVD of parylene at room temperature, after [54].

These monomers are lead into a vacuum deposition chamber in which the target substrate is placed. At room temperature (approximately 25 °C), polymerisation of the monomers begins on all exposed surfaces of the substrate so that a conformal and isotropic deposition can be achieved. Due to a cold trap (−70 °C) behind the vacuum deposition chamber residual monomers can be trapped which allows an extremely pure coating of the substrate. [55, 56]

Atomic Layer Deposition (ALD)

Unlike CVD, ALD technology utilises the alternating exposure of two precursors which leads to sequential and controlled reactions on the surface of the substrate. Thus, a self-limiting film growth of up to one atomic layer per deposition cycle can be achieved. This allows a highly conformal and dense thin film coating [57]. High isotropy of ALD layers allows conformal depositions even on non-planar substrate surfaces with high aspect ratios. Due to the possibility of coating three-dimensional structures, ALD has become very popular in MEMS technologies. [58]

Due to the variety of materials, ALD-films can be utilised as tailored functional films with specific properties. Starting with insulating metal oxides, which may serve as ultra-thin *high-k* dielectrics or metal gates [59], ALD also provides a number of conductive nitrides and noble metals which can be used as electrode layers. Further properties, such as optical (for example as ultra-thin TCO), chemical (e.g. for biocompatible coatings) and tribological characteristics (e.g. for low friction or anti-stiction coatings), enlarge the applications field for functional ALD-films. [52]

ALD Process

An ALD process, which is based on at least two reactants (also called precursors), can be described as a deposition cycle with at least 4 steps. In step 1, the first gaseous precursor is applied on a solid substrate with active sites, so that its surface is saturated with the reactant. In step 2, an inert purging gas is applied in order to remove excess precursor or any by-products. In step 3 the second gaseous precursor is applied which leads to chemical reactions between the molecules on the saturated surface of the substrate. After a second purging in step 4 only the required ALD material with a thickness of up to one atomic layer is left. The schematic illustration of such an ALD cycle is illustrated in Figure 2.6.

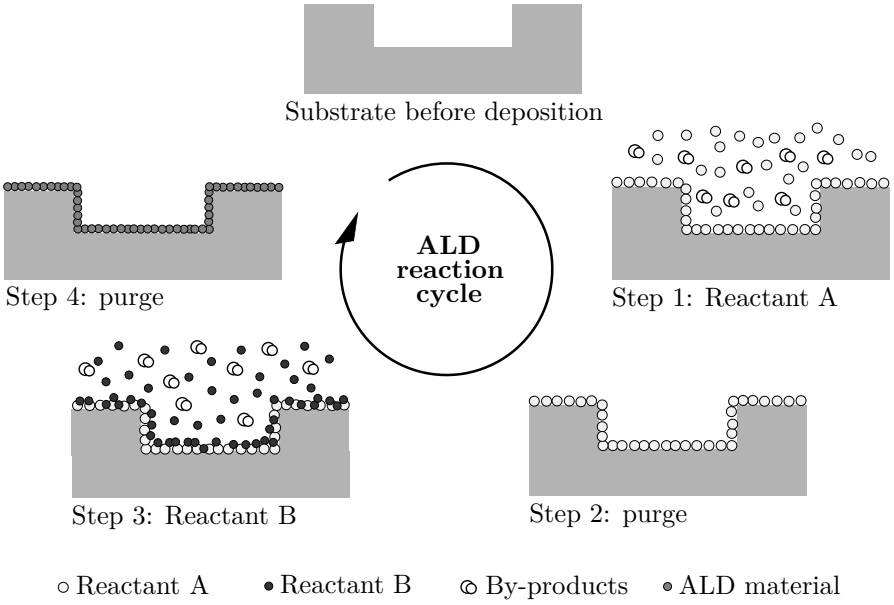

Figure 2.6: Schematic illustration of an ALD process, after [57].

The deposition velocity is measured in growth per cycle (GPC) which depends on pulsing times of single precursors. Only if these times are sufficiently long, a saturation of the substrate's surface to be coated can be guaranteed. Another important process parameter is the process temperature. It can influence the reactivity of used precursors and, thereby, increase or decrease the growth rate.

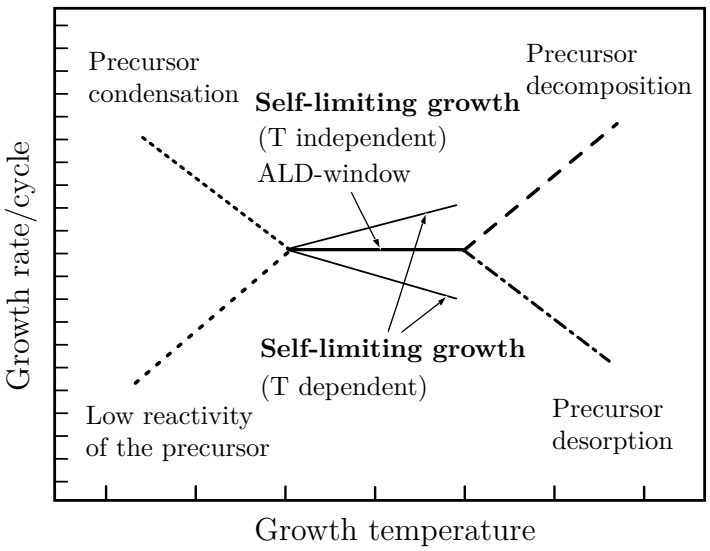

Figure 2.7: ALD window for constant and T independent self-limiting growth, after [58].

In order to improve the reproducibility of film growth, a temperature range (called ALD-window) should be considered in which a self-limiting growth with a constant growth rate is established for corresponding materials (see Figure 2.7). [58]

Phenomenon of island growth

There are four groups of classification for ALD processes on the basis of GPC variations (see Figure 2.8) with a dependency on the number of deposition cycles n. The GPC can be constant over the total amount of applied deposition cycles (Figure 2.8 (a)) which leads to a linear growth of the deposited material. A substrate-enhanced growth appears, if the GPC is higher for small n and decreases with additional cycles until a constant value after sufficient n is achieved (Figure 2.8 (b)).

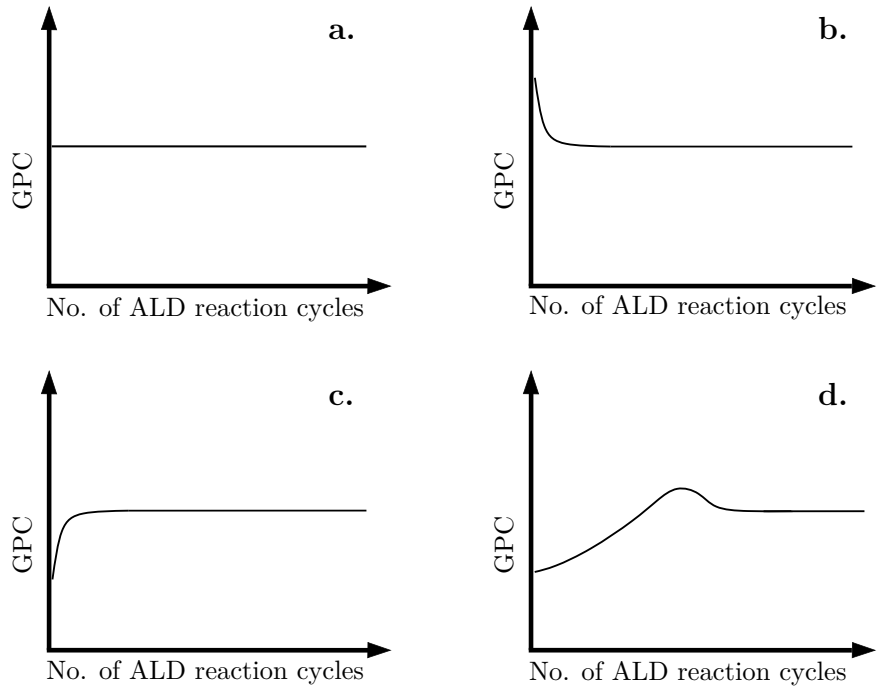

Figure 2.8: ALD growth types: (a) linear growth, (b) substrate-enhanced growth, (c) substrate-inhibited growth type 1, (d) substrate-inhibited growth type 2; after [60].

The substrate-inhibited growth has two types. The first type, as presented in Figure 2.8 (c), shows a small GPC for small n but accelerates with an increasing number of deposition cycles, until, after a threshold of n has been reached,

remains constant. In the second type (Figure 2.8 (d)), the GPC goes through a maximum first, before achieving the constant value for higher n. Considering substrate-inhibited ALD processes, growth rates with a GPC < 1 atomic layer are possible. This is due to the phenomenon of island growth which is a surface-selective growth of the desired ALD material.

Island growth occurs via following two effects:

- Substrates may show low reactivity toward applied reactants, except at areas with active defects. If reactants are only trapped at these areas, islands grow with an increasing number of n until neighbouring islands start to touch each other and a homogeneous layer is built (at threshold number of n) [60].

- Precursor molecules may cause steric hindrances on the surface of the substrate. These hindrances lead to restricted deposition and partial growth of the required ALD material [61].

Experimental results have shown that both effects appeared for the deposition of Al_2O_3 with $AlME_3$ and H_2O (which can be considered as the most typical and studied ALD process) on substrates like silicon, silicon dioxide and zinc oxide [60, 57]. According to [60], active defects can be characterised by an initial radius r_0 in nm. Islands, which start growing symmetrically from the defect centre, gain in diameter with respect to the number of ALD reaction cycles n. During each cycle, the lateral island radius r increases by a constant amount Δr. Radius growth of single islands can be described by the following Equation 2.7.

$$r = r_0 + n \cdot \Delta r \tag{2.7}$$

After a specific number of ALD reaction cycles n_c, neighbouring islands start to touch each other and island coalescence starts. For Al_2O_3-islands on a SiO_2 substrate, the cycle number for coalescence start was found out to be $n_c = 16$ [60]. Considering Equation 2.7 and the experimental results from [60], it is possible to tailor the size of islands to be deposited.
The growth model of single islands is presented in Figure 2.9. Figure a. presents a top view of an island, which is symmetrically growing on an active defect,

whereas b. shows the cross-section along the red dashed line. A top view and cross-section of an island during coalescence at n_c reaction cycles is presented in Figure 2.9 c. and d., respectively.

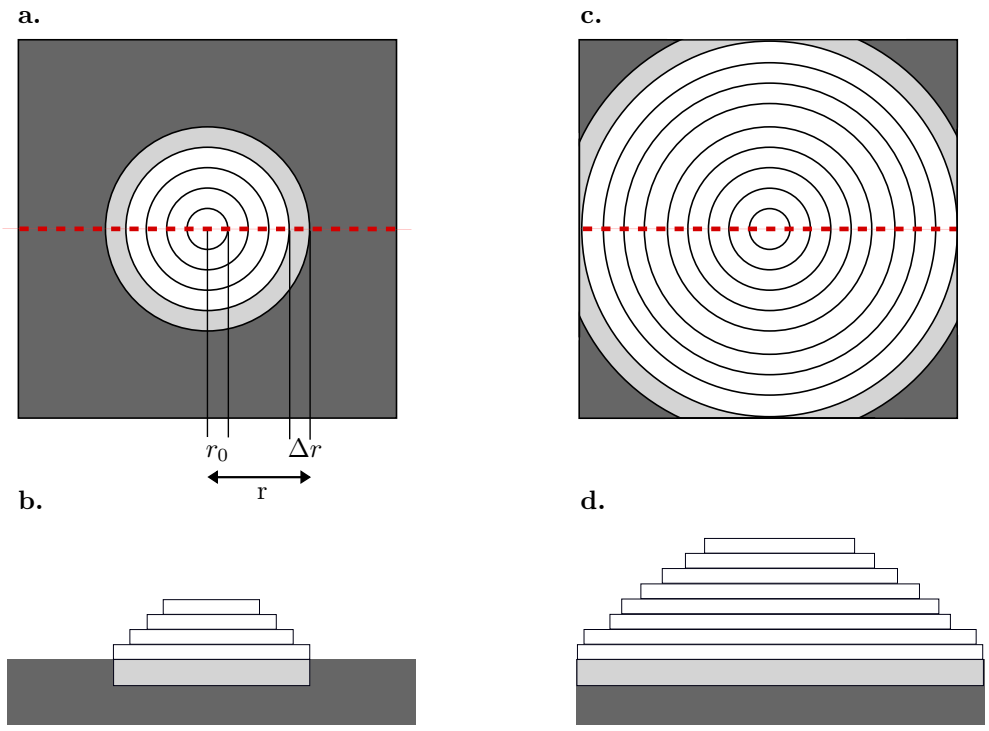

Figure 2.9: Growth model of an island: Top view (a.) and cross-section (b.) of an island with radius r and an increase of Δr per reaction cycle. After n_c reaction cycles, island coalescence begins. Top view (c.) and cross-section (d.) of coalescing island are shown, adapted from [60].

ALD composites

A standard deposition cycle of an ALD process refers to one required material with application of two precursors. Furthermore, ALD enables the fabrication of mixed materials, as well. Subsequent depositions of two ALD materials on one substrate are possible by applying x ALD cycles of the first material and y ALD cycles of the second material. One deposition period of x plus y ALD cycles is defined as *super-cycle*. If x and y are sufficiently high, a nanolaminate consisting of both materials with a thickness of a few nm can be achieved [62].

If x and y are below the threshold of n for a linear film growth (in case of a substrate-inhibited ALD growth), island growth of single materials occurs. This may lead to composites of applied ALD materials instead of nanolaminates

[63, 64]. Schematically-illustrated fabrication of such a nanolaminate and homogeneous composite is presented in Figure 2.10.

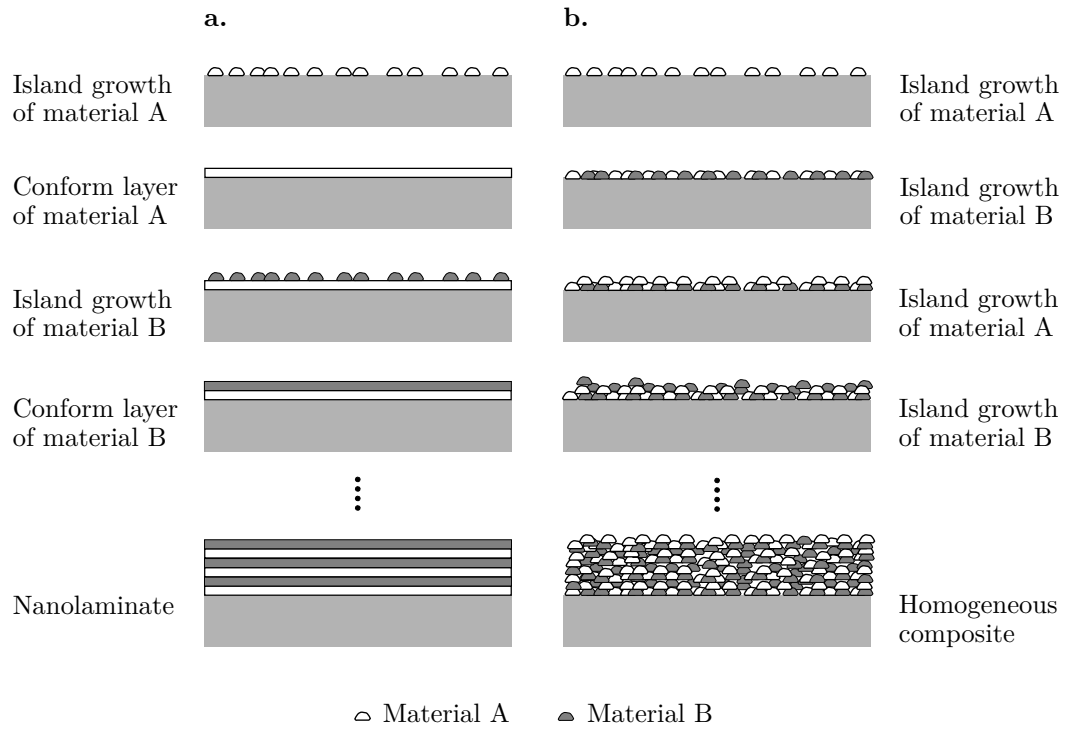

Figure 2.10: Schematically illustrated fabrication of a. nanolaminate with conform layers of materials A and B (stacked) and b. homogeneous composite consisting of islands of deposited materials.

In a., the number of deposition cycles for both materials exceeds the threshold n so that conform layers are built subsequently. In b., the number of deposition cycles for both materials is chosen small enough so that only island growth is achieved. By alternately applying small deposition numbers of both materials, a homogeneous composite without conform layers can be built. Both materials must have a similar ALD-window.

At Fraunhofer IMS, a thermal ALD equipment of the type *R200* from *Picosun Oy* is used. It is a single-wafer reactor with vertical gas flow which allows deposition of metal oxides, nitrides and also metals. Nitrogen (N_2) is used both as carrier and purging gas. Table 2.4 presents a selection of ALD oxides and conductive materials with respective precursors and process parameters which are used in this work.

Table 2.4: ALD materials, precursors and process temperatures used, after [65].

Oxides	Precursor A	Precursor B	Precursor C	ALD-window
Al_2O_3	$AlMe_3$	H_2O	-	220 °C to 380 °C
ZnO	DeZn	H_2O	-	200 °C to 300 °C
Ta_2O_5	$Ta(EtO)_5$	H_2O	-	270 °C to 300 °C
Conductive materials				
Ru	$RuCp_2$	O_2	-	275 °C to 330 °C
TiAlCN	$TiCl_4$	$AlMe_3$	NH_3	300 °C to 330 °C

2.2.2 Laser-Based Micromachining

With decreasing structure size and increasing system complexity, laser-based micromachining has been established as a manufacturing technology in three-dimensional material processing in the last decades [16]. Here, materials are selectively removed by laser irradiation, in which the laser-beam is tightly focused on the material to be ablated, so that finer machining results can be achieved than via common precision mechanics. Laser-based micromachining guarantees reproducible and precise structuring of metals and passivations with feature sizes in µm-range. Additionally, it enables high patterning speeds and direct, maskless machining which, compared to structuring through photo-lithography and etching, simplifies the structuring process by several process steps [66].

Ablation rate depends on both properties of the target material, and the wavelength and pulse length of the laser. Here, pulse widths can vary from milli- to nanoseconds for the short laser pulse range and from pico- to femtoseconds for the ultrashort laser pulse range. Short laser pulse processes are generally dominated by thermal effects. The surface of the target material absorbs the energy of the laser pulse. Due to the heat conduction of the target material, specific temperatures are achieved in order to melt, evaporate or transfer the material into a plasma state. During this process, ablation is caused by evaporation and melt expulsion (as presented in Figure 2.11, a.). These thermal effects may cause damage or melt depositions at the cut edges which are generated by the melt expulsion. Nevertheless, short laser pulse processes meet requirements concerning precision and efficiency for numerous applications, especially in the micromachin-

ing of metals. However, for higher precision standards, ablation processes with ultrashort laser pulses should be utilised. Pico- to femtosecond pulses show extreme intensities within short interaction times. This means that ablation is not caused by continuous evaporation. Instead, the target material is transferred into an overheated liquid which turns into liquid droplets and expanding vapour (as presented in Figure 2.11, b.).

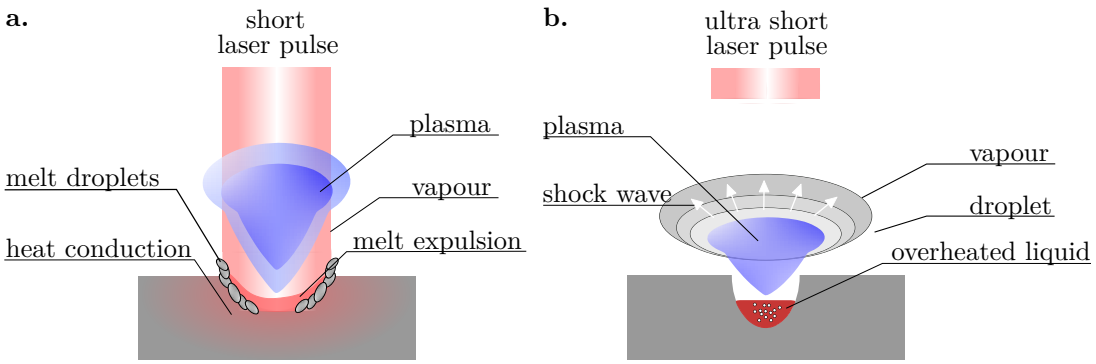

Figure 2.11: Interaction of laser pulse beams with target materials, adapted from [67]: a. short laser pulse process under heat development and generation of melt deposits at the cut edges, b. ultrashort laser pulse process with smaller interaction volume, fewer thermal impacts and minimisation of melt deposits.

The ultrashort laser pulse ablation shows less distinct laser interaction volume and thus fewer thermal impacts. As a result, melt deposits can be minimised or even eliminated. High precision and process control standards of ultrashort laser pulse processes suffer from lower throughput compared to short laser pulse processes. [67]

Also in the field of polymer micromachining, laser ablation is widespread. Patterning of particularly parylene for biomedical applications provided new options for the processing (local opening) of stimulation electrodes and needles. Martyniuk et al. [68] and Schmidt et al. [69] introduced the ablation of parylene with the use of a frequency-quadrupled yttrium aluminium garnet (YAG) laser and an ultraviolet laser system in 1994 and 1995, respectively. In 2009, Schmiedel et al. presented a paper on the combined plasma laser removal of parylene coatings. Here, melt deposition or debris production during laser application could be significantly reduced by a simultaneously-applied atmospheric pressure plasma, which obviated settling of polymer fragments instantly at the appearance [70].

Since precision requirements are fulfilled by millisecond pulse widths for the successful ablation of polymers, metals and dielectrics, a short laser pulse process is used in this work. Selective ablation is achieved by using a green laser ($\lambda = 532\,\mathrm{nm}$) for removing metals and an ultraviolet laser ($\lambda = 355\,\mathrm{nm}$) for removing passivations, oxides and dielectric layers.

3 Concept Development

In this thesis, a process scheme is developed which enables the fabrication of an advanced encapsulation with a self-monitoring function for active implants. In order to obtain a miniaturised encapsulation volume, component level encapsulation is chosen instead of a system level encapsulation with a rigid metal or ceramic housing (as described in Chapter 1.1). This encapsulation concept consists of individual, three-dimensional layers which serve different purposes.
An insulating polymer protects the electrical components of the implant, whereas a thin-film ceramic seals the implant hermetically. The most important component of the encapsulation stack is a humidity sensor layer which enables the self-monitoring function of the presented concept. The sensor consists of three thin films: a bottom electrode, a top electrode and a humidity-sensitive layer in between. In case of water adsorption, a significant change in resistivity can be seen. Due to this sandwich-type sensor structure which is applied to the substrate three-dimensionally, humidity within the encapsulation stack can be detected immediately and on the entire surface of the implant. Compared to the self-monitoring component level approaches with IDE as sensor electrodes on the implant circuit board (discussed in Chapter 1.1), this sandwich-type sensor structure offers a much higher local resolution since. Due to the three-dimensional application of the sensor structure, detection of water is facilitated anywhere on the implant surface. With common IDE sensor structures, this resolution could only be achieved if the total implant surface were equipped with IDE which is very challenging considering the effort for die-level patterning on complex three-dimensional surfaces.
Further advantage is that humidity can be detected one level above the electrical components of the implant which are protected by the insulating polymer for a certain period of time. Thus, defects in the encapsulation can be detected even before the humidity reaches critical components, promotes corrosion and influ-

ences the functionality of the implant. A simplified cross-sectional sketch of this encapsulation stack is presented in Figure 3.1.

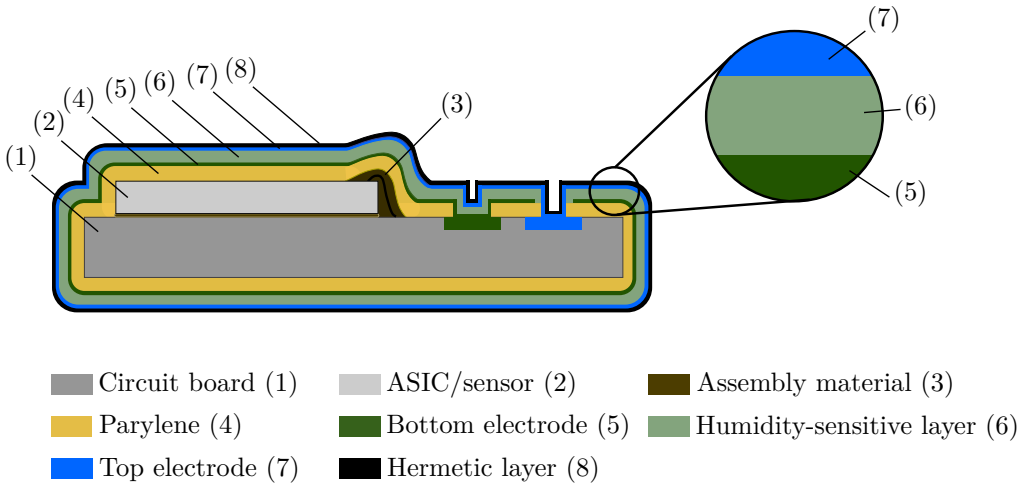

Figure 3.1: Schematic sketch of an active implant, consisting of a circuit board (1) and an ASIC or sensor chip (2) and assembly material (3). Enveloping component-level encapsulation stack is composed of: insulating parylene layer (4), bottom electrode of the humidity sensor layer (5), humidity-sensitive layer (6), top electrode (7) and thin-film ceramic as hermetic sealing layer (8). Inlet presents the magnified sandwich-type humidity sensor structure and the resistive measuring principle (resistance of sensitive layer changes significantly in case of water adsorption which can be detected between the metal electrode layers).

(1) Substrate: Based on the later application, the developed encapsulation concept should be applicable on a three dimensional substrate. Therefore, a circuit board is presented in the schematic sketch as a substrate for the enveloping component-level encapsulation.

(2) Active electronic components: As an additional challenge in the substrate topography to be coated, sensor chips or ASICs can be found on the circuit board. These components increase the implant surface area, the complexity of surface topography and the number of different materials used. Thus, active electronic components complicate the deposition of individual thin-film layers.

(3) Assembly material: For the assembly of active components, assembly material with approval for use in specific medical devices is required. Consider-

ing process temperatures of subsequently deposited encapsulation layers, high-temperature stable materials are needed.

(4) Parylene: This insulating polymer with good humidity barrier properties is deposited directly on top of the electronic components of the active implant and serves as an isolation layer between these components and the following humidity sensor layer. Additionally, it rounds sawn die edges and simplifies the complex material mixture of the implant. Thus, further deposition of thin-film layers can be applied more effectively (see Chapter 3.2.1).

(5) Bottom electrode: The bottom electrode of the humidity sensor layer is a thin metal film which is applied three-dimensionally on the parylene layer. It is connected to the respective contact pad on the circuit board through an opening in the insulating parylene layer so that an inter-layer connection (ILC) is achieved during the deposition process of the top electrode metal (see Chapter 3.2.2).

(6) Humidity-sensitive layer: The humidity-sensitive layer is a thin-film ceramic composite with temperature stability of up to at least 300 °C. In case of water adsorption, it shows a significant change in resistivity which can be measured as a sensor signal. Even the smallest amounts of water due to defects in the hermetic sealing are detected immediately anywhere in the encapsulation. Therefore, the sensitive layer is three-dimensionally applied to the implant and surrounded by conductive layers. Thus, a resistive sensing mechanism is promoted. The humidity-sensitive layer is the main component since it enables the self-monitoring function of the presented encapsulation stack. The development of such a humidity-sensitive layer is a major focus of this thesis.

(7) Top electrode: The top electrode of the humidity sensor layer is also a thin metal film which is applied three-dimensionally on the humidity-sensitive layer. Connection with the respective contact pad on the circuit board is carried out by openings of the underlying layers so that ILC is achieved during the deposition process of the top electrode metal (see Chapter 3.2.2).

(8) Hermetic sealing: This thin-film ceramic layer serves as the main humidity barrier of the presented encapsulation stack. Three-dimensionally deposited,

it protects the active implant from absorbed humidity within an outer silicone coating, which is necessary for an appropriate shape of the device (see Chapter 3.9) but not considered in this thesis.

Resistive Sensing Mechanism

The most common two humidity sensing mechanisms are capacitive and resistive sensing mechanisms. Both could be used for the detection of humidity with the presented sandwich-type sensor structure in this encapsulation concept. Regarding the large sensor area of the sensor structure in this work which represents the surface area of an active implant ($\approx 100\,\mathrm{mm}^2$), one mechanism is still more appropriate than the other.

As described in Chapter 2.1.1, capacity-sensitive type humidity sensors utilise the increase of the dielectric constant in case of water adsorption. In case of a small local defect in the hermetic sealing and ingress of water molecules into the sensitive layer, only a small part of this layer is able to react and change its electrical properties. The equivalent circuit in Figure 3.2 a. presents the parallel connection of several capacitors, each of them representing a local area in the sensitive layer. Considering the equation for the total capacitance of several capacitances in a parallel manner, the increase of capacitance for one of these capacitors would not lead to a significant change of the total sensor signal.

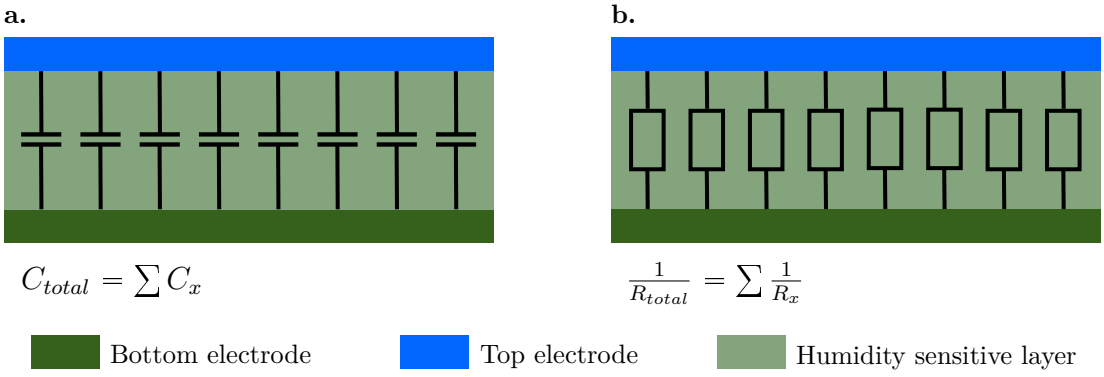

Figure 3.2: Equivalent circuits for capacitive sensing mechanism in a. and resistive sensing mechanism in b., in which each parallel capacitor or resistance stands for a small local defect in the sealing layers above.

In Figure 3.2 b. the equivalent circuit of a resistive-sensitive type humidity sensor is presented. Each resistance represents a local area again. As described in Chapter 2.1.1, for impedance-sensitive type humidity sensors the decrease of elec-

trical impedance or the increase of conductance of the sensing material is crucial. In a circuit with resistors which are connected in parallel, the total resistance is based on the smallest resistance in the circuit. This means that one local defect could decrease the resistivity of a single resistor, thus increase the conductivity of the sensor layer and still lead to a great change in sensor signal. Therefore, a resistive sensing mechanism is chosen in this work.

Failure Mechanism

In case of a mechanical defect in the hermetic ceramic and upper metal layer, water can penetrate into the encapsulation stack until it reaches the humidity-sensitive material between the sensor electrodes where it changes its electrical properties. By means of a resistive humidity measuring principle, adsorbed water can be detected, which indicates a leakage in the hermetic sealing.

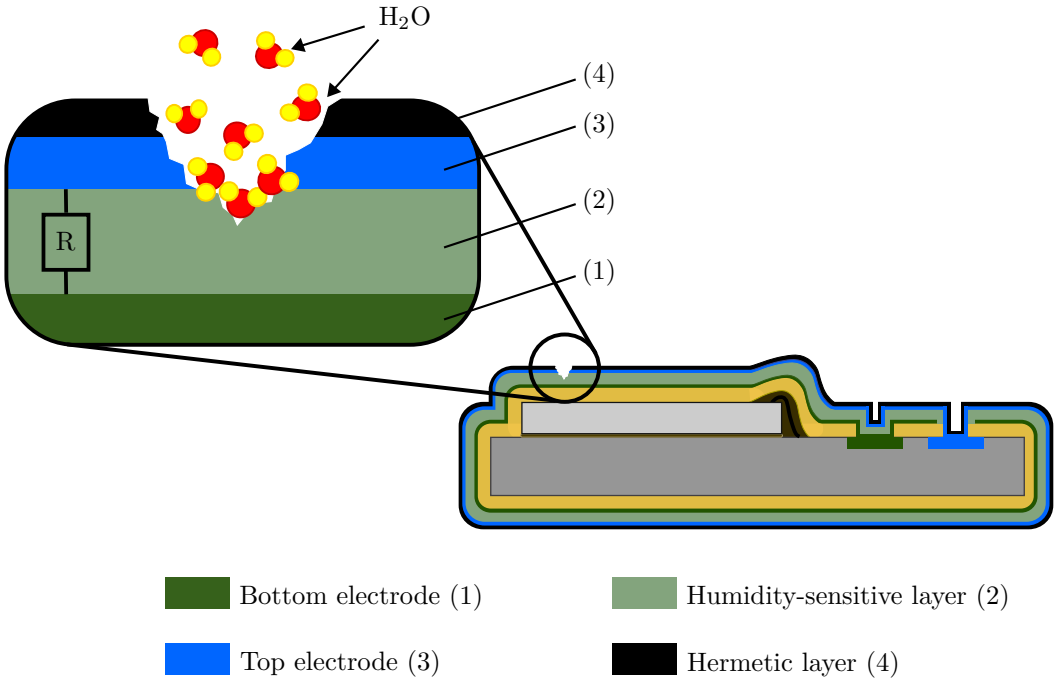

Figure 3.3: Failure mechanism of the component level encapsulation concept with a mechanical defect in the hermetic layer and top electrode (illustrated in the inlet): by adsorbing water molecules, the conductivity of the humidity-sensitive layer increases significantly. The resulting change in resistance between the metal electrodes reveals a degradation in the upper layers of the encapsulation stack.

In Figure 3.3, an example for a mechanical defect in the upper two layers is presented in a simplified sketch. Such defects can be caused by false handling with tweezers or defects in the thin-films which lead to accelerated local corrosions. Water can penetrate through the smallest cracks and delaminations. As soon as water molecules reach the humidity-sensitive layer, they change the conductivity of the sensitive layer within a local spot which results in a sensor signal.
Even if water penetrates through the thin ceramic sealing and the humidity sensor layer, the electronic components of the active implant are protected by the polymer between implant surface and humidity sensor layer. As a humidity barrier, this polymer prevents corrosion for a certain period of time until the implant with degraded encapsulation can be removed from the body.

The parylene coating is achieved by a CVD process (Gorham process, Chapter 2.2.1), whereas the layer stack of bottom-electrode, humidity-sensitive layer, top-electrode and hermetic sealing material is processed by ALD (Chapter 2.2.1). Micromachining of thin-film layers is accomplished by laser ablation. Before the whole process flow is presented in detail, process limitations are considered in order to discuss chosen processes and materials.

3.1 Process Limitations

The monitoring sensor for humidity detection should be integrated within the implant encapsulation, which consists of a hermetic thin-film stack. Thus, the fabrication of such a humidity detecting element cannot be separated from the encapsulation process directly on top of an active implant. Active implant feature at least one ASIC for sensor signal readout. As such an ASIC is fabricated in complementary metal oxide semiconductor (CMOS) technology, post-CMOS requirements have to be taken into account in order to maintain the chip functionality while encapsulation processes are applied. Also, operation conditions of assembly materials, for example die-bonding glues, provide temperature budgets which have to be complied with. On the technological side, an additional limitation occurs through the present substrate which is a silicon circuit board equipped with an ASIC. While standard microsystem technologies are oriented for processes on plane wafers, only technologies which also enable handling on

die-level and provide adequate results at the same time can be utilised for the development of this concept. Resulting limitations with regard to different categories are presented in the following chapters.

3.1.1 Limitations concerning post-CMOS Processing

Considering post-processing of substrates which include CMOS components, two general requirements have to be taken into account:

- limited temperature budgets and
- protection against damages or contaminations.

Post-processing CMOS components may lead to undesired annealing due to applied temperatures in the following process steps. For standard CMOS technologies with aluminum-based metallisation, modifications of electrical characteristics change depending on annealing temperature and duration. Typical temperature budgets from the literature are listed in Table 3.1. In each reference an approximately 10 % degradation in metallisation resistance was recorded, whereas transistor properties remained unchanged.

Table 3.1: Temperature budgets for post-processing of 250 nm to 350 nm CMOS technologies.

Technology	Temperature	Time period	Reference
350 nm	525 °C	90 min	[71]
250 nm	475 °C	30 min	[72]
250 nm	450 °C	60 min	[72]
250 nm	425 °C	360 min	[72]

Considering the Al based metallisation of the 350 nm CMOS-ASIC used, an overall temperature of only 400 °C shall not be exceeded. Thus, process times of 360 min and above can be applied without any risks of negative modifications due to processes at further elevated temperatures.
In this work, only ALD processes are used for the deposition of the thin-film encapsulation stack. Process temperatures of up to 300 °C for utilised dielectrics or oxides (for example Al_2O_3, ZnO, or Ta_2O_5) and up to 400 °C for conductive

materials (TiN, TiAlCN or Ru) are required, while deposition times (depending on desired layer thickness) do not exceed approximately 300 min. Thus, required ALD processes fulfil the present temperature budget easily.

Patterning of ALD-layers is accomplished by laser micromachining (see Chapter 3.2.2). Since the local removal of dielectrics or conductive materials is only required on specific spots on the circuit board, the risk of damaging or contaminating the CMOS-ASIC is considered to be negligibly low.

3.1.2 Limitations concerning post-Assembly Processing

Irrespective of limitations concerning post-CMOS processing, there are more severe limitations considering the assembly material on the implant to be coated. Assembly material like die-bond glues or glob-top and underfill materials for mechanical stabilisation of wire bonds and stud-bumps, respectively, show advanced humidity-barrier and temperature-stable properties for an enlarged field of applications. Nevertheless, further processing with microsystem techniques of assembled devices has no yet been established. Therefore, finding suitable assembly materials which withstand mechanical and thermal stress of such further processing, is mandatory.
Occurring challenges during processing with microsystem techniques might be outgassing, degradation at high process temperatures and, thereby, loss of performance. In order to avoid these problems, the following requirements have to be fulfilled by the assembly material:

- die-bond and glob-top/underfill properties,
- temperature stability of up to 300 °C for 300 min,
- no outgassing,
- no deformation during application of high temperatures,
- easy handling and
- appropriate curing time and temperature.

Most of the commonly-used die-bond materials feature continuous temperature stabilities at 200 °C with short-term operations at only 300 °C. High temperature epoxies with continuous operating temperatures above 200 °C often include various filler materials, which support mechanical properties such as temperature stability. However, most filler materials are not approved for post-processing with microsystem techniques, since the risk of system contamination is too high. Therefore, only pure epoxies with high-temperature stabilities are selected. One epoxy glue by Polytec EP, the *EP 642*, meets all requirements and, thus, is selected as assembly material in this work. With a permanent stability at 250 °C and a short-term stability at 350 °C for approximately up to six hours, this electrically non-conductive glue is stable for upcoming coating steps by ALD at temperatures of around 300 °C (as presented in [18]). The same assembly glue is used as die-bond and as glob-top material for wire-bond protection in order to keep the mixture of materials on the assembled device as simple as possible. Here, a non-thixotropic version is chosen which enables easier covering of the wire-bonds. As a frozen composite, the *EP 642* is a one component glue which facilitates handling and storage. Curing times and temperatures can be applied to the circuit board or used chips of the implant without any problems. The most important properties of *EP 642* after curing time are summarised in Table 3.2.

Table 3.2: Properties of used epoxy glue *EP 642* after curing process, after [73].

	Unit	Technical data
Curing time	min	15
Curing temperature	°C	180
Shore hardness (D)	-	85
Continuous operating temperature	°C	-55 / +250
Maximum operating temperature	°C	-55 / +350
Decomposition temperature	°C	+410
Water uptake (24 h at 23 °C)	%	0.3

The choice of assembly material influences the choice of following process steps, as well. Applicable process temperatures and times are depend on the maximum operation limits of used epoxy glue which is 350 °C for short periods [73]. Hence, cured assembly material was tempered at 300 °C for 300 min, in order to prove

sufficient temperature stability for various ALD processes at $\leqslant 300\,^{\circ}\mathrm{C}$ up to 300 min.

3.1.3 Challenges concerning Processing on Die-Level

Microsystem technologies serve a very wide range of processing possibilities on wafer-level. With regard to the structures to be implemented, various deposition techniques like chemical or physical vapour deposition (sputtering) can be applied for layer generation. These techniques are utilised not only on wafer-level, but also on die-level which is often related to great handling effort or even additional process development. Especially if a three-dimensional processing of a die is required, a sufficient step coverage is mandatory for a conformal coating of not only surfaces, but also of the edges of a silicon die. Therefore, implementation of this encapsulation stack of thin-films is strictly limited to coating techniques, which allow highly conformal depositions. Additionally, a good adhesion of the individual layers to each other is a prerequisite.
As discussed in Chapter 2.2.1, only CVD processes provide required deposition qualities concerning isotropy. CVD is utilised for substrate coating with parylene. Thus, the complex surface and sharp die-edges of the circuit board and the assembled ASIC are simplified and rounded by this chemical inert and comparatively thick polymer film. ALD, which is a variant of CVD, is utilised for further three-dimensional deposition of functional thin-films. Temperature budgets and material selection for both techniques fulfil limitations of Chapter 3.1.1 and 3.1.2.

On wafer-level, patterning of applied layers can be easily accomplished by photo-lithographic patterning and etching processes. On die-level, however, photolithography necessitates manual handling in each sub-step, so that process complexity and effort increase significantly. Lift-off processes with sacrificial materials are not appropriate, either, since layer generation is achieved by CVD processes. These serve highly isotropic coatings (unlike layers achieved by sputtering). As a result, the sacrificial material is completely covered so that no access area for etching media exists. As an alternative technique with only one process step, laser ablation has been established for local removal of polymers, dielectrics and metal layers. Compared to patterning by photo-lithography, laser ablation enables patterning with only one process step which simplifies the complexity of

die-level processing and delivers comparable results. Micromachining by laser ablation on die-level is explained in detail in Chapter 3.2.2.

3.2 Process Flow

Considering technical process limitations (see Chapter 3.1), a process flow for the implementation of an encapsulation stack with an integrated humidity sensor layer is presented. Therefore, appropriate microsystem processing techniques are evaluated and chosen for coating and patterning specific materials. The process flow consists of five deposition processes with additional micromachining steps. An overview of the deposition processes is presented in Figure 3.4.

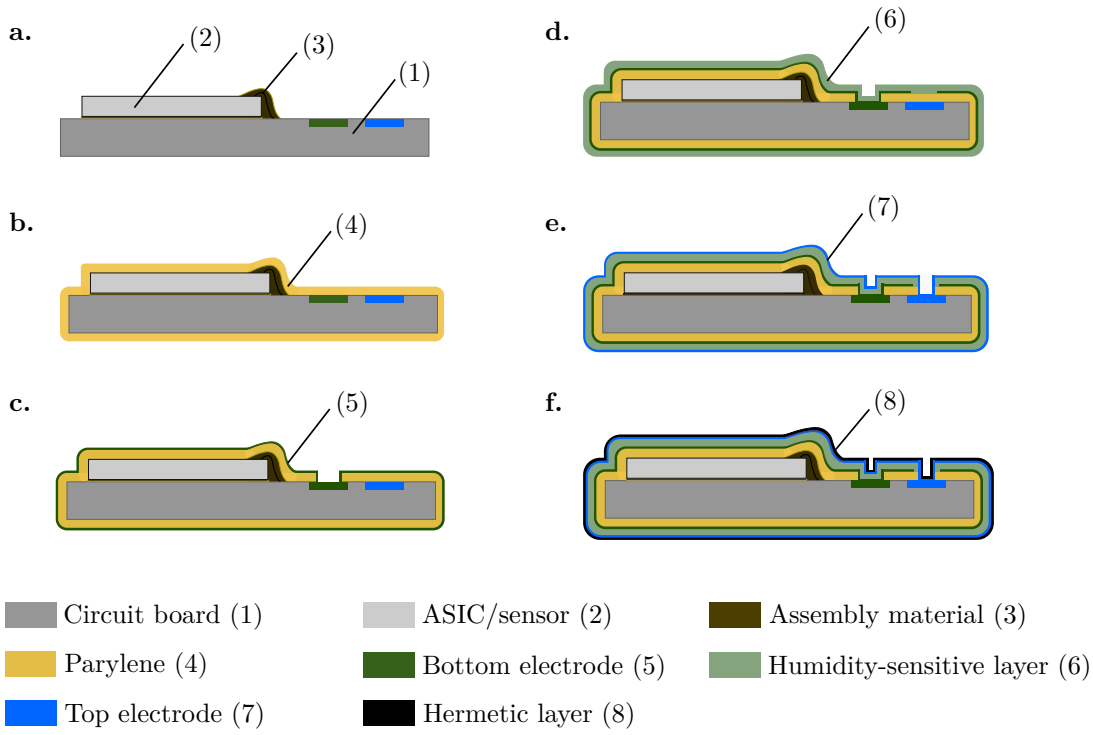

Figure 3.4: Schematic process flow presenting five deposition steps of the encapsulation concept with isolating parylene, integrated humidity detecting sensor layer and hermetic ceramic.

Starting with an assembled active implant, consisting of a circuit board, CMOS-dies and sensors, and assembly material (a.), the substrate is ready for preparation with a parylene coating (b.). After the substrate surface has been smoothed and simplified through the polymer coating, the first conductive metal layer (bottom

electrode (c.)), the humidity-sensitive layer (d.) and the second conductive metal layer (top electrode (e.)) are applied to the substrate. ILC of conductive layers with respective contact pads on the circuit board are achieved by laser ablation. By locally and selectively structuring the insulating layers, openings to underlying pads are produced, so that an electrical contact results automatically through the deposition of conductive material (see Chapter 3.2.2). An electrical connection of the top electrode without any shorts to the bottom electrode layer is guaranteed by a developed sequence of laser ablation and deposition steps which is presented in Chapter 3.2.2.

Finally a hermetic and biocompatible and biostable ceramic is deposited on top of the fabricated stack as a sealing (f.). Among all work packages in this process flow, the following key processes are considered in more detail:

- Substrate preparation with parylene,
- micromachining by laser ablation,
- ILC of conductive layers,
- implementation of humidity detecting sensor layer, and
- hermetic sealing.

3.2.1 Substrate Preparation with Parylene

Outgoing from the substrate, the surface reveals challenging properties. Starting with a complex topography (for example due to high aspect ratios and sharp edges of dies or the circuit board used), the coating of such a substrate with a stack of very thin functional films does not seem to be promising from a mechanical point of view. Sawn die edges or microscopic defects on the surface of the assembled device can lead to cracks, pinholes and delamination of atomic layer deposited thin films with thickness of only tens of nanometers. In addition, the combination of CMOS chips, the implant circuit board and epoxy assembly glue reveal a complicated mixture of various materials on the implants surface. Considering incubation times of chemical vapour deposited materials, a conformal coating of different implant elements does not seem to be promising with thin ALD layers, either. Therefore, a simplified and smoothed surface is required and

achieved by substrate preparation with parylene.
A strong adhesion to the substrate surface is mandatory. Additionally, the material should flatten every unevenness and fill gaps of the substrate during the deposition process. Thus, voids can be avoided by which the risk of water vapour condensation on the substrate surface is minimised. Without condensation or migration of ions, corrosion effects can be prevented on the voltage carrying components and contact pads [16, 6]. Highly isotropic deposition of a chemically inert and high-ohmic parylene fulfils these requirements.

Parylene is a polymer which is deposited by chemical vapour deposition at low temperatures (commonly at room temperature) and, thus, allows coatings in almost unlimited application fields. By depositing such a polymer layer directly on top of a non-encapsulated active implant, complex topographies with compositions of different materials can be simplified to one smooth surface consisting of only one material. Due to the Gorham process (a variant of CVD), pinhole-free and three-dimensional coating of complex implant surfaces is possible. The most important properties of parylene are:

- gas and moisture barrier,
- electrical insulation,
- high surface conformability,
- pinhole free application,
- low dielectric constant,
- biocompatibility and bio-stability,
- sterilisability and
- no outgassing of volatile chemicals.

There are several types of parylene. Consisting of the same raw material but with slightly modified chemical structure, these types represent specific advantages concerning requirements for electrical, mechanical or temperature stability. A summary of the most common parylene types with respective characteristics is presented in Table 3.3.

Table 3.3: Most common parylene types and typical properties, after [74, 75, 76].

	N	**C**	**D**	**F**
Physical and mechanical properties				
Density in g/cm^3	1.110	1.289	1.418	1.32
Elongation at break %	250	200	200	200
Water absorption in % (day)	0.01	0.06	< 0.1	< 0.009
Electrical properties				
Dielectric strength in V/mil at 1 mil	7.000	5.800	5.500	5.500
Volume resistance (23 °C, 50 %RH in Ω cm)	$1 \cdot 10^{17}$	$6 \cdot 10^{16}$	$2 \cdot 10^{16}$	$2 \cdot 10^{17}$
Surface resistance (23 °C, 50 %RH in Ω cm)	10^{15}	10^{15}	$5 \cdot 10^{16}$	$5 \cdot 10^{15}$
Dielectric constant (at 60 Hz)	2.65	3.15	2.84	2.25
Dissipation factor (at 60 Hz)	0.0002	0.019	0.003	0.002
Barrier properties (gas permeability)				
(cc x mm)/(m^2 x day x atm)				
Nitrogen	7.7	0.37	1.77	4.85
Oxygen	11.81	2.8	12.6	23.5
Carbon dioxide	84.25	3.03	5.12	95.6
Moisture vapour transmission				
(g x mm)/(m^2 x day) at 37 °C, 90 %RH	0.59	0.06	0.1	0.23
Thermal properties				
Melting temperature in °C	410	290	380	> 460
Linear coefficient of expansion in ppm/°C	69	35	38	36
Continuous operation temperature in °C	90	125	160	350
Biocompatibility				
proven	yes	yes	N/A	yes

A difference regarding the adhesion of the parylene types on various substrates is not apparent from the literature. Due to its outstanding chemically inert properties and biocompatibility, parylene C is an often-used polymer for biomedical and lab-on-chip applications [77]. It has been well established in the field of encapsulation of medical devices in the last decades as well [20, 24]. Even more advanced barrier properties have been achieved by applying bi-layer encapsulation stacks with parylene and an additional material, most commonly Al_2O_3 [22, 19, 78]. Nevertheless, as the first coating layer of this encapsulation stack, further requirements for the parylene have to be taken into account. Considering

upcoming deposition steps of functional thin films by ALD, temperature stability is the decisive argument for the choice of parylene which is why parylene C, with a continuous operation temperature of only 125 °C, is not sufficient for this concept. With its comparably good electrical, physical and barrier properties and the highest temperature stability among all parylene variants (continuous operation temperature of up to 350 °C), parylene F is chosen as a suitable polymer for the first layer of the developed encapsulation concept. In this work, parylene F has been deposited on the circuit boards by *Heicks Parylene Coating GmbH*. Substrates were cleaned by hydrofluoroether (HFE) treatment before the Gorham process was applied (see Figure 2.5). Thus, parylene F deposition with a thickness of approximately 3 µm could be achieved at 25 °C [79].

3.2.2 Conductive Electrode Layers by ALD

The encapsulation concept presented in this work consists of a thin film layer stack of ALD materials which includes an integrated sandwich-type humidity sensor. Therefore, functional conductive layers have to be deposited and connected to the circuit board metallisation. In order to enable the connection of metal layers with respective contact pads, underlying dielectrics and polymers have to be removed locally, first.
Should processing single dies become necessary, standard microsystems technology processes are not always suitable. Die-level patterning via lithography requires at least masking, exposure, developing and etching steps and costs much effort due to manual handling and adjustment in each sub-step. If common precision mechanics do not deliver sufficient results either, laser ablation can be used. This alternative technique with only one process step (without the use of photoresist) has been established as a manufacturing technology in three-dimensional material processing for systems with decreasing size and increasing complexity [16]. The finest machining can be achieved via laser irradiation where the laser-beam is tightly focused on the material to be ablated (see Chapter 2.2.2). Micromachining by laser-ablation guarantees precise and reproducible patterning of metal and passivation layers with high patterning speeds and maskless processing.

In this work, selective ablation of parylene, metal layers or dielectric layers is achieved by laser ablation with *EzLaze II*, a laser cutting system by *New Wave Research*. The system obtains two laser wavelengths which enable a selective cut-

ting of metal lines or layers with the green laser (λ = 532 nm) and removing of passivations, oxides and dielectric layers with the ultraviolet laser (λ = 355 nm). With different trigger modes, single-shot with 1 Hz or burst-mode with 5 Hz, and a wide energy range with precise energy control, the system facilitates fast and precise material removal with high repeatability. Cut sizes may be selected within a range from 2 µm x 2 µm up to 100 µm x 100 µm. [80]
The laser module is mounted directly over the microscope objectives. While the green laser can be applied through any regular objective, the UV laser can only be applied through a specific objective with a magnification of 100 x.

Besides the opening of the first isolation layer, further layers of the encapsulation stack also have to be opened at concrete spots with specific cut sizes in order to connect two conductive layers with respective pads on the circuit board. Therefore, the use of laser ablation is considered for patterning conductive and insulating layers as well. Depending on the thickness of the material to be ablated, the energy level of the laser beam has to be adjusted. In Figure 3.5, the process flow for contacting metal electrode layers through subsequently opened areas is presented in eight steps.
After the parylene has been deposited on the whole surface of the substrate (a.) and subsequently removed on top of the contact pad for the bottom electrode layer (b.), an O_2-flash is applied for cleaning the metal surface from the remaining polymer and forming smooth parylene edges with a minimised amount of residuals at the opened area (c.). In parallel, the surface of the parylene film is slightly roughened by the plasma. The roughness promotes the adhesion of the ALD metal, which serves as electrically connected bottom electrode layer (d.). In step e., an appropriately wide area of the bottom electrode has to be ablated selectively above the top-electrode-contact-pad. The deposition of the humidity-sensitive layer (also by ALD) follows (f.). Thus, the parylene layer and the humidity-sensitive layer form a stack of isolating materials where the bottom electrode was removed. After the removal of both isolating layers with a smaller ablation area than in step e., the opening of the top-electrode-contact-pad on the circuit board is guaranteed (g.). This opened pad is coated with a further metal layer (top electrode) in step h. for an electrical connection without any shorts to the bottom electrode layer.

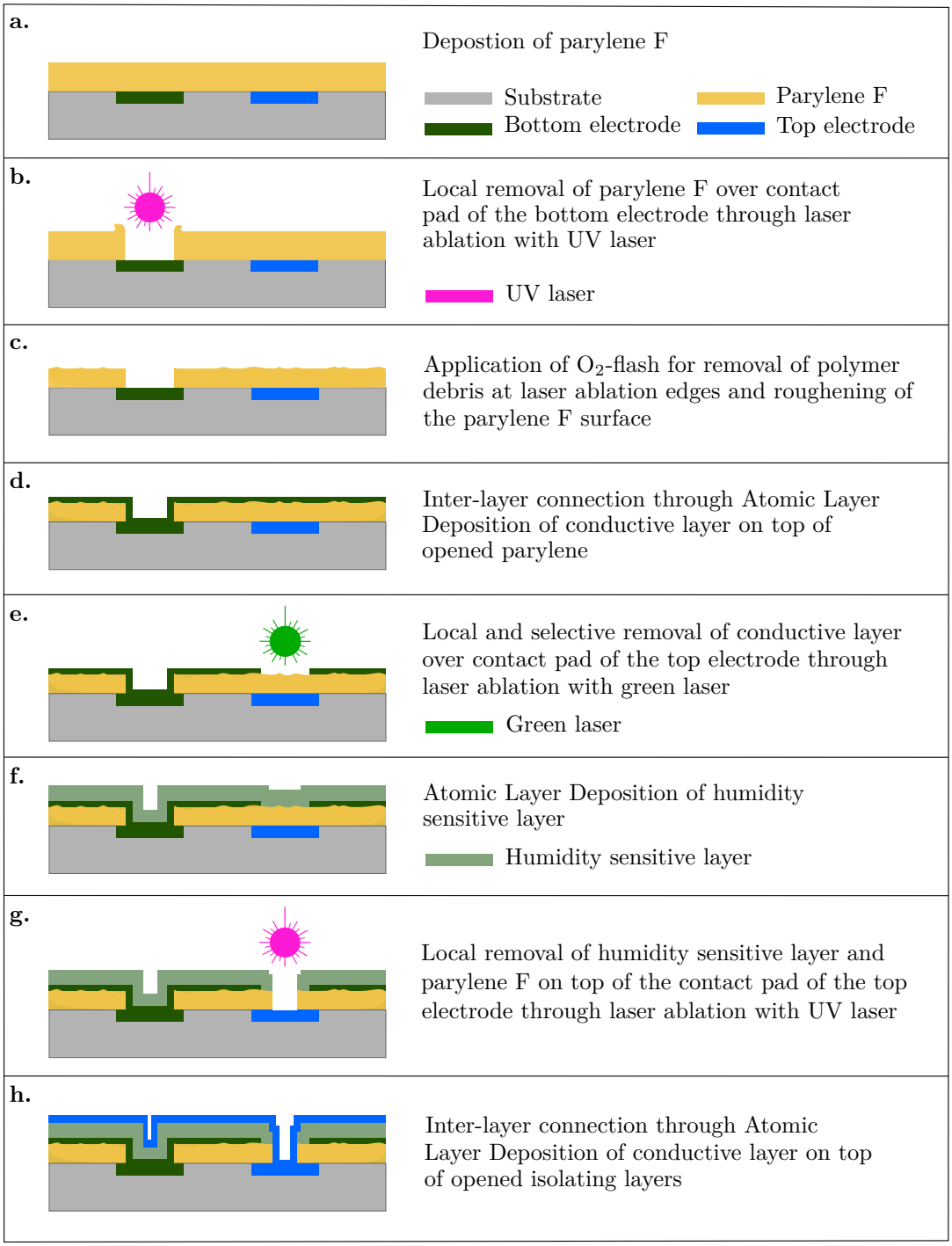

Figure 3.5: Schematic process flow for opening of parylene or ALD layers by local and selective laser ablation (using a green or a UV laser) and further contacting with conductive thin film layers.

Further information about the parameters used for laser ablation of various materials are presented in Chapter 3.3.3.

3.2.3 Humidity-Sensitive Layer by ALD

The humidity-sensitive layer serves to detect invaded water between both conductive electrode layers. Generally, humidity sensitivity of a material depends on the signal change after the adsorption of water molecules, regardless of the transduction type. In this work, the development of a material, whose conductivity is significantly changed due to water adsorption, is required so that a degradation of the hermetic sealing can be detected by exceeding a threshold value. Here, certain technological demands need to be fulfilled.

Technological demands:

- Deposition of the humidity-sensitive layer has to be highly isotropic and show sufficient step coverage since application on die-level is required.
- The humidity-sensitive layer has to withstand further process temperatures. and
- Deposited humidity-sensitive layer must show suitable adhesion and growth behaviour on the electrode layer underneath.

Resistive humidity measurements are often established with polymer-based materials. Especially porous polymer films and polymers with specific dopants show excellent linearity between the amount of adsorbed water molecules and the measured resistance [81]. Nevertheless, these technological demands do not correspond to the deposition process and the temperature stability of such a humidity-sensitive film. Polymers are commonly applied by dipping or spin-coating processes which are not appropriate for conformal coating of a three-dimensional substrate. Additionally, they show poor stability and insufficient chemical inertness at high temperatures. Regarding the process flow of this encapsulation concept, degradations would occur which is why polymers are not considered as a humidity-sensitive layer in this work.

In contrast, ceramics show chemical inertness and stability at high operation temperatures and can be deposited by CVD processes. By showing resistive or capacitive changes proportional to the amount of adsorbed water molecules, ceramic materials can be used as humidity-sensitive layers with a wide measuring

range and high temperature stability [81]. Composite ceramics (also called multiphase ceramics) combine various materials, which are normally not in chemical interaction with each other, in order to tailor sensor behaviour. In ordinary ceramic technology most common raw materials are oxides (for example Al_2O_3, TiO_2, ZnO, SnO_2, or SrO) or carbonates (for example $BaCO_3$, $SrCO_3$, Na_2CO_3, or $MnCO_3$) [47, 82]. With these raw materials, production of porous ceramic composites with specified pore size and distribution can be implemented. The manufacturing process of such a ceramic composite, as presented in Figure 3.6 a., includes complex mechanical processes and sintering steps at temperatures above 1000 °C [83, 84]. Regarding technological demands for the humidity-sensitive layer in the encapsulation concept of this work, this strategy is not applicable. Therefore, an ALD process has been developed as a fabrication method for composite ceramics. This process simplifies the preparation and deposition steps enormously, as presented in Figure 3.6 b..

Besides technological demands, humidity-sensitive layer development by means of ALD also takes application-oriented demands into consideration.

Application-oriented demands:

- The humidity-sensitive layer has to show high reliability and service life (ideally up to several years) under implantation conditions (constant body temperature of about 37 °C).
- The humidity-sensitive layer has to show a significant change in conductivity due to water adsorption if a threshold is exceeded.
- The humidity-sensitive layer does not need short response times of seconds or even a few minutes.
- The humidity-sensitive layer does not meet any requirements regarding hysteresis since operation is planned only during adsorption procedures, not during desorption.
- Resistance in dry air (considering application in test structures) or in intact encapsulation (considering application within implant encapsulation) should be in the MΩ range [82].

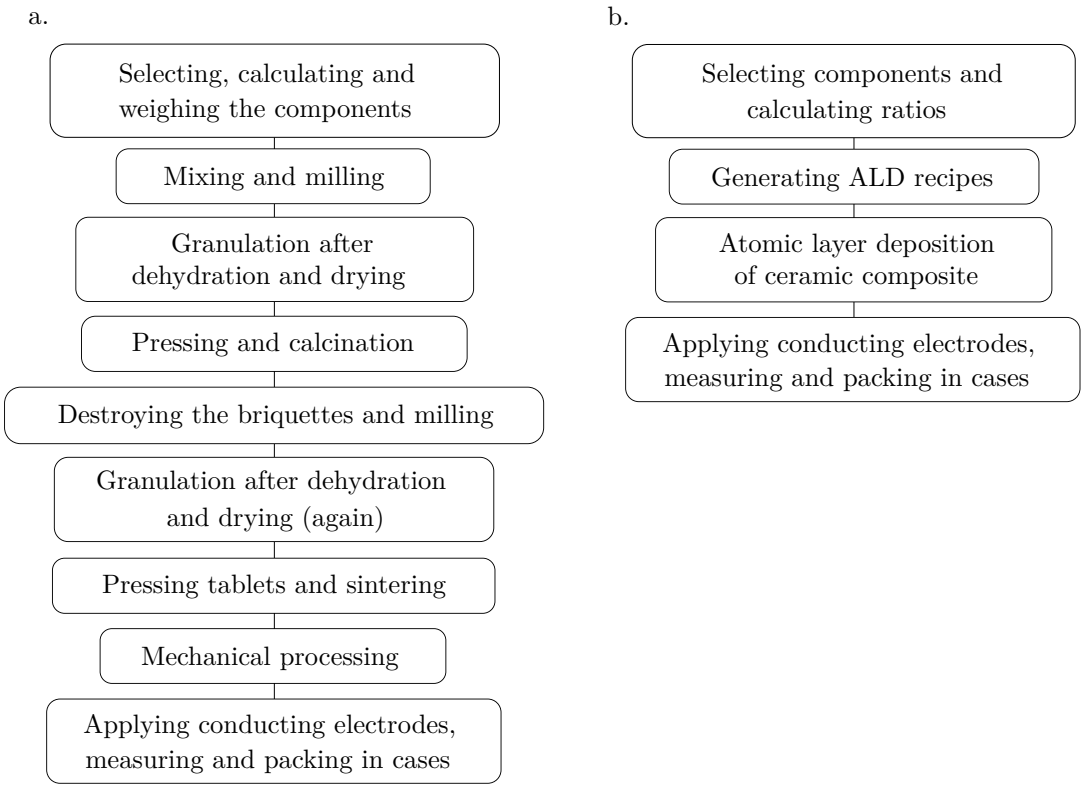

Figure 3.6: Classic manufacturing process of a ceramic composites consisting of at least two components for application in humidity sensors (after [47]) in a.; manufacturing process of a ceramic composite by ALD in b..

The usage of ALD materials already fulfil the technological demands, such as isotropic deposition and compatibility with further process temperatures and materials. Nevertheless, application-oriented demands, for example sensor behaviour during water adsorption and related sensitivity, need precise and targeted tailoring of the sensor layer. It is known that humidity sensitivity of ceramics depends on grain sizes, junctions between the grains and the corresponding amount of active sites for adsorption of water molecules, regardless of the transduction type (see Chapter 2.1). If these two conditions are combined, it becomes apparent that a sensitive ALD semiconductor, dielectric, or a semiconductor-dielectric mixture needs to be developed as a humidity-detecting sensor layer.

Based on ALD layer properties, such as high conformity and density even on substrate surfaces with high aspect ratios (see Chapter 2.2.1), production of granular ALD ceramics cannot be implemented with standard processes. Single

phase metal oxides are often amorphous and have no granulation. Single phase semiconductors may show grain boundaries if they are poly-crystalline but grain sizes and forms strongly depend on the process temperature, annealing steps, crystallinity of the semiconductor [85] and structure of the substrate on which the semiconductor grows [86].

Regarding the choice of oxides and semiconductors, which are applicable in the ALD used, only a few materials can be considered as humidity-sensitive material. Currently available oxides are ZnO, Al_2O_3 and Ta_2O_5. As a ph-sensitive oxide, Ta_2O_5 is generally used in ph sensors [87] and is not established in gas sensors. In contrary, n-type semiconducting ZnO and Al_2O_3 are well established materials for measuring humidity, but only if the material structure allows the adsorption of water vapour at the grain boundaries or through porosity. Therefore, ZnO and Al_2O_3 are chosen for the fabrication of a multiphase composite under specific process restrictions.

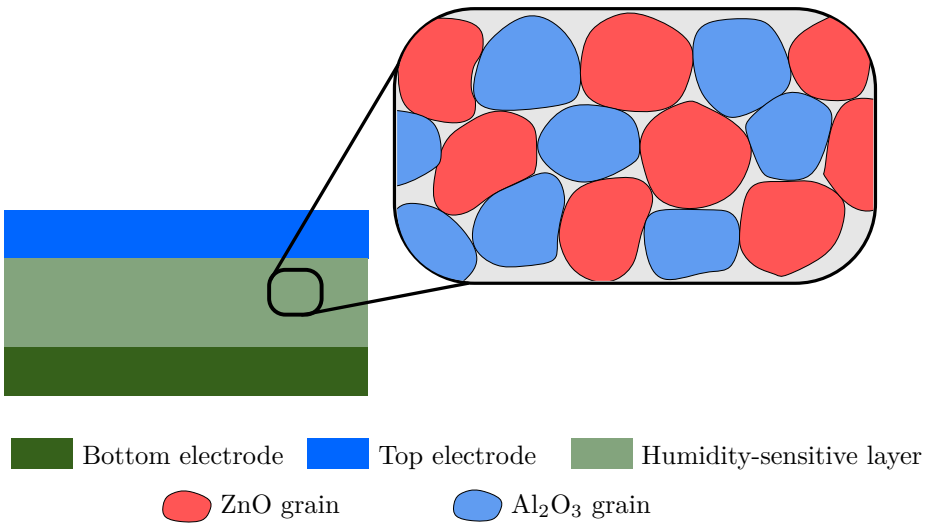

Figure 3.7: Simplified sketch of the aimed sandwich-type sensor structure: inlet magnifies the humidity-sensitive multiphase-composite which consists of dielectric Al_2O_3 and semiconducting ZnO grains.

In order to guarantee a granularity and associated grain boundaries instead of a nano laminate consisting of stacked ZnO and Al_2O_3 layers, the principle of island growth at small numbers of deposition cycles (see Chapter 2.2.1) has been utilised. As demonstrated in [64], island growth enables embedded particles (can also be referred to as grains) of a conductive material within an oxide matrix. By

depositing only islands of the conductive and the dielectric material, a granular composite can be achieved. A conceptional sketch of the intended composite is presented in Figure 3.7. The inlet presents the composition of ZnO and Al_2O_3 grains as a homogeneous multiphase-ceramic layer which can be applied between two electrode layers. The humidity sensing mechanism of this ALD multiphase-ceramic is presented in Figure 3.8. In Figure 3.8 a., the state of a sensitive ALD composite in dry environment is demonstrated. The grain surfaces are saturated with adsorbed oxygen molecules from the surrounding atmosphere which trap free electrons of the conductive ZnO grains. As a result, depletion regions are formed at the ZnO grain surfaces.

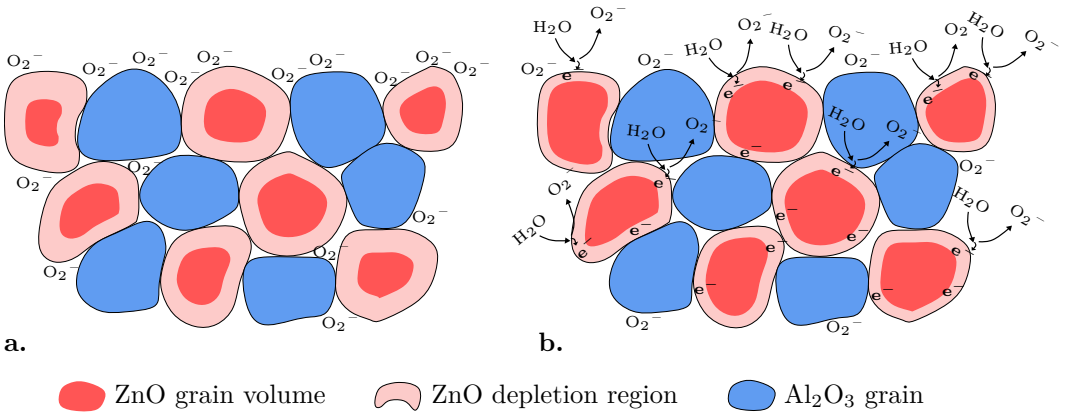

Figure 3.8: ALD composite with dielectric Al_2O_3 and semiconducting ZnO grains: a. composite with depleted ZnO grain boundaries due to adsorbed oxygen molecules on the grain surfaces; b. with increasing level of humidity, water molecules replace oxygen molecules and release electrons which are donated to the depleted region. Conductivity of single grains and total composite increase.

Due to the granularity of the aimed composite, water molecules can be adsorbed at the sensor layer surface and diffuse between the grains where they replace the O_2 molecules. Chemisorbed water molecules on the surfaces of n-type semiconducting ZnO-grains can donate electrons so that the amount of free electrons in the semiconductor grain increases. This phenomenon increases the conductivity of ZnO-grains and decreases the resistivity of the ALD composite (Figure 3.8 b.). Thus, the aimed composite reacts sensitively to changes in humidity.

Different deposition methods, for example drop-coating specific suspensions [88] or screen-printing pastes [89], allow the fabrication of ZnO nanoparticles or nanorods which feature an increased surface area and promote capillary condensation of water which supports the sensor sensitivity. In case of ALD grown ZnO, both granularity and increased surface area can be implemented. Additionally, the inherent conductivity of the ALD ZnO, which owns a relatively low specific resistivity of approximately 8 mΩcm, generates a low-impedance junction between the electrode layers. This is contrary to the application-oriented demands which require resistance values in the MΩ range in a dry surrounding. Thus, pure ALD grown ZnO layers are not appropriate as a sensitive layer for an impedance-type humidity sensor. Pure Al_2O_3 is amorphous and free of pores. Incapable of adsorbing water vapour, ALD grown Al_2O_3 is therefore an unsuitable humidity-sensitive material. However, the principle of island growth allows both materials to be combined into a granular composite. In this composite, sensitivity is dominated by the amount and the size of the semiconducting ZnO grains, which react sensitively to water vapour and other reducing gases. Deposition of Al_2O_3 is only used in order to generate dielectric buffer grains, so that sensitive ZnO grains are separated from each other and no conductive nanolaminate can be formed due to island coalescence. The Al_2O_3 content also reduces the conductivity of the composite. Thus, resistances in the MΩ range can be achieved in dry air and application-oriented demands can be fulfilled.

This approach allows the fabrication of a humidity-sensitive ALD composite at process temperatures $\leqslant 300\,^{\circ}\mathrm{C}$ which can be applied to three-dimensional substrates in a very conformal way. Synthesis and deposition processes are much simpler compared to multiphase-ceramics for use in humidity sensors. Additionally, the presented ALD composite is more temperature-stable than humidity-sensitive polymers and can be applied more evenly to complex topographies.
The sensitivity depends on the amount and surface area of the ZnO grains which react to adsorbed water molecules with band bending of the conduction band and thereby increased conductivity (see Figure 2.4 in Chapter 2.1.2). Therefore, the number of sensitive ZnO grains has to be maximised so that the interaction between adsorbed water molecules and ZnO grain boundaries is promoted. This can be achieved by producing fewer but larger grains with large surface areas or

by producing many but small grains with small numbers of ALD reaction cycles.

The maximum number of reaction cycles has to be determined in order to avoid formation of nanolaminates of Al_2O_3 or ZnO. The growth rate (expressed in GPC) of the composite has to be determined so that the thickness of the composite between two metal layers can be adjusted. Additionally, the topography of the composite has to be investigated. As discussed in Chapter 2.1.2 (Influence of Porosity), the porosity of the composite plays a significant role since it can support or suppress the adsorption of water molecules. Based on the number of reaction cycles for Al_2O_3 and ZnO islands and the number of super-cycles, the grain sizes of both materials and the ratio of the composite can be adjusted. Also electrical properties (especially resistivity) and final composite-thickness can be estimated. All of these parameters are taken into consideration during the process development of humidity-sensitive thin-film composites. Nevertheless, non-homogeneities can occur due to process deviations, such as temperature gradients on the substrate or inconsistent flow rates of reactants. This can lead to undefined ratios of Al_2O_3 and ZnO grains at different locations which means that also the sensitivity can vary on adjacent spots on the substrate.
Preliminary investigations, test depositions and characterisations were carried out for the creation of suitable ALD recipes. These experiments were necessary in order to investigate the island growth behaviour, the growth rate and the homogeneity of the aimed composite. Respective results are discussed in Chapter 3.3.4.

3.2.4 Hermetic Sealing

Biostability of materials used in active implants, which have direct contact to used surrounding tissue, is mandatory. For component-level encapsulated implants with a hermetic sealing of the implant components, biostability is given by the additional shaping silicone coating on top of the hermetic sealing. Due to the poor diffusion barrier properties of silicones, absorption of water molecules cannot be prevented. Thus, also the hermetic sealing material needs to feature suitable biostability so that corrosion of implant components can be avoided and surrounding tissue can be protected from resulting harmful substances.
Common passivation materials for CMOS components are e.g. silicon nitride (Si_3N_4) or silicon dioxide (SiO_2). Regarding [7, 8], these materials can show a solubility in water and may produce basic ammonia or acidic substances.

The encapsulation concept presented in this thesis includes a hermetic ALD thin-film which envelops the whole implant and the former applied encapsulation layers. For this purpose, Ta_2O_5 is chosen as a suitable material due to the proven diffusion-barrier and protection properties in phosphate-buffered saline (PBS) and 0.9 % NaCl-solution [18, 6, 17] or in 0.1 mol hydrochloic acid [90].

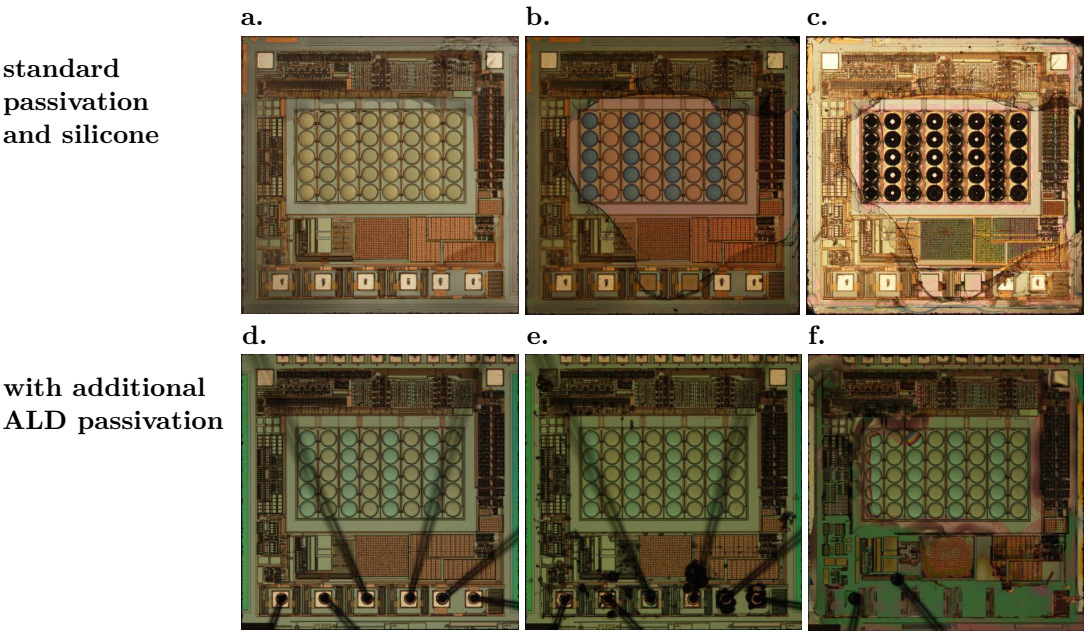

Figure 3.9: Photographs of pressure sensor chips with standard passivation in the top row and with an additional stack of ALD films (50 nm Al_2O_3 and 50 nm Ta_2O_5) in the lower row, all stored in an autoclave with PBS at 150 °C: (a. and d.) before the storage begins, (b. and e.) after one hour of storage and (c. and f.) after 15 or 36 hours of storage, respectively; adapted from [6].

Sealing properties and biostability of Ta_2O_5 have been proven in [6]. Additionally, accelerated ageing of a pressure sensor chip with standard passivation (750 nm thick SiO_2 and 500 nm thick Si_3N_4) has been compared to the accelerated ageing of a sensor chip with an additional stack of ALD Al_2O_3 and Ta_2O_5 (both 50 nm thick). The difference in sealing quality was tested by a storage test in an autoclave. Both sensors were put into PBS with an elevated temperature of 150 °C for up to 56 h and optically examined with different time intervals (see Figure 3.9). In order to protect some of the blank aluminum pads of the standard passivated sensor chip, a silicone coating with *Nusil Med-6015* was applied.

At the beginning of the accelerated ageing test, both sensor chips are free of defects (a. and d.). After only one hour in the autoclave, first signs of corrosion

can be seen on the two unprotected bonding pads (without silicone coating) and on the pressure sensitive membranes in the middle of the standard passivated sensor chip (b.). Corrosion signs also appear at the bonding pads of the sensor chip with an additional stack of ALD Al_2O_3 and Ta_2O_5 films (e.), since weak points in the encapsulation between the used gold bonding wires and the aluminum pads are expected. However, no other defects can be seen. After 15 h, the standard passivated sensor chip is almost completely destroyed (c.). Also the additionally passivated sensor chips shows major corrosion damage (f.). Nevertheless, (triggered by the corrosion at the bonding pads) the damage occurs after around 36 h and, with regard to the knowledge from [6], might be prevented if the aforementioned weak points are coated with, for example, the protecting silicone *Nusil Med-6015*.

The implemented encapsulation concept in this thesis consists mainly of a stack of ALD thin-films. Thus, a good adhesion and material compatibility is expected between single layers, whereby the use of ALD Al_2O_3 as an adhesive between the standard passivation and the Ta_2O_5 is not considered to be necessary. The deposition of Ta_2O_5 as a hermetic sealing layer can be achieved by the ALD process parameters presented in Table 3.4.

Table 3.4: Utilised process parameters of Ta_2O_5 deposition.

	Precursor A	Precursor B	Pulsing-Purging times	Process temperature
Ta_2O_5	$Ta(EtO)_5$	H_2O	1.8 s, 8.0 s - 0.1 s, 8.0 s	270 °C

By fulfilling all technological and application-oriented requirements, such as highly isotropic deposition at temperatures below 350 °C and hermeticity as well as biostability, ALD Ta_2O_5 is chosen to be the hermetic sealing material for the final layer of the encapsulation stack.

3.3 Process Developments

The development of the presented process flow required tests and investigations regarding single process steps. In this chapter, developments with regard to three-dimensional deposition of parylene F and and die-level patterning by laser

ablation of are discussed. Additionally, ILC with ALD metals are evaluated with the help of two different test structures. Finally, preliminary experiments on ALD composites are accomplished in order to investigate growth rates of various composites, limiting ALD cycle number for island growth of ZnO and Al_2O_3 and the homogeneity of fabricated composites.

3.3.1 3D-Deposition and Adhesion of Parylene F

For the implementation of the presented encapsulation concept, good conformality and adhesion of the individual layers are needed. Especially the properties of the first layer are of great importance since this layer encapsulates the complex surface of the implant. Susceptible spots for mechanical defects, for example sawn die edges and side walls, should be coated with a high step coverage. The first-layer material should creep into every unevenness and gap during the deposition process, which is performed under vacuum, so that air inclusions can be avoided by which the risk of water vapour condensation on the substrate surface is minimised. Thus, the probability for the occurrence of delaminations or corrosion is minimised as well [6]. Without condensation or migration of ions, corrosion effects can be prevented on the voltage-carrying components and contact pads [16, 6].

Highly isotropic deposition of a chemically inert and high-ohmic parylene F fulfils these requirements. Due to the Gorham process, pinhole-free and three-dimensional coating of complex implant surfaces is possible. In Figure 3.10, SEM cross-sections of a silicon die for test purposes with a three-dimensional parylene F coating are presented. Since the used CVD process does not show perfect conformality, the parylene thickness varies at different positions on the die. Figure 3.10 a. reveals the surface of the coated die where the parylene layer shows a thickness of 3.5 µm, whereas b. shows a coated die-edge and sawn side wall with a thickness of 2.5 µm and 3.7 µm, respectively. Colour distortions within the parylene F layer indicate an uneven breaking edge of the comparatively soft polymer and are to be interpreted as fracture artefacts.

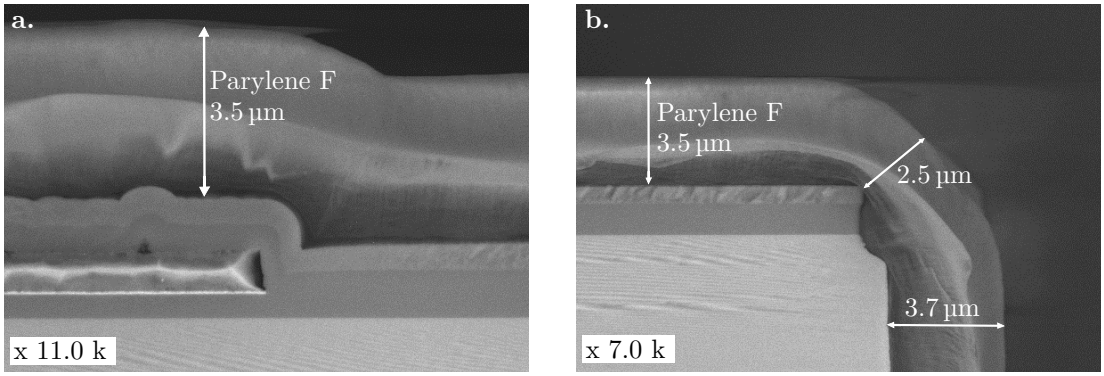

Figure 3.10: SEM cross-sections of a three-dimensionally coated silicon die with parylene F: a. surface of the die with aluminum metallisation and isolating films (nitrides), coated with a 3.5 µm parylene layer; b. conformally coated die edge and sawn side wall with a parylene layer thickness of 2.47 µm and 3.75 µm, respectively.

A strong adhesion to the substrate surface is also required. To verify the sufficient adhesion of parylene to the substrate surface, a tape-test was implemented. The 3.5 µm thick parylene F layer enveloping the test die with an isolating nitride on the surface, was scratched intentionally with the tip of a needle. The cross-shaped weakness in the parylene layer was tested by removing the test strip in different directions in order to examine the prepared area for delaminations. No delaminations or other undesired effects were observed at three tested spots.

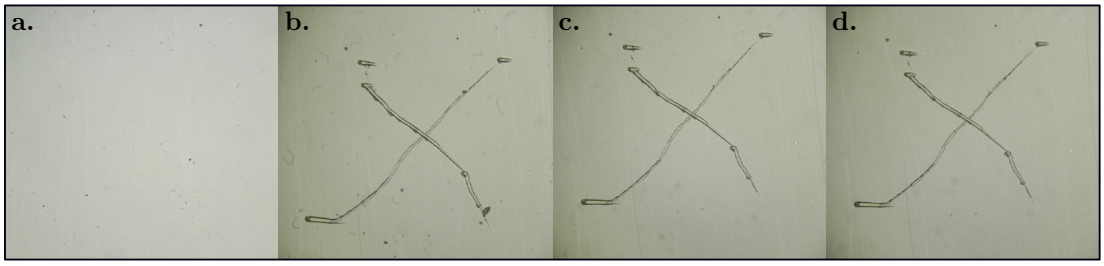

Figure 3.11: Proof of adhesion by successful tape-test: a. parylene coated substrate, b. manually prepared spot with a cross (by the use of a test-needle), c. prepared mark after first strip (parallel in one and vertical in the other direction), d. prepared mark after second strip (45° in both directions).

Representative results are presented in Figure 3.11. Figure 3.11 a. and b. show one examined spot before and after preparing a cross-shaped scratch with a needle. Figure 3.11 c. presents the result after stripping the tape along one line and vertically to the other line, whereas d. presents the result after removing a

second piece of tape with an angle of 45° in both directions. Presented results indicate a sufficient adhesion of the parylene F on the silicon die.

3.3.2 Patterning Parylene F and ALD Layers by Laser Ablation

Patterning of parylene F and ALD layers is performed by using short laser pulses with pulse widths of a few nanoseconds. The ablation of parylene F, which is the first and also the thickest layer in this encapsulation stack, is achieved by the application of the ultraviolet laser with a wavelength of $\lambda = 355\,\text{nm}$.

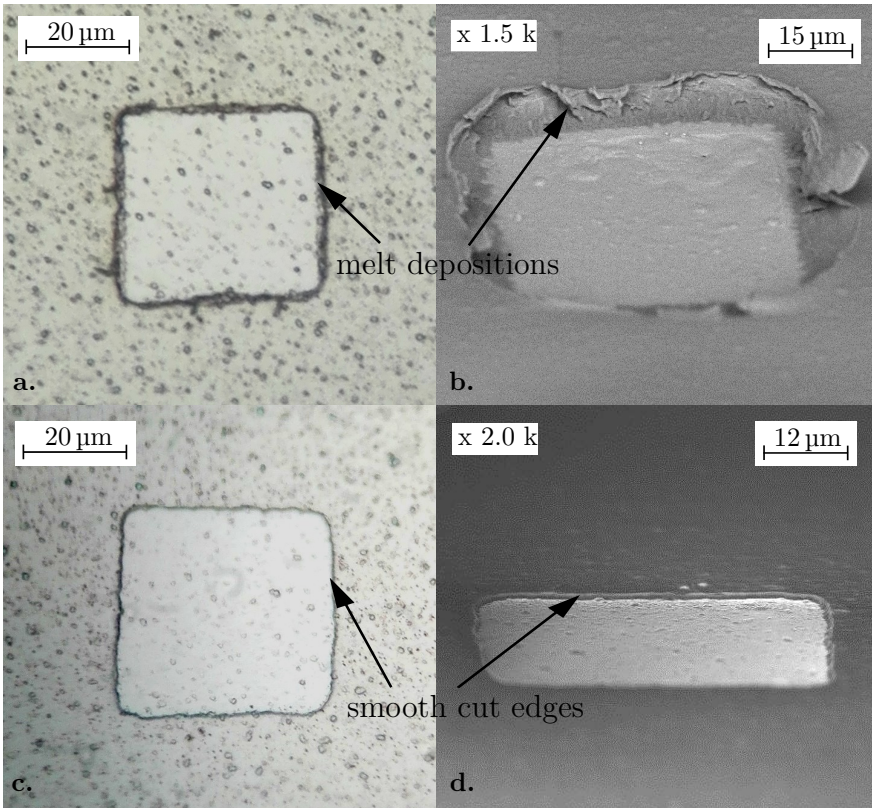

Figure 3.12: Microscope and SEM images of parylene films after laser ablation with a cut size of 40 µm x 40 µm, before (a. and b.) and after an additional O_2-flash treatment with approximately 40 for 7 min (c. and d.).

Due to the thickness of up to 3.5 µm, the amount of material to be removed is much bigger for the structuring of parylene than for the structuring of ALD layers with layer thicknesses in the nm-range. Therefore, only during the ablation process of parylene, residuals and debris are formed at the cut edges. These

residuals and debris obstruct further deposition with ALD thin-films and need to be minimised. This can be achieved by the application of an additional O_2-flash which cleans the opened metal surface and smooths the parylene edges. By this process the parylene coating is thinned and slightly roughened on the surface which even facilitates the adhesion of further ALD layers on the polymer coating. Microscope and SEM images of a parylene film after laser ablation, before and after the application of an additional O_2-flash, are presented in Figure 3.12. The chosen cut size was 40 µm x 40 µm. The improved smoothness at the parylene edges due to removal of polymer residuals after 7 min of O_2-flash treatment can be observed. The parylene F film thickness was reduced to approximately 0.8 µm. Further ablation tests were performed with various ALD materials which are applicable in the encapsulation concept. An overview of laser process parameters is presented in Table 3.5. Generally, metals are patterned by a green laser. Polymers and dielectrics are patterned by UV laser. The green laser was applied through a regular objective with a magnification of 50 x, while the UV laser was applied through the specific objective with a magnification of 100 x.

Table 3.5: Verified parameters for laser ablation of various materials with specific thickness (stated energy levels are device-specific).

	Material	Thickness in nm	Trigger mode	Energy level	Cut size in µm x µm	Objective (magnification)
Green laser	Ru	25	Burst 12x	High, 12	40 x 40	50 x
UV laser	Parylene F	≈ 2500	Burst 3x	High, 30	40 x 40	100 x
	$ZnO+Al_2O_3$	20	Burst 6x	High, 13	40 x 40	100 x
	$ZnO+Al_2O_3$	70	single shot	High, 38	60 x 60	100 x

3.3.3 Evaluation of ILC with ALD Metals

In this chapter, ILCs with an ALD metal are evaluated at vias which are fabricated with two different process flows. The first process flow includes photo-

lithographic patterning and an additional etching step, whereas the second process utilises laser ablation for the opening of vias. Two test structures with variously fabricated vias were used for the evaluation of resulting ILC. The test structures are discussed in the following. In both cases TiW was used for the first metal layer and ALD-Ru was applied as second metal layer for each test structure.

First, the actual resistivity ρ_x of used metals was determined at room temperature with the help of meander shaped structures with a length of approximately 6.8 mm and a width of 6 µm. Therefore, the Equation 3.1 was used.

$$\rho_x = R \cdot \frac{h \cdot w}{l} \tag{3.1}$$

Here, h and w are the height and the width of the metal, respectively, while l stands for the length of the test structure. For the determination of the measurand R, IV measurements were performed with an *Agilent 4155C* Semiconductor Parameter Analyser within a range from 0 V to 1 V at room temperature. Measured resistances of TiW and Ru meander structures, aimed and actual thickness and theoretic and calculated values for ρ are summarised in Table 3.6. The aimed thickness of the metals was determined during the manufacturing procedure of the test structures. The actual thickness is determined by investigating the cross-section of the structures with the help of SEM. Calculated resistivities are in the expected range, but slightly lower than assumed. These deviations could be caused by temperature differences during the measurements or by inaccurate determinations of the layer thickness.

Along with the actual specific resistances of used metals, via resistances can be calculated as well. Since reasonable resistances for individual metal layers were detected in the lower half of the wafer with an adequate distance to the wafer edge, this position was utilised for further measurements and evaluations of via resistances. Two different structures were tested.

The first test structure (presented in Figure 3.13) is a via-chain with a length of approximately 2.8 mm and a width of 6 µm. Metal 1 and metal 2 wires, separated by 850 nm of undoped silicon glass (USG), are connected by 154 vias in

Table 3.6: Resistances of TiW and Ru meander structures with assumed (theoretical) and calculated (actual) specific resistances.

Metal	Aimed thickness	Assumed ρ_x	Measured resistance	Actual thickness	Calculated ρ_x
TiW	100 nm	80 µΩcm [91]	1430 Ω	90 nm	11.4 µΩcm
Ru	20 nm	85 µΩcm [92]	1694 Ω	25 nm	37 µΩcm

total. The isolating USG was patterned by photo-lithography and opened by a subsequent etching step at the respective via positions before metal 2 was deposited. The resistance of the via-chain was determined by IV measurements. Figure 3.13 a. shows a photograph of the meander-shaped via-chain. Magnified vias are presented in the inlet. In Figure 3.13 b., a tilted view of the vias of the test structure is presented using SEM, while Figure 3.13 c. reveals the cross-section of one single via. Here, individual metal layers and their electrical contact in the via opening are shown.

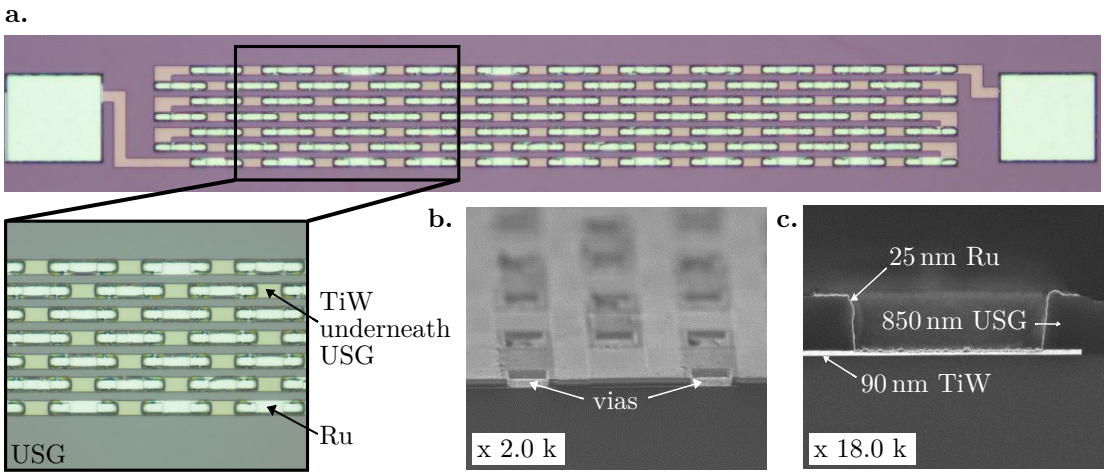

Figure 3.13: Via-Chain (vias fabricated by photo-lithographic patterning, etching and resist removal) for the investigation of contact resistances in the via openings: a. photograph of used test structure, inlet shows magnified vias connecting underlying TiW (metal 1) with upper Ru (metal 2) through the isolating USG; b. SEM image with tilted view on the via-chain; c. SEM image of the cross-section of a single contact between metal 1 and metal 2.

According to the applied voltage, a current is generated and measured which allows the calculation of the resistance with respect to Ohm's law. By subtracting the inherent wire resistances of both metal layers, the resistance of all contacts in the via openings can be determined. This can be used to estimate the resistance

of one single contact between metal 1 and metal 2. In a photo-lithographically patterned via with a length of 8 µm and a width of 4 µm, the calculated contact resistance was $\approx 11.7\,\Omega$. This value is sufficiently low and can be used as a reference for the second test structure.

The second test structure (presented in Figure 3.14) was used to estimate the resistance of a single contact between metal 1 and metal 2 in a via opening which was fabricated by laser ablation. Electrical contacting of conductive layers with other metallisation layers through openings by laser ablation has already been successfully tested [93]. For further evaluation of such electrical contacts, with regard to contacts through photo-lithographically patterned via-openings, a second test structure was used.

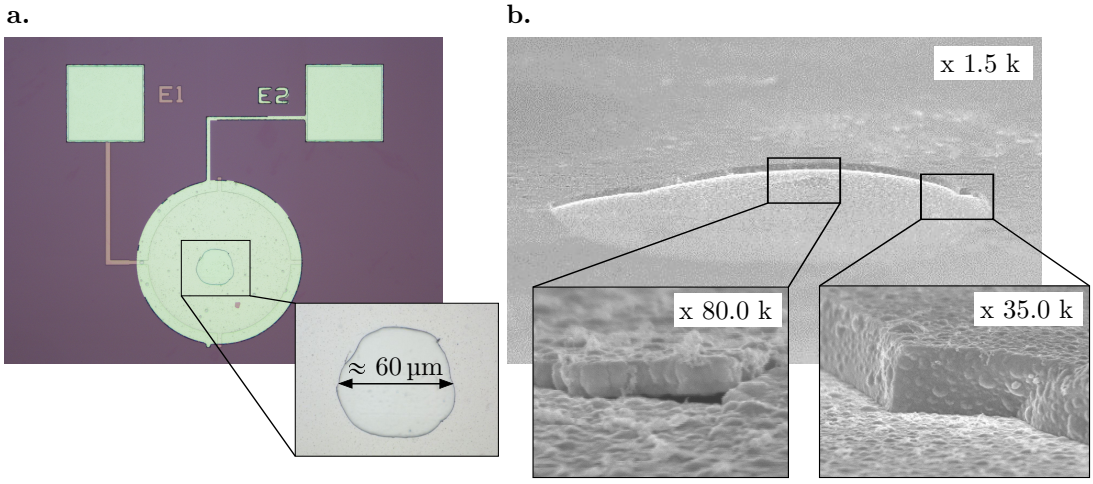

Figure 3.14: Test structure 2 is a plate capacitor with one via (fabricated by laser ablation) for the investigation of the via resistance: a. photograph of used structure, inlet shows the magnified opening by laser ablation after deposition of Ru-metallisation; b. oblique view of the corresponding via using SEM, left inlet shows a crack in the Ru (presumably due to an already existing crack in the lower TiW electrode), right inlet presents the smooth coating of the cut edges.

This circular shaped structure with TiW-metallisation as the bottom electrode (electrode diameter was 220 µm) and a 850 nm USG dielectric was equipped with an opening in the USG layer by laser ablation. A single-shot UV laser with a wavelength of 355 nm (with increased energy level at level 31) was used for the opening of the dielectric. Thus, no photo-lithography, no resist removal and no wet-cleaning processes were required. Further processing, such as the applica-

tion of an O_2-flash for the removal of parylene-debris at the cut edges, was not necessary since no generation of melt depositions was observed. This opening, with a diameter of about 60 µm, allowed an ILC of the bottom electrode with a subsequently-applied Ru-metallisation which served as the top electrode. Figure 3.14 a. shows a microscope photograph of the test structure with the via opening in the middle of both circular shaped electrodes (magnified view in the inlet). Figure 3.14 b. presents a tilted view on the structure and the position with laser ablated USG, smoothly coated with ALD Ru.
IV measurements under same conditions as for the first test structure were performed in order to determine the resistance of the via fabricated by laser ablation. Again, inherent resistances of the electrodes were calculated and subtracted from the measured resistance of the test structure. Thus, the resistance of the single via could be estimated. Despite the large via diameter and the resulting contact area, the determined via resistance was $\approx 250\,\Omega$. This value is unexpectedly high but not unreasonable. As shown in the left inlet in Figure 3.14 b., laser ablation may lead to small damages in form of cracks in the bottom electrode due to heat generation during the short laser pulse laser ablation process. Also remaining USG residuals may increase the resistance of the ILC.

Measured currents of meander shaped structures with both metals and via resistances from both test structures are presented on the left y-axis of the graph in Figure 3.15. Correspondingly calculated resistances are presented on the right y-axis. Test voltage (from 0 V to 1 V) is applied on the x-axis. Converted to a contact area of $1\,mm^2$, a via fabricated by means of photo-lithography and subsequent etching would feature a resistance of approximately $0.37\,m\Omega$, while a via fabricated by laser ablation would have a resistance of approximately $0.71\,\Omega$. The second resistance is higher by a factor of almost 2000. Considering the later application of such an ILC with ALD metals through a via fabricated by laser ablation, these ILC-resistances are still negligible. Metal layers, which shall be electrically connected to the implant circuitry with such ILCs, are supposed to enclose a humidity-sensitive layer with a much higher inherent resistivity (in the range of several MΩ). Thus, ILCs with ALD metals through laser ablation-fabricated vias are considered as suitable for the implementation of the encapsulation concept which is presented in this work.

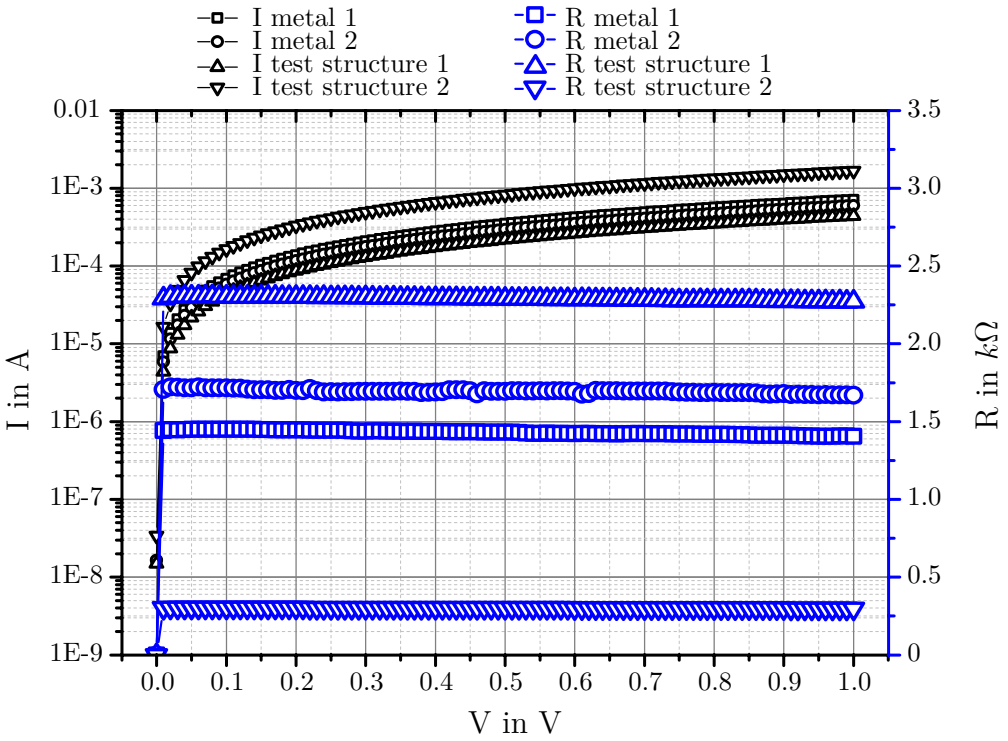

Figure 3.15: Results of IV-measurements with meander shaped structures (metal 1 and 2) and both test structure (first: via-chain, vias fabricated with photo-lithographic patterning and subsequent etching step; second: test structure with a single via, fabricated by laser ablation of the dielectric USG between both metal layers); the left y-axis presents measured currents, while the right y-axis shows calculated resistances with respect to applied voltages (0 V to 1 V).

3.3.4 Studies on ALD Composite Growth

After the concept for the development of a humidity-sensitive ALD composite has been explained in Chapter 3.2.3, preliminary experiments for the creation of suitable ALD recipes are discussed in the present chapter. For the successful fabrication of a homogeneous and humidity-sensitive mixture of ZnO and Al_2O_3 grains, island growth behaviour of both materials is investigated first.

Due to steric hindrance from precursor molecules and localised distribution of active sites on the substrate surface, island growth can be achieved if the growth of an ALD material is substrate-inhibited. Islands grow continuously with each additional deposition cycle. If only islands are aimed at, the number of deposition cycles n has to be small enough so that touching neighbouring islands and forming a planar layer are prevented. Al_2O_3 is a metal oxide which demonstrates

substrate-inhibited growth on SiO_2 and ZnO substrates. In literature, the limiting number of deposition cycles for island growth of Al_2O_3 on a SiO_2 substrate is 16. [60]
The ALD process parameters, precursors and pulsing and purging times of used oxides are listed in Table 3.7.

Table 3.7: Utilised process parameters of Al_2O_3 and ZnO depositions.

Oxides	Precursor A	Precursor B	Pulsing/Purging times	ALD-window
Al_2O_3	$AlMe_3$	H_2O	$AlMe_3$: 0.1 s, 6 s H_2O: 0.1 s, 10 s	220 °C to 380 °C
ZnO	DeZn	H_2O	DeZn: 0.1 s, 8 s H_2O: 0.2 s, 8 s	200 °C to 300 °C

Process temperature was set to 270 °C and process pressure was set to approximately 6 for each test deposition. Under these process conditions, individual GPC values were estimated as $\approx 0.15 \frac{\text{nm}}{\text{cycle}}$ for pure Al_2O_3 and $\approx 0.17 \frac{\text{nm}}{\text{cycle}}$ for pure ZnO.

GPC of ALD Composites

The GPC rate is, amongst other parameters, a function of the surface where the reaction between the precursors occur. Considering the growth types (presented in Figure 2.8), growth rates may change during a deposition process. Especially at the beginning of a process, the effect of the substrate is dominant. For the substrate-inhibited growth type, islands are formed at small numbers of deposition cycles. During this phase, GPC values are smaller than in the phase of constant growth which only occurs if the substrate is already covered by the material to be deposited (after island coalescence has occurred). Hence, GPC values for composites with nanolaminates are higher than GPC values for composites with homogeneously distributed islands.

GPC rates may also differ at different ALD equipments due to varying pulsing and purging times or different process pressures. Therefore, preliminary experiments with composite recipes were accomplished on blank silicon substrates in order to determine the limiting number of deposition cycles n for ZnO and Al_2O_3 islands. Regarding [60], in which island coalescence starts at $n = 16$, maximum

n was chosen $\leqslant 15$ in this work. Since a process temperature of 270 °C works for both oxides, all processes were performed at this temperature. An overview of composite recipes for three experimental depositions are presented in Table 3.8. Here, x represents n for Al_2O_3, y represents n for ZnO and super-cycle is the number of repetitions of alternately applied Al_2O_3 and ZnO depositions $(x + y)$. On the basis of super-cycles, a common number of total deposition cycles was targeted for each experimental deposition. In order to verify this assumption, a common number of total deposition cycles of about 560 was chosen for each experimental deposition.

Table 3.8: Deposition cycle numbers and super-cycle numbers of experimental depositions which are used for determining the limiting n for island growth.

Sample	x	y	Super-cycles	Deposition cycles in total
1	15	12	21	567
2	8	8	35	560
3	4	4	70	560

The layer thickness of these depositions actually achieved (in the centre of the respective wafer) is presented in Figure 3.16. The cross-section of sample 1 reveals a composite layer thickness of approximately 166 nm (a.), whereas sample 2 shows a thickness of approximately 100 nm (b.). The SEM cross-section of sample 3 (presented in Figure 3.16 c.) presents a layer thickness of approximately 45 nm. Even though the total amount of deposition cycles is comparably high for each sample, layer thickness between sample 1 and sample 2 varies by more than 50 %. The higher growth rate of sample 1 indicates the fabrication of stacked thin-films of ZnO and Al_2O_3, while the much smaller growth rate of sample 2 indicates growth of ZnO and Al_2O_3 islands. The difference between sample 2 and 3 are the halved numbers of deposition cycles for each oxide (x and y are chosen 4 instead of 8). Thus, islands with also halved sizes are expected in sample 3, which would result in a halved composite layer thickness, despite the same amount of deposition cycles in total. With a layer thickness of 45 nm, as shown in Figure 3.16 c., sample 3 fulfils the expectations.

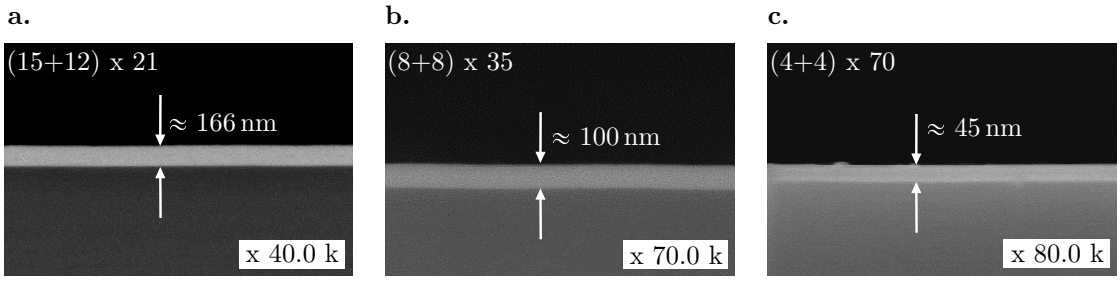

Figure 3.16: SEM cross-sections of various ALD composites and respective thickness: a. sample 1 with a layer thickness of approximately 166 nm; b. sample 2 with a layer thickness of approximately 100 nm; c. sample 3 with a layer thickness of approximately 45 nm.

Estimated GPC rates are ≈ 13.83 nm per super-cycle for sample 1, ≈ 2.86 nm per super-cycle for sample 2 and ≈ 0.64 nm per super-cycle for sample 3.
For further investigation of the limiting number of deposition cycles (x and y) for island growth of used oxides, time of flight - secondary ion mass spectrometry (TOF-SIMS) was performed with sample 1 and 2. Achieved results are presented in the following.

Limiting ALD Cycle Number for Island Growth

The distribution of different oxide clusters within the composites of sample 1 and sample 2 was investigated by TOF-SIMS (*TOF.SIMS* $5-100$ from *ION-TOF GmbH*). By using TOF-SIMS, the composition of a solid thin-film can be investigated by sputtering the surface of the tested film and collecting ejected secondary ions. A mass spectrometer measures these secondary ions so that the composition of the thin-film can be analysed. This investigation technique allows depth profiling with resolutions of < 1 nm per sputter step.
An area of 100 µm x 100 µm was monitored and an average of intensity was calculated for detected fragments. Intensity trends with respect to sputter depth revealed information about the composition of Al_2O_3 and ZnO elements in the deposited ALD composites.

Since experimental depositions were accomplished on untreated silicon wafers, the ion intensity of Si was also evaluated. The investigated samples were taken from the centres of the respective wafer. Intensity signals for Al_2O_3, ZnO and Si ions are plotted with respect to the sputter depth. These results are presented in Figure 3.17 a. for the first and in 3.18 a. for the second test composite.

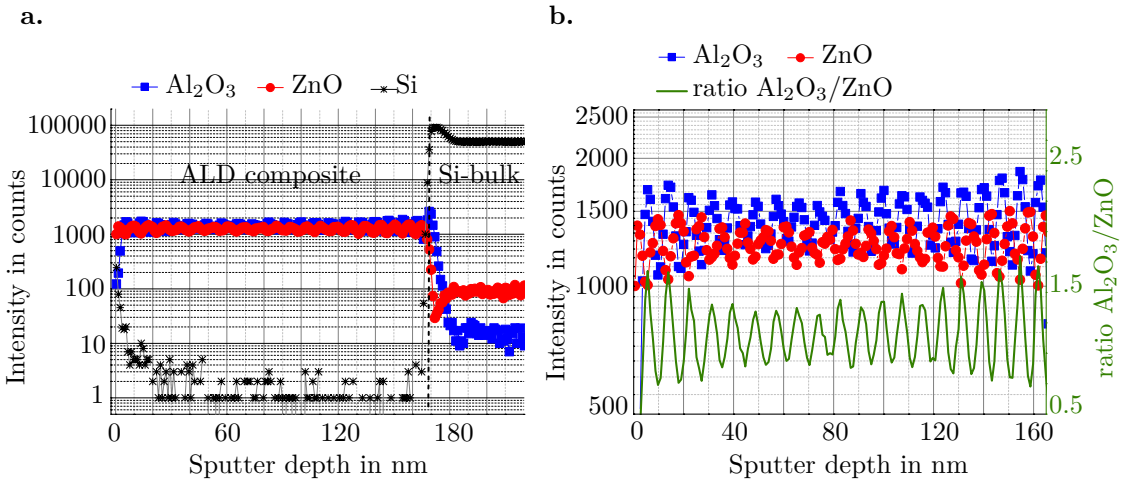

Figure 3.17: TOF-SIMS of the composite with 15 cycles for Al_2O_3 and 12 cycles for ZnO: a. representing intensity of measured ions over the sputter depth; b. representing also the calculated ratio of Al_2O_3 and ZnO ions, after [94].

As expected, ion intensities of the composite materials significantly decrease at the interface to the bulk material, where the intensity of detected bulk Si ions increases at the same sputter depth. In Figures 3.17 b. and 3.18 b., the calculated ratios of Al_2O_3 to ZnO ion intensities are drawn as well.
As shown in Figure 3.17 a., the interface between ALD composite and bulk material of sample 1 could be detected at about 166 nm sputter depth. Detected Al_2O_3 and ZnO ion intensities are obviously alternating during the whole sputter depth until the bulk is reached. Ion intensities and resulting ratio (sinusoidal shape) within the range of composite thickness are presented in Figure 3.17 b.. This result indicates a nanolaminate or at least stacked layers with significant predominant content of single materials. Considering the period lengths of phase shifted intensity curves, Al_2O_3 layers of up to 5 nm thickness and ZnO layers of up to 3 nm thickness can be extracted.

The reduction of deposition cycles from 12 and 10 to 8 for each oxide results in a totally different TOF-SIMS outcome. As presented in Figure 3.18 a., linear curves without any gradients are presented for Al_2O_3- and ZnO-ion intensities. Comparable to Figure 3.17, the ion intensities of both oxides significantly decrease at the interface to the bulk material, which is at $\approx$ 100 nm. Figure 3.18 b. shows the enlarged depth within the range of ALD composite thickness. Intensities of Al_2O_3 and ZnO are constant which results in a constant ratio, as well.

This indicates that the amounts of Al_2O_3 and ZnO elements are constant at every sputter step through the whole oxide composite.

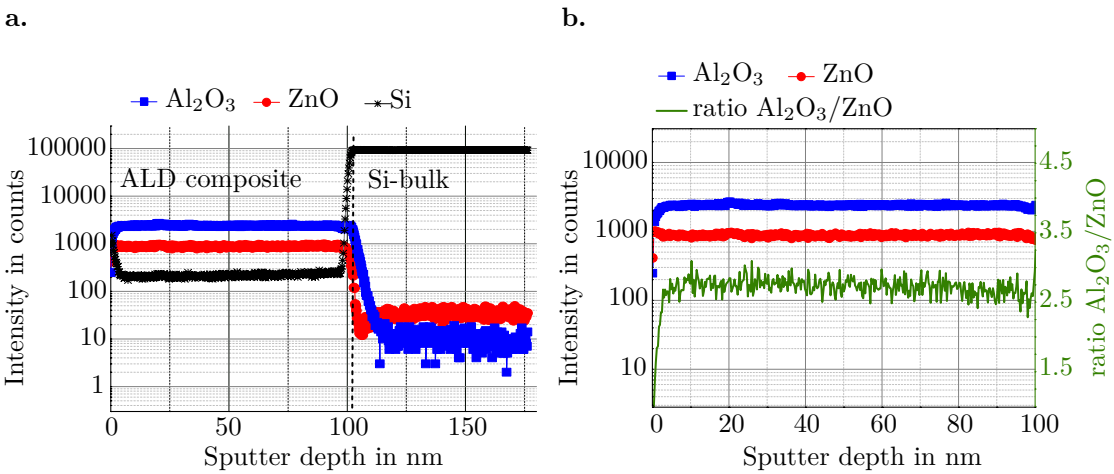

Figure 3.18: TOF-SIMS of the composite with 8 cycles each for Al_2O_3 and ZnO: a. representing intensity of measured ions over the sputter depth; b. representing also the calculated ratio of Al_2O_3 ions and ZnO ions, after [94].

The results of the TOF-SIMS support the assumption that the experimental deposition of sample 1 obviously resulted in a stack of nm-thin Al_2O_3 and ZnO layers and that island growth of Al_2O_3 and ZnO can be achieved with a number of deposition cycles $n \leqslant 8$. Regarding GPC rates of sample 2 and sample 3, it is also assumed that halved number of deposition cycles lead to halved sizes of islands. These limits will be taken into account for the fabrication of a humidity-sensitive ALD composite, consisting of Al_2O_3 and ZnO islands, in the following referred to as grains.

Homogeneity of ALD Composites

ALD processes show highly conformal and homogeneous depositions. The self-limited saturation of the precursor molecules on the substrate surface allow for the controlled deposition of monolayers so that a controlled layer thickness with very small deviations can be achieved.

Outgoing from the single-wafer reactor with seven vertical gas flow lines (line 1 to 6 for each of the six precursors and line 7 from the top with a constant N_2 flow with a flow rate of 50 sccm for better gas distribution on the wafer), flow rates at active and passive lines are set in such a way that the distribution of ZnO and

Al_2O_3 grains is even so that maximum deposition homogeneity is achieved. Considering the material to be deposited, at least two of the six precursor lines are active whereas the others are passive. Active lines pulse the required precursors into the chamber with corresponding pulsing time and flow rate. Passive lines purge the process chamber with N_2 continuously, so that precursor molecules are carefully distributed on the whole substrate. Generally, flow rates of active lines are higher than flow rates of passive lines. According to the circular distribution of the nozzles in the process chamber, this setting allows for a homogeneous coating of a wafer. Figure 3.19 presents the arrangement of the lines with corresponding precursors in the used ALD process chamber.

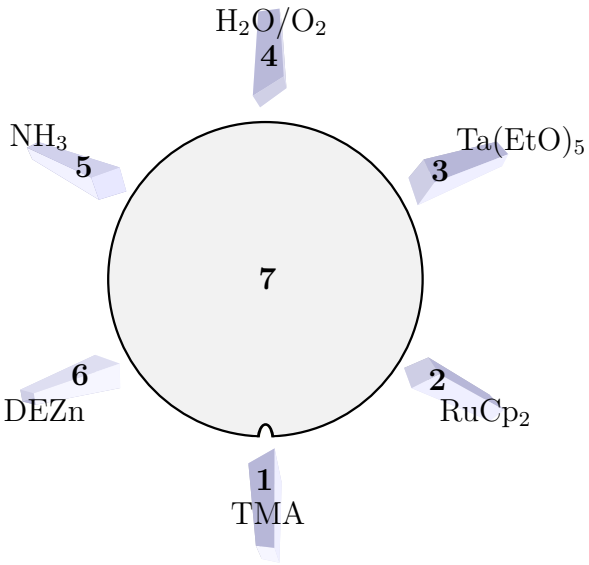

Figure 3.19: Arrangement of the lines in the process chamber of the used single-wafer ALD equipment with vertical gas flow. Line 1 to 6 are assigned to one of the six precursors, while line 7 serves with a constant N_2 flow with a flow rate of 50 sccm for better gas distribution on the wafer.

For materials such as ZnO or Al_2O_3, the homogeneous deposition of the films is well established by verified settings of the flow rates in each line. As an example, the deposition of a ZnO layer with 350 deposition cycles at 270 °C is discussed. With alternately applied DEZn and H_2O, a conductive ZnO layer could be achieved on a wafer with an electrically isolating USG coating.

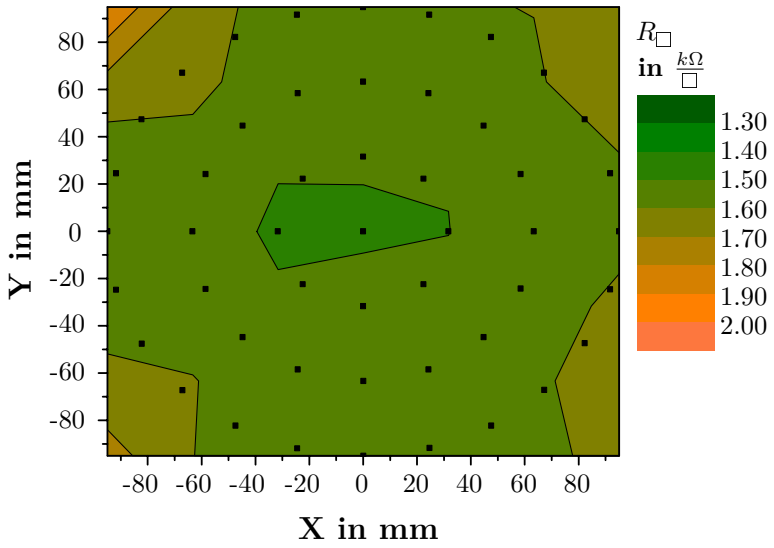

Figure 3.20: Contour plot with sheet resistances on 49 spots on a wafer with a 54 nm thick conductive ALD ZnO layer: the mean sheet resistance is 1.55 $\frac{\text{k}\Omega}{\square}$, while the 1 σ error is 2.4 %.

The layer thickness of 54 nm was optically measured by the ellipsometer *UV-1280 SE*, a thin film measurement system from *KLA-Tencor*. Sheet resistances of single spots on the wafer were measured by a *ResMap* four point probe from *CDE*. For very homogeneous ZnO layers, sheet resistances ($R_\square$ in $\frac{\Omega}{\square}$) are comparable and show small deviations only. In Figure 3.20, the contour plot of the tested ZnO film is presented. Determined from 49 measurement points all over the substrate, the mean value of $R_\square$ was 1.55 $\frac{\text{k}\Omega}{\square}$, while the 1 σ error was 2.4 %. The homogeneity in the distribution of two elements within the ALD composites is tested in the same way. By mixing conductive ZnO grains with isolating Al_2O_3 grains, a higher sheet resistance (compared to the pure ZnO film) with similarly small 1 σ error would be expected all over the substrate surface. Since composites with ZnO to Al_2O_3 ratios around 1:1 delivered sheet resistances outside the measuring range of the used four point probe, which has an upper measuring range limit of $\approx 25\ \frac{\text{M}\Omega}{\square}$, a higher ratio of 4:1 had to be chosen. Test depositions on USG coated wafers were performed with $n = 8$ for ZnO and $n = 2$ for Al_2O_3. The number of super-cycles was chosen to be 35, while the process temperature was 270 °C. Detailed parameters of the four tested depositions and summarised results of the four point measurements with 49 measuring points for each wafer are presented in Table 3.9.

Table 3.9: Test depositions for investigation of the composite homogeneity: Measuring the $R_{\square}$ of ZnO+Al_2O_3 mixtures with slightly varying process parameters (especially flow rates at precursor lines or pulsing times of the TMA precursor) can reveal information about the homogeneous distribution of conductive ZnO and isolating Al_2O_3 grains; all depositions are performed at 270 °C.

	Number of Test Deposition			
Parameters	1	2	3	4
n for ZnO islands	8			
Pulsing/Purging times for ZnO	0.1 s, 8 s / 0.2 s, 8 s			
n for Al_2O_3 islands	2			
Pulsing/Purging times for Al_2O_3	0.1 s, 6 s / 0.1 s, 10 s			0.2 s, 7 s / 0.1 s, 10 s
Number of super-cycles	35			
Line 1 flow rate in sccm	100	80	100	100
Line 2 flow rate in sccm	50	80	100	50
Line 3 flow rate in sccm	50	80	50	50
Line 4 flow rate in sccm	100	80	50	100
Line 5 flow rate in sccm	50	80	50	50
Line 6 flow rate in sccm	100	80	100	100
Minimum $R_{\square}$ in Ω/sq	1.42 k	1.3 k	1.79 k	3.57 k
Maximum $R_{\square}$ in Ω/sq	20.2 M	23.35 M	24.55 M	23.4 M
Mean $R_{\square}$ in Ω/sq	6.84 k	7.33 k	9.76 k	11.24 M
1 σ error in %	65.94	77.6	60.7	43.3

In the test depositions 1 to 3, flow rates of active and passive lines were changed in order to improve the distribution of precursor molecules on the substrate surface. The active lines of the presented ALD composite are DEZn for the generation of ZnO grains and TMA for the generation of Al_2O_3 grains. Both oxides require H_2O as the second precursor, which is why this line was active during the whole four test depositions.

Starting with 100 sccm at the active lines and only 50 sccm at the 3 passive lines, the mean sheet resistance for the first test deposition resulted in 6.84 $\frac{\text{k}\Omega}{\square}$

with a deviation of 65.94 %. As presented in the contour plot in Figure 3.21 a., a less-conductive channel is formed in the lower half of the wafer.
In test deposition 2, flow rates of each line were regulated to 80 sccm. This resulted in an even greater deviation of 77.6 % and a more pronounced channel with higher sheet resistances (see Figure 3.21 b.) in the lower half, which increased the mean sheet resistance to 7.33 $\frac{k\Omega}{\square}$.

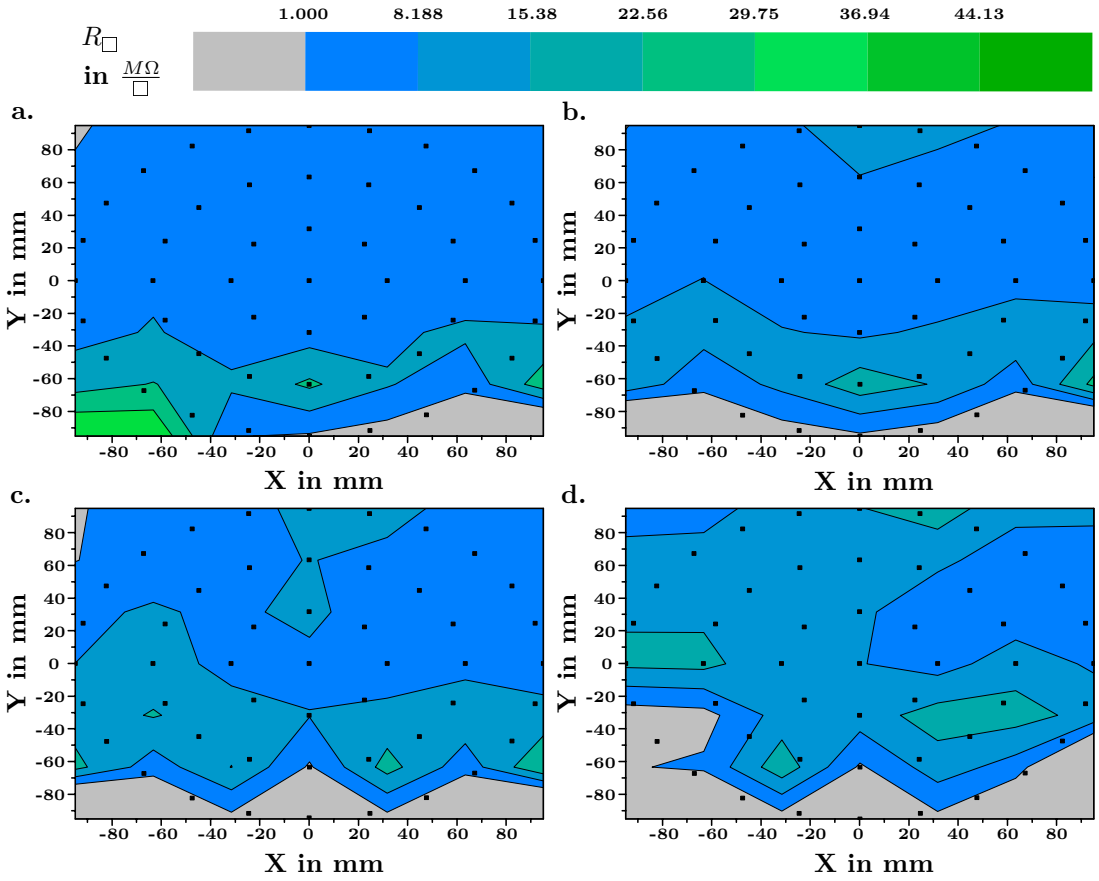

Figure 3.21: Contour plots with sheet resistances, measured at 49 points all over the wafers with test depositions 1 to 4 in the plots a. to d., respectively.

Including the results from the first test deposition, flow rates were changed again in the third test deposition. The more conductive upper half of the wafers of test deposition 1 and 2 seems to contain more conductive ZnO grains than isolating Al_2O_3 grains. In order to increase the amount of Al_2O_3 grains in this area, flow rates of lines 1, 2 and 6 were increased to 100 sccm, while the flow rates of lines 3, 4 and 5 were set to 50 sccm. The intention was the support of TMA distribution so that more Al_2O_3 grains could be generated on the upper half of

the wafer. Since TMA streams in from line 1 (see Figure 3.19), the flow rate of this and the neighbouring lines were increased, while the flow rates of the other lines were decreased. This intervention increased the size of the less-conductive channel in the contour plot (see Figure 3.21 c.) and the mean sheet resistance to 9.76 $\frac{\text{k}\Omega}{\square}$.
In test deposition 4, the same flow rates as in 1 were chosen but the pulsing and purging times for the TMA during the deposition of Al_2O_3 grains were increased from 0.1 sec to 0.2 sec and from 6 sec to 7 sec, respectively. This resulted in a mean sheet resistance of 11.24 $\frac{\text{M}\Omega}{\square}$ with a deviation of 43.3 %. The corresponding contour plot, as presented in Figure 3.21 d., also reveals that the distribution of conductive ZnO grains and isolating Al_2O_3 grains is more homogeneous than in previously tested composites.

Along with deviations of around 60 % up to 77 %, the homogeneity in the distribution of ZnO and Al_2O_3 grains is obviously very poor for test deposition 1, 2 and 3. By increasing the TMA pulsing and purging times in test deposition 4, the deviation could be decreased to 43 %, which is why pre-settings of test deposition 4, such as flow rates and pulsing or purging times, are used for further fabrication of humidity-sensitive sensor structures.

A reason for bad homogeneity of composites might be the hardware of the ALD equipment used. As shown in Figure 3.19, the lines with corresponding precursors are arranged circularly within the process chamber. This enables the supply of the precursor molecules at different positions on the wafer. By setting the flow rates of the active lines to 100 sccm, an N_2 flow with 100 sccm is applied during the deposition of Al_2O_3 grains. Due to this relatively high flow rate from the passive line 6 (on the left) the TMA from line 1 (at the wafers notch) seems to be flushed to the right before the saturation of precursor molecules is accomplished on the whole substrate. Thus, the distribution of Al_2O_3 grains might be prevented in the upper half of the wafer.
Due to the same effect, the distribution of conductive ZnO grains is also prevented by the relatively high N_2 flow rate at line 1 during pulsing with DEZn at line 6. The N_2 flushed the DEZn molecules towards line 4, which might be the reason why sheet resistances are lower in the upper half of the wafers.

Since flow rates of precursor lines cannot be changed during a process, all flow rates of active lines were set to 100 sccm, while flow rates of passive ones remained at 50 sccm. By increasing the pulsing and purging time of the TMA during the deposition of Al_2O_3 grains, the discussed effect can be minimised so that distribution of ZnO and Al_2O_3 grains are more homogeneous which results in the smallest $1\,\sigma$ error under the tested depositions.

4 Experimental Verification

4.1 Evaluation of Humidity-Sensitive ALD Composites

First, suitable ALD composite recipes have to be evaluated regarding their sensitivity to humidity. Therefore, sensor structures are fabricated with four different ALD composites which were verified as appropriate concerning island growth and granularity in Chapter 3.3.4. These composites differ in the ratio of ZnO to Al_2O_3 and the size of the individual grains.
Composites with the most promising parameter settings are used as the humidity-sensitive layer in the implementation of the presented encapsulation stack on a 3D dummy implants.

4.1.1 Sensor Structures used

In this chapter, the sensor structures for the evaluation of different composites are presented. As discussed in Chapter 3, the humidity-monitoring sensor within the encapsulation stack consists of a humidity-sensitive ALD composite which isolates the two surrounding metal layers from each other. These metal layers serve as electrodes and measure the inherent resistance of the composite which changes with respect to the amount of diffusing water molecules.
The design of the electrodes is chosen referring to the estimated surface size of an active implant. The sensor area equals the surface area of the bottom electrode which is 10 mm x 10 mm. Sensor design and dimensions are presented in Figure 4.1.

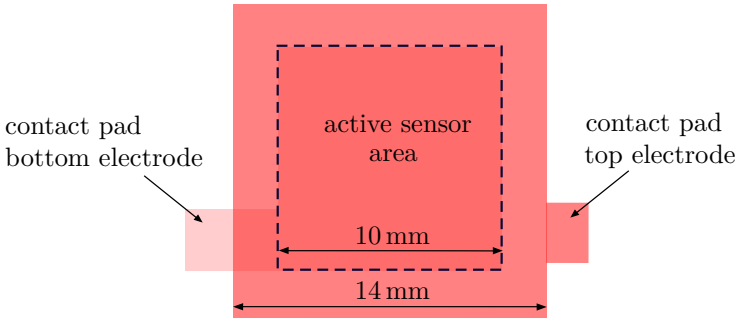

Figure 4.1: Sandwich-type sensor design featuring a bottom electrode with a contact pad to the left and an overlapping top electrode with a contact pad to the right, active sensor area is determined by the area of the bottom electrode (10 mm x 10 mm).

The bottom electrode with a contact pad to the left is electrically isolated from the top electrode by the ALD composite in between. The overlapping top electrode has a contact pad to the right which minimises the risk of shorts during the assembly of wires.

Since a defect-free top electrode does not allow any diffusion of water molecules to the humidity-sensitive ALD composite, further designs with different degrees of perforations have been implemented. These perforations within the top electrode are placed directly above the bottom electrode and serve as humidity access openings to the humidity-sensitive ALD composite underneath the top electrode. Four designs with 0, 10, 25 and 50 openings are implemented. All perforations have an opening area of 100 µm x 100 µm. The design without any openings serves as a reference sensor.
Sensor electrodes are made of about 100 nm thick TiW which was sputtered. Patterning was achieved by photo-lithography and subsequent etching with etching media on the basis of SF_6. Laser-printed foil masks with a resolution of 25.000 dots per inch (dpi) were used for the patterning of the photoresist. The substrate was a silicon wafer with a 45 nm thick isolating Al_2O_3 film.

As discussed in Chapter 3.2.3 and verified in Chapter 3.3.4, ALD composites shall be used as a humidity-sensitive layer in the encapsulation concept of this thesis. The two main parameters, which influence sensitivity of electronic and protonic type humidity transducing materials, are the amount of grain boundaries and the size of the reactive surface area. Therefore, the sensor layer properties

were tailored (as presented in [64]) by varying ratios of deposition cycles of the n-type semiconducting ZnO and the dielectric Al_2O_3.
According to the evaluations in Chapter 3.3.4, four promising mixtures of ZnO and Al_2O_3 grains were used as sensor layer between the electrodes. The four recipes, which are presented in Table 4.1, were generated with a changing number of deposition cycles n for ZnO and Al_2O_3. A sensor with the recipe "ZnO+Al_2O_3 3:6 85SC" was investigated by cross-sectional SEM images at the electrodes contact pads and in the middle part of the sensor. The results are presented in Figure 4.2. Outgoing from the calculated GPC rates from Chapter 3.3.4, a composite thickness of 60 nm was estimated. The actual thickness is 80 nm, both on the substrate and on the TiW-metallisation.

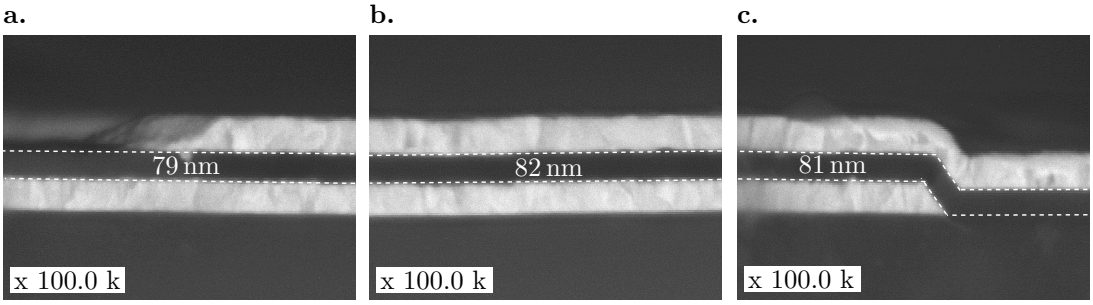

Figure 4.2: SEM cross-section images of a sensor structure with a "ZnO+Al_2O_3 3:6 85SC" ALD composite at the edge of the top electrode (a.), the middle part of the sensor (b.) and the edge of the bottom electrode (c.). Thickness of the humidity-sensitive ALD composite equals about 80 nm.

By using the recipe "ZnO+Al_2O_3 3:6 85SC", small ZnO grains and double-sized dielectric Al_2O_3 grains on the first wafer were targeted so that a ratio of 1 : 2 is obtained. In recipe "ZnO+Al_2O_3 4:4 92SC" ZnO and Al_2O_3 grains are chosen in the same size on the second wafer (ratio 1 : 1). Considering the estimated growth rates of 4 : 4 mixtures in Chapter 3.3.4, a total thickness of approximately 60 nm to 70 nm can be achieved with these two recipes. For the composites on wafers 3 and 4, the number of deposition cycles for ZnO grains were decreased so that smaller ratios could be achieved. With the recipe "ZnO+Al_2O_3 3:9 75SC" a ratio of 1 : 3 and with "ZnO+Al_2O_3 2:8 90SC" a ratio of 1 : 4 was applied on wafers 3 and 4, respectively. For comparability, all composites shall feature a similar total thickness, so that only amount, size and ratio of the established grains play

a role in the sensitivity of the fabricated sensors. Relevant recipe parameters of implemented ALD composites are listed in Table 4.1.

Table 4.1: Utilised recipes for the deposition of ZnO+Al_2O_3 composites for humidity sensing purposes.

	Recipe Names of ZnO+Al_2O_3 composites			
Parameters	3:6 85SC	4:4 92SC	3:9 75SC	2:8 90SC
Wafer number	1	2	3	4
n for ZnO islands	3	4	3	2
n for Al_2O_3 islands	6	4	9	8
Number of super-cycles	85	92	75	90
Grain size ratio ZnO/Al_2O_3	$\approx$ 1:2	$\approx$ 1:1	$\approx$ 1:3	$\approx$ 1:4
Deposition temperature in °C	270			
Pulsing/Purging times for ZnO	0.1 s, 8 s / 0.2 s, 8 s			
Pulsing/Purging times for Al_2O_3	0.2 s, 7 s / 0.1 s, 10 s			
Line 1 flow rate in sccm	100			
Line 2 flow rate in sccm	50			
Line 3 flow rate in sccm	50			
Line 4 flow rate in sccm	100			
Line 5 flow rate in sccm	50			
Line 6 flow rate in sccm	100			
Estimated composite thickness in nm	$\approx$ 60	$\approx$ 60	$\approx$ 80	$\approx$ 80
Actual composite thickness in nm	80	72	N/A	85

4.1.2 Measuring Environment

After the fabrication of the wafers with various sensors, characterisation was accomplished at a set-up with a probe station from *Süss MicroTec*. First, the individual resistance of each sensor was measured. Outgoing from a homogeneous mixture of ZnO and Al_2O_3 grains, a specific resistance in the magnitude of the specific resistance ρ of Al_2O_3 (about 10 to 17 mΩcm, [95]) and resulting high resistances in the GΩ range were expected for sensors with the implemented composites. IV measurements were performed with an *Agilent 4155C* Semicon-

ductor Parameter Analyser which was controlled by an *EasyEXPERT group+* device characterisation software. In order to minimise influence from light, the door of the probe station was closed during the IV measurements. Additionally, the chuck was heated to 50 °C for each measurement, independent of sensor or wafer, to create comparable conditions. The electrodes were contacted by needles on micromanipulators. The bottom electrode was used as ground potential, while the top electrode was subjected to the test voltages. Contacting the bottom electrode required the partial removal of the ALD composite, which can be achieved by laser ablation with a UV-laser (even opening edges but long process times for appropriately large openings) or by mechanical scraping (quick manual process but uneven opening edges).

During the IV measurements, the applied voltages were increased slowly with an increment of 0.1 V. As soon as currents in the range of µA were detected, the measurement was interrupted in order not to exceed the breakdown voltage. Sensors with high resistances ($\geqslant 1\,\mathrm{M\Omega}$) were tested further with regard to the sensor signal after the application of a droplet of deionised (DI) water on the sensor surface. Here, IV-t measurements were used, in which the test voltage remained constant over a certain period of time (usually 50 min). Currents were measured and monitored from the moment a water droplet was applied on the sensor surface (with or without perforations in the top electrode) until well after the droplet evaporated. The changes in resistances during the test were calculated and interpreted as sensor signals. The set-up with the probe station, parameter analyser and controlling software is presented in Figure 4.3. The inlet shows a magnified photograph of a contacted sensor with a water droplet on the surface. Since the application of the water droplet is accomplished manually, the door of the probe station needed to be open during the IV-t measurements despite potential influences of light.
ALD composite recipes of sensors, which demonstrated very high resistances (recognisable by leakage currents below µA in the IV measurements up to 5 V) and the behaviour $\delta I/\delta t > 0$ or equivalently $\delta R/\delta t < 0$ in the DI water droplet test, were considered for the implementation of the three-dimensional encapsulation.

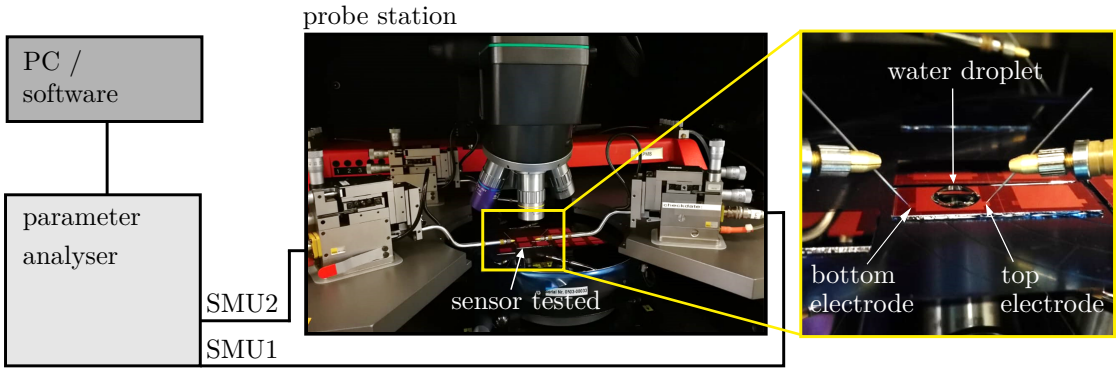

Figure 4.3: Test set-up for characterisation of sensors on the untreated wafer: the probe station protects against light while contact needles on micromanipulators contact bottom and top electrodes of each sensor for the application of test voltages.

4.1.3 Results and Discussion

Sensors of the four wafers (with different ALD composites) were tested in the introduced test set-up. In this chapter, results of investigations concerning sensor response to humidity in form of a water droplet are presented. First, a preliminary investigation of individual resistances of each sensor was performed. Thus, suitable sensors, which showed high initial resistances, could be sorted for the water droplet test in which the sensor reaction to an applied water droplet on the perforated upper electrode was investigated.

Some sensors on the wafers showed resistances in the MΩ range with small leakage currents and corresponding resistances in the upper GΩ-range even up to 24 V during the first characterisations by means of IV measurements. Despite the expectations, some sensors in specific areas of the wafers did not show high resistances during the IV measurements. With only a few tens of Ω at test voltages of 10 or 100 mV and leakage currents of up to several 10 mA, these parts of the sensitive composites on the wafers serve more as low-resistance junctions between the electrodes than as humidity-sensitive films which should show high resistances under room temperature and humidity conditions. Explanations for this effect could be an unbalanced distribution of ZnO and Al_2O_3 grains. An increased amount of ZnO grains in specific areas can lead to an unwanted high electrical conductivity, regardless of the surrounding humidity levels.

The examples, which showed resistances in the MΩ range up to a test voltage

of 10 V, were further investigated with a quick water droplet test. With a constant test voltage of preferably 5 V (test voltage of the multimeter in the second test set-up) smaller voltages IV-t measurements were also performed. Currents were measured and monitored from the moment a water droplet was applied on the sensor surface (with or without perforations in the top electrode) until well after the droplet evaporated.

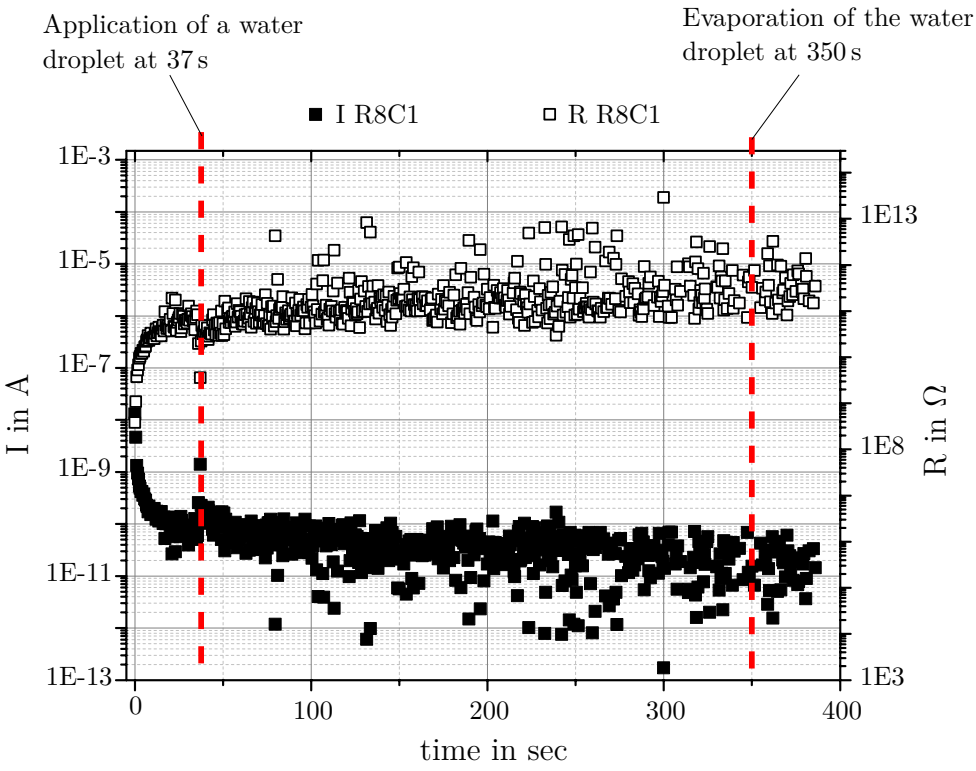

Figure 4.4: IV-t measurement with application of a water droplet on sensor R8C1 (without perforations on the top electrode): monitored current I is presented in the left y-axis, while calculated resistance R is presented in the right y-axis. The sensor does not show any noticeable change of $\delta I/\delta t > 0$ or $\delta R/\delta t < 0$ to the application or evaporation of the water droplet.

Starting with wafer 1 and the recipe "ZnO+Al_2O_3 3:6 85SC", all wafers were tested successively. Sensor nomenclature is uniformly based on the position of the respective sensor on the wafer. Through the combination of the row and column numbers, each sensor can be distinguished from the others. For example, the sensor in row 3 and column 1 is called R3C1, and so forth.
First a sensor without perforations (R8C1) on the top electrode was tested with a test voltage of 5 V. In the first 20 s, a running-in behaviour can be seen in the

current signal. Presumptions for this behaviour are scattered light which may influence the conductivity of the composite with semiconducting ZnO components or polarisation effects in the composite layer as soon as the test voltage is applied. However, the reason cannot be explained in more detail without further investigation. After approximately 35 s, the signal drifted with approximately 15 pA in 50 s which was sufficiently stable in order to apply a water droplet. As expected, no perceptible changes in the current I or the resistance R were seen during the whole time of water droplet application (see Figure 4.4).
Other sensors which demonstrated resistances in the MΩ range at test voltages of up to 15 V were tested with the quick water droplet test. At the start of each measurement, the running-in behaviour can be seen in every sample tested. After approximately 50 s, water droplets were applied.

Five sensors on wafer 1 showed a positive sensor response and presented a change of $\delta I/\delta t > 0$ during the time of water droplet application. The times of droplet application, droplet evaporation, as well as shift in measured current and resulting shift in resistance for each positively tested sensor is summarised in Table 4.2. Measured currents of these sensors are presented in Figure 4.5.

Table 4.2: Summarised results from sensitive sensors ($ZnO+Al_2O_3$ 3:6 85SC) in the water droplet test: respective number of perforations in the top electrode, time of droplet application and evaporation and test voltages are presented. Resulting changes in current and resistance during the droplet application are calculated.

Sensor	Number of perforations in the top electrode	Time of droplet application	Time of droplet evaporation	Test voltage	Averaged δI during droplet application	Corresponding δR in sensor resistance
R3C6	10	98 s	935 s	2 V	≈ 200 µA	≈ 200 GΩ
R3C7	10	78 s	1200 s	5 V	≈ 15 µA	≈ 25 GΩ
R4C1	25	61 s	425 s	5 V	≈ 10 µA	≈ 50 GΩ
R7C6	50	98 s	620 s	1 V	≈ 0.4 nA	≈ 96.7 GΩ
R8C7	2 macroscopic defects	103 s	710 s	1 V	≈ 0.14 nA	≈ 190 GΩ

The investigation time is much longer than the time until the water droplet is evaporated since constant currents values are not achieved directly after the evaporation but with a delay. This is due to the fast water adsorption and the much slower desorption procedure.

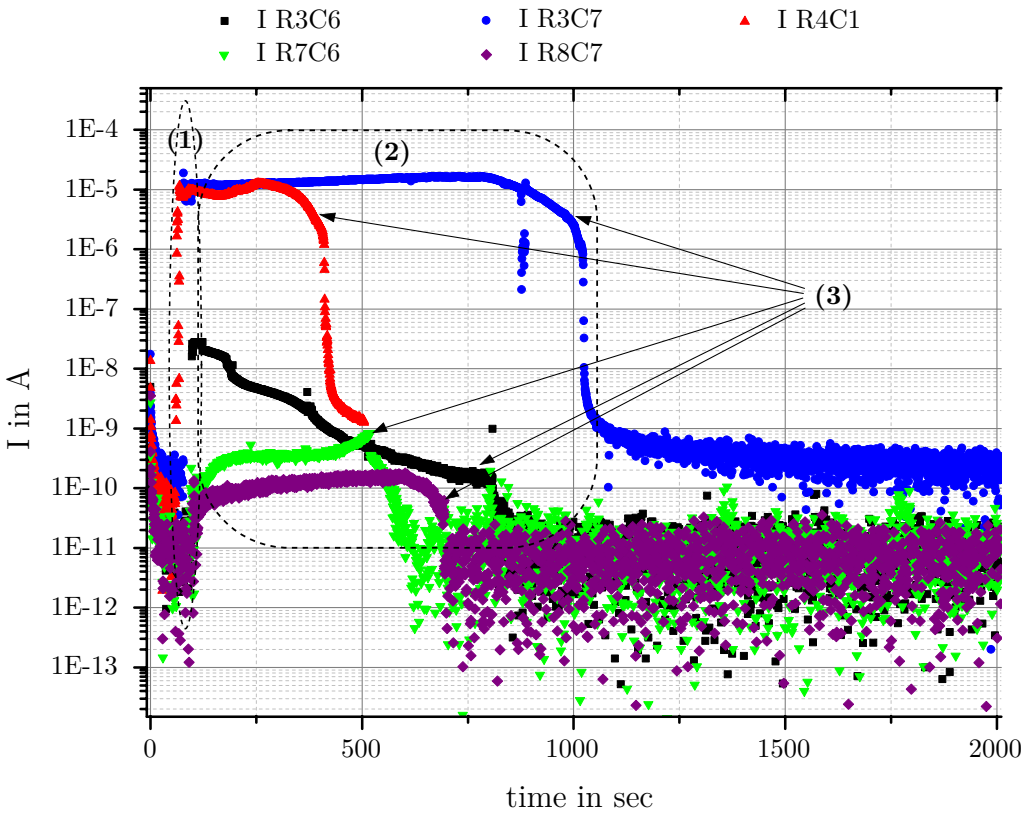

Figure 4.5: Water droplet test on sensors with the humidity-sensitive ALD composite "ZnO+Al_2O_3 3:6 85SC": measured currents show a steep positive gradient after the application of water droplets (adsorption of water (1)). While the water droplets rest on the sensor surfaces, currents demonstrate plateaus whose lengths approximately correspond to the respective evaporation time (2). After the water droplets are evaporated (3), the desorption procedure starts. Desorption ends when the current reaches a constant value.

For each successfully-tested sensor, a steep positive gradient can be seen in the curve at the time of water droplet application. These gradients can be used to indicate that the adsorption procedure (1) is completed within a few seconds. This quick sensor response justifies the suitability of the composite tested for the integration in a humidity-monitoring encapsulation concept for implants. The plateaus in the current signals represent the presence of water droplets during the evaporation processes. Depending on the size of the applied water droplet, evaporation times (2) may vary between tested sensors. Typically, the desorption procedure (3) still continues after the droplet is completely evaporated. The duration of the desorption procedure cannot be precisely determined, as it depends on the respective sensor design and the number of wetted openings in the top electrode. The more perforations are wetted, the stronger is the interaction of

water molecules with the humidity-sensitive layer underneath the top electrode. This is assumed to be the reason why a decrease of the current values (after the evaporation of the droplet) is more pronounced for some sensors than for others. In the case of sensor R8C7, which belongs to the sensor design without perforations, two macroscopic defects were detected in the metallisation of the top electrode. These comparatively large defects are assumed to be responsible for the unexpected positive sensor response in the water droplet test. Summarised results are presented in Table 4.2. The averaged δI during droplet application is extracted from the data, while the corresponding δR in sensor resistance is calculated with the help of Ohm's law (test voltage divided by the actual current value), forming the difference between the initial resistance and the resulting resistance during droplet application.
A proportional correlation between the number of perforations and the change in resistance can not be seen for the tested sensor structures. One reason could be an inaccurate manual application of the droplet on single sensors. If each perforation is not covered with water, the potential for the interaction of water molecules with the humidity-sensitive layer between the electrodes cannot be fully exploited. Another reason could be the obstruction of some perforations by dirt particles, so that not every opening in the top electrode can be considered for the measurement. This is realistic, since the tests are not performed under clean room conditions. A third reason could be the non-homogeneity of the composite on the active area of 10 mm x 10 mm. If some perforations in the top electrode are not above a humidity-sensitive spot, water molecules within these perforations cannot contribute to the change of the sensor signal.

Comparable IV measurements were performed with sensors from wafer 2 which utilises the second ALD composite "ZnO+Al_2O_3 4:4 92SC". A few sensors with inherent resistances in the MΩ range could be detected and further tested. However, none of the sensors on the wafer with the ALD composite "ZnO+Al_2O_3 4:4 92SC" showed a positive sensor response to the application of a water droplet. Thus, no results of the quick water droplet test could be obtained.

In contrast to wafer 2, some sensitive sensor structures could be discovered on wafer 3. Summarised results are presented in Table 4.3.

Table 4.3: Summarised results from sensitive sensors ($ZnO+Al_2O_3$ 3:9 75SC) in the water droplet test: respective number of perforations in the top electrode, time of droplet application and evaporation and test voltages are presented. Resulting changes in current and resistance during the droplet application are calculated.

Sensor	Number of perforations in the top electrode	Time of droplet application	Time of droplet evaporation	Test voltage	Averaged δI during droplet application	Corresponding δR in sensor resistance
R1C4	10	66 s	345 s	5 V	≈ 20 µA	≈ 0.5 TΩ
R3C7	10	72 s	495 s	5 V	≈ 10 µA	≈ 1.6 TΩ
R4C3	25	63 s	422 s	5 V	≈ 10 µA	≈ 1.67 TΩ
R4C6	25	74 s	442 s	5 V	≈ 30 µA	≈ 0.16 TΩ
R5C7	25	99 s	540 s	5 V	≈ 10 µA	≈ 0.5 TΩ

Measured currents of these sensors are illustrated in Figure 4.6.

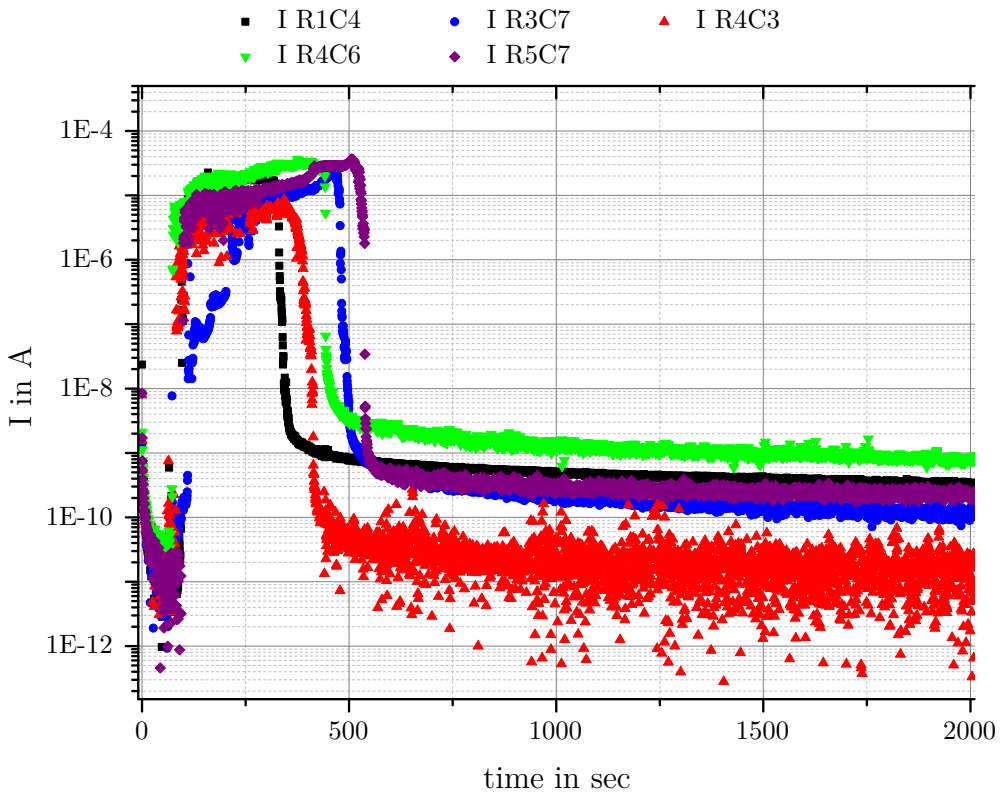

Figure 4.6: Water droplet test on sensors with the humidity-sensitive ALD composite "$ZnO+Al_2O_3$ 3:9 75SC": measured currents show a steep positive gradient after the application of water droplets and plateaus whose lengths approximately correspond to the respective evaporation time. After the water droplets are evaporated, the desorption procedure starts and ends when a constant current value is reached for the respective sensor.

Similar to the results in Figure 4.5, a steep positive gradient can be seen in the presented curves at the time of water droplet application. As expected, the adsorption procedure is completed within a few seconds, while the desorption procedure requires more time, even more than 2000 sec. Since a constant test voltage of 5 V was used for each sensor structure, current signal plateaus demonstrate lengths which correspond to the respective evaporation time of the applied water droplet. A proportional correlation between the number of perforations and the change in resistance can not be seen again. As the main reason, the non-homogeneity of the composite on the active sensor area is assumed.

Summarised results of sensors tested from wafer 4 are presented in Table 4.4.

Table 4.4: Summarised results from sensitive sensors (ZnO+Al_2O_3 2:8 90SC) in the water droplet test: respective number of perforations in the top electrode, time of droplet application and evaporation and test voltages are presented. Resulting changes in current and resistance during the droplet application are calculated.

Sensor	Number of perforations in the top electrode	Time of droplet application	Time of droplet evaporation	Test voltage	Averaged δI during droplet application	Corresponding δR in sensor resistance
R2C6	10	83 s	510 s	5 V	$\approx$ 20 µA	$\approx$ 1.66 TΩ
R3C5	10	97 s	522 s	5 V	$\approx$ 10 µA	$\approx$ 2.5 TΩ
R4C2	25	96 s	560 s	5 V	$\approx$ 10 µA	$\approx$ 1.0 TΩ
R4C7	25	131 s	525 s	5 V	$\approx$ 30 µA	$\approx$ 1.0 TΩ
R6C6	50	88 s	539 s	5 V	$\approx$ 10 µA	$\approx$ 1.25 TΩ

Also for sensors with the composite "ZnO+Al_2O_3 2:8 90SC" a clear adsorption phase at the moment of droplet application and comparable plateaus for the current signal while the droplets slowly evaporate on the top electrodes can be seen. Despite different positions on wafer 2, the adsorption and desorption procedures of the exemplary presented sensors are more comparable with each other than tested sensors of wafer 1 and 3. A more homogeneous distribution of ZnO and Al_2O_3 grains on the whole wafer is assumed. Results of tested sensor structures from wafer 4 are presented in Figure 4.7.

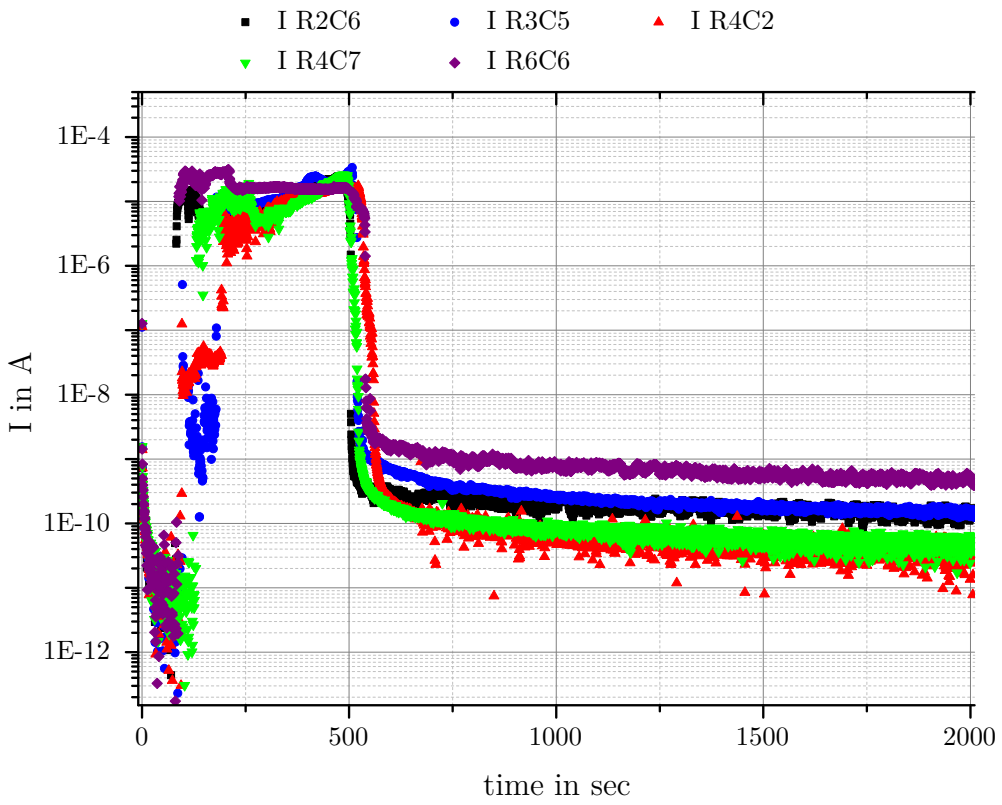

Figure 4.7: Water droplet test on sensors with the humidity-sensitive ALD composite "ZnO+Al_2O_3 2:8 90SC": measured currents show a steep positive gradient after the application of water droplets and plateaus whose lengths approximately correspond to the respective evaporation time. After the water droplets are evaporated, the desorption procedure starts and ends when a constant current value is reached for the respective sensor.

After each sensor on wafers 1 to 4 was characterised by IV and IV-t (water droplet test) measurements, sensors were divided into one of three categories (with respect to their characteristics):

1. sensors with low inherent resistances (red background),
2. sensors with high inherent resistances but without a positive response to the application of a water droplet (yellow background), and
3. sensors with high inherent resistances and with a positive response to the application of a water droplet (green background).

Sensors, which demonstrated small resistances during the IV measurements (leakage currents of up to several 10 mA at test voltages of 10 or 100 mV) are marked with a red background and not considered further. Sensors with a yellow

background showed high resistances in the IV measurements at test voltages of at least 5 V (with maximum leakage currents in the µA range). These ones were further investigated with the water droplet test but did not show a change in resistance. Sensors which additionally demonstrated a positive response to the application of a water droplet are marked with a green background.

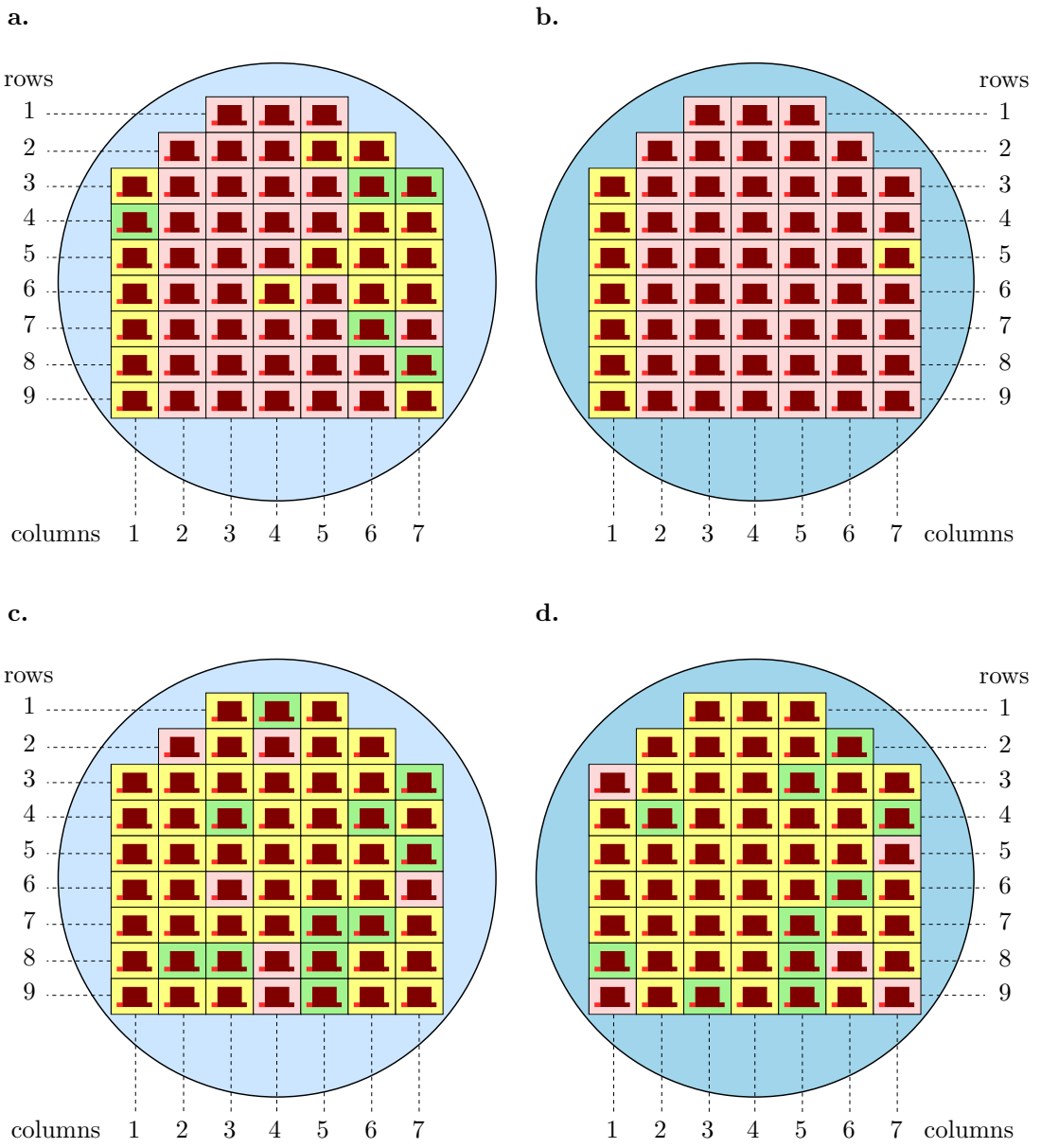

Figure 4.8: Summary of the results, divided into three categories (red for sensors with low inherent resistances, yellow for sensors with high inherent resistances but without positive responses to water droplet application, and green for sensor with high inherent resistances and positive responses to water droplet application): a., b., c. and d. show results from wafer 1 ("3:6 85SC"), 2 ("4:4 92SC"), 3 ("3:9 75SC") and 4 ("2:8 90SC"), respectively.

The results are illustrated in Figure 4.8, in which a., b., c., and d. present the achieved yield for wafer 1, 2, 3 and 4, respectively.

This summary certifies that the aim of fabricating a humidity-sensitive ALD composite has been achieved. Several sensors on the wafers 1, 3 and 4 showed a positive response to the application of water droplets. This implies (at least on several positions on specific wafers) a successful mixture of humidity-sensitive ZnO grains with uniformly integrated Al_2O_3 grains by applying the recipes "3:6 85SC", "3:9 75SC" and "2:8 90SC".
Nevertheless, the yield for wafer 1 is very poor since only five suitable sensors could be detected. Wafer 2 does not own appropriate sensors at all, which is attributed to the highest used ZnO to Al_2O_3 ratio of 1 : 1. Testing the composites with ratios 1 : 3 ("ZnO+Al_2O_3 3:9 75SC") and 1 : 4 ("ZnO+Al_2O_3 2:8 90SC") showed a tremendously increased number of appropriate sensors with high initial resistance and suitable response of the sensor signal to an applied water droplet. The predominant red zone from previously characterised wafers 1 and 2 has almost disappeared in wafers 3 and 4. Additionally, the number of humidity-sensitive sensor structures has doubled in comparison to wafer 1. Thus, the decrease of the ZnO content can be seen as an effective measure in order to achieve more spots on the wafer with a balanced distribution of ZnO and Al_2O_3 grains in ALD composite. Nevertheless, all three recipes from wafer 1, 2 and 3 were applied to the three-dimensional substrates as the sensitive layer in the encapsulation stack.

In order to verify the repeatability of these measurements, IV characterisations were performed a second time after the droplet test. Even though current values decreased directly after the evaporation of the droplet, the high resistances achieved during the desorption procedure could not be recorded in the second IV measurement. Unfortunately, each sensor, which owned a perforated top electrode so that the ALD composite had direct contact to the applied water droplet, showed short circuit behaviour with low resistances and high leakage currents afterwards. This applies to both sensitive and non-sensitive structures with initial resistance values in the MΩ range or higher. Respective measurements as examples for IV measurements before and after the droplet test are presented in the appendix. These changes of sensor structure characteristics could not be

reversed by drying process, such as tempering at 100 °C for two hours. Thus, the ability of detecting humidity is irreversible for the developed ALD composites. The explanation may lie in a delayed chemical reaction of H_2O with the ZnO component of the composites. It is assumed that the reduction of semiconducting ZnO grains form more conductive Zn particles. These particles settle between the Al_2O_3 grains and build conductive Zn bridges between the electrode layers as soon as the test voltage is no longer applied. This would change the electrical properties of the composite irreversibly. One possible reaction could be the direct reduction of ZnO in aqueous solutions, as presented in the following equations.

$$\mathrm{ZnO\,(s) + 2\,H_2O\,(l) + 4\,e^- \longrightarrow 2\,Zn\,(s) + 4\,OH^-\,(aq)} \tag{4.1}$$

Simultaneously, the oxidation of hydroxide ions OH^- release the required electrons.

$$\mathrm{4\,OH^-\,(aq) \longrightarrow O_2\,(g) + 2\,H_2O\,(l) + 4\,e^-} \tag{4.2}$$

The whole redox reaction can be summarised to:

$$\mathrm{2\,ZnO\,(s) \longrightarrow 2\,Zn\,(s) + O_2\,(g).} \tag{4.3}$$

Another reaction could be the reduction of ZnO to Zn due to the lightly acidic property of the DI water (measured ph value ≈ 6.5). Dissolution of carbon dioxide (CO_2) from the atmosphere in DI water forms carbonic acid (H_2CO_3) [96]. The reaction of carbonic acid with further water molecules forms an hydronium ion (H_3O^+) and a hydrogen-carbonate ion ($HCO_3{}^-$).

$$\mathrm{CO_2\,(g) + H_2O\,(l) \rightleftharpoons H_2CO_3\,(aq)} \tag{4.4}$$

$$\mathrm{H_2CO_3\,(aq) + H_2O\,(l) \rightleftharpoons H_3O^+\,(aq) + HCO_3{}^-\,(aq)} \tag{4.5}$$

In contact with the resulting solution, the ZnO grains in the composite can be reduced by hydronium ions [97] which leads to following equations.

$$\mathrm{ZnO\,(s) + 3\,H_3O^+\,(aq) \rightleftharpoons Zn^{2+}\,(aq) + 3\,H_2O\,(l)} \tag{4.6}$$

Similarly to electrolysis, the resulting Zn^{2+} ions are immediately reduced to Zn by provided electrons from the solution.

$$\mathrm{Zn^{2+}\,(aq) + 2\,e^- \rightleftharpoons Zn\,(s)} \tag{4.7}$$

The standard potential for zinc is $-0.76\,\mathrm{V}$ [98]. With an applied voltage of $5\,\mathrm{V}$ during the resistance measurement (test voltage of the multimeter used), the required potentials for both presented reduction types of ZnO are provided.
Both presented reduction processes are expected for tests with NaCl-solution (H_2O with dissolved Na+ and Cl^- ions) instead of DI water as well. Here, direct reduction can be performed due to the available H_2O molecules while reduction through H_3O^+ is possible since required absorption of CO_2 from the atmosphere also occurs in NaCl-solutions.
The reduction of ZnO changes the composition and thus the electric property of the sensitive material, irreversibly, which means that the detection of water molecules can be performed only once. Within a disposable implant encapsulation, a non-repeatable signal is absolutely sufficient for the planned application of water detection.

4.2 Implementation of the Encapsulation Concept on 3D Substrates

4.2.1 3D Substrate Designs

Silicon circuit boards were designed and fabricated in order to serve as substrates for the three-dimensional implementation of the developed encapsulation stack. Therefore, various chip sizes and circuitry layouts were chosen which are presented in Figure 4.9. Each layout includes two metal pads which serve as contact pads for the electrical connection of the bottom and top electrode layer of the humidity-sensitive sensor structure within the encapsulation stack. Additionally an area for the assembly of a transponder ASIC is provided in each layout.
Layouts V1.1 (a.) and V1.2 (b.) show slim versions. The contact pads for the electrode layers, rp and rn, are directly connected to the two big contact pads at the top of the chip to which an additional measuring device can be connected. Thus, the resistance between the sensor electrodes can be measured. An electrically unconnected ASIC can be used as a dummy chip which complicates the substrate topography for three dimensional ALD processes.
Layouts V2.1 (c.) and V2.2 (d.) show the large versions. These designs allow the assembly of an active transponder ASIC which allows sensor signal processing of

the humidity-sensitive sensor structure as well as energy and data transmission through a coil. Therefore, three bonding pads, two for antenna connections (antN and antP) and one for the operation voltage (vddu), are provided at the top end of the substrate.

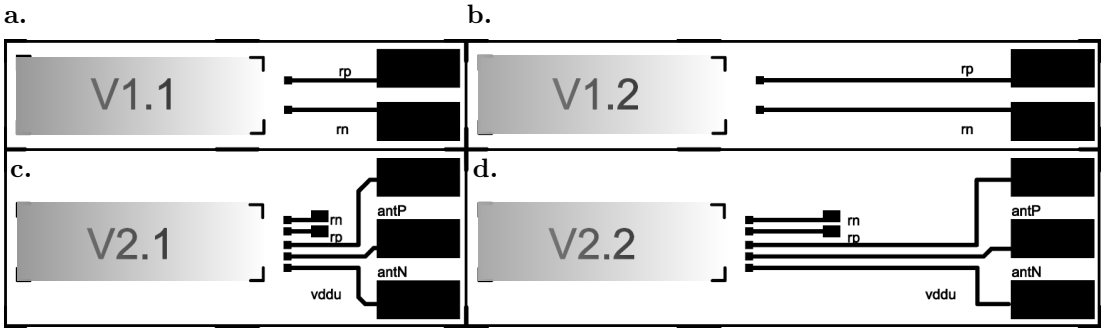

Figure 4.9: Four types for a simplified circuit board (in two different lengths) have been designed: a. and b. show slimmer versions which allow monitoring of the inherent resistance of the integrated humidity-sensing structure by means of additional resistance measuring device; c. and d. present larger versions on which active transponder ASICs may be assembled, which provide humidity sensor signal processing on the chip.

These pads lead to bonding pads in close proximity to the active transponder ASIC. Thus, an external antenna can be connected and the induced operation voltage can be buffered. Since one of two antenna potentials serves as ground potential, no further ground connections are needed. The contact pads of the electrode layers are connected to corresponding bonding pads of the ASIC (rp and rn) which is responsible for the detection of a significant change in resistance between the electrode layers within the encapsulation stack.

4.2.2 Process Flow of 3D Encapsulation

Three dimensional substrates of each design were coated with a 2.0 µm to 5.0 µm parylene F layer with a short time heat resistance of up to 350 °C. This first process step was accomplished by the company *Heicks Parylene Coating GmbH*. The bigger pads at the end of the substrate were not coated so that these parylene-free areas could be wired electrically in further steps. Photographs of parylene-coated substates of the version V1.2, without and with assembled dummy ASICs, are presented in Figure 4.10 a. and b.. In c., version V2.2 is presented which was equipped with an active transponder ASIC by using respective assembly material

(a heat resistant epoxy for die-bonding and glob-top purposes, see Chapter 3.1.2). The chip and the assembly material are also conformally coated with parylene F. The next step is the deposition of the three-dimensional bottom electrode layer which also guarantees an ILC with the opened contact pad, as proven in Chapter 3.3.3. In order to promote the growth of ruthenium on top of parylene, a very thin film of Al_2O_3 with only 20 deposition cycles was applied to serve as adhesive. This Al_2O_3 film barely influences the electrical connection between the opened contact pad and ALD electrode layer. The increase in resistance of the ILC is negligibly small due to the minimal thickness of the dielectric Al_2O_3.

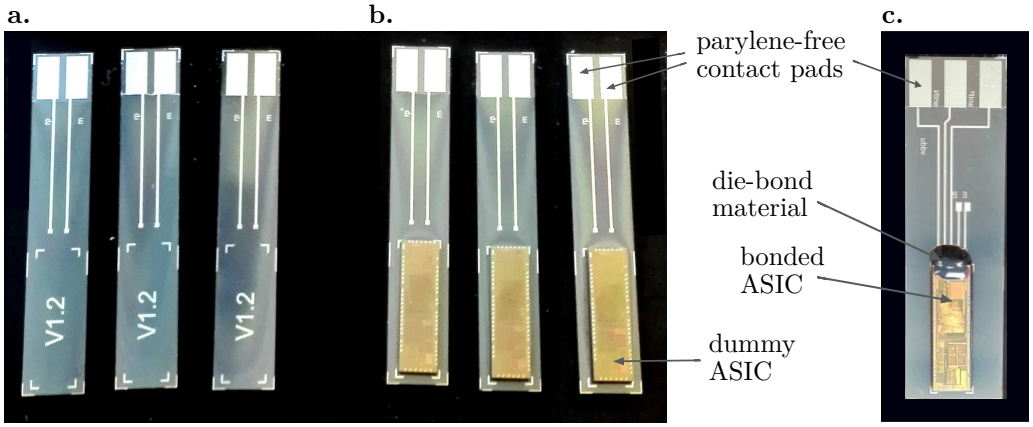

Figure 4.10: Photograph of parylene F-coated circuit boards (type V1.2): a. shows blank samples while b. shows samples with dummy ASICs at one end which serve a more difficult topography for 3D coating. The two contact pads at the opposite end of the circuit board are omitted.

Generally, the ALD window for Ru processes with the *Picosun* system used presents process temperatures from 275 °C to 330 °C (see Table 2.4). At this point of this thesis, reconstruction works of the ALD system were necessary, which in the following only allowed Ru processes above 360 °C. Therefore, samples without parylene F coating were also considered for further encapsulations.
In order to avoid depositions on the two (already parylene-free) assembly pads, masking with a black marker from Lumucolor (by *Staedler*) was performed before the chips were clamped into an aluminum bracket which helped with the placement of the chips in the process chamber.

In Figure 4.11, photographs of three different substrate types at sequential progress levels during the implementation of the developed 3D encapsulation

stack are presented. In a.1 a sample of a parylene-coated substrate is presented, in which the formation of cracks was so massive during the ALD process, so that only partial deposition of Ru could be achieved. Even though the growth behaviour of the composite was much more adequate (see Figure 4.11 a.2), samples with heavily damaged parylene F layers were sorted out and not further processed. In Figure 4.11 b., other parylene coated circuit boards are presented. The mentioned cracks due to exceeded processing temperatures occurred in attenuated form at the edges of these samples. Although further processing was possible, sufficiently enclosing three-dimensional depositions with very thin ALD films could not be achieved. Therefore, in addition to the substrates with parylene coating, substrates without parylene coating were also covered with the developed 3D encapsulation stack (see Figure 4.11 c.).
Since the isolating parylene between the two contact pads on the circuit board is missing here, masking the wire and the pad for the top electrode layer was performed with the aforementioned black marker before the bottom electrode was applied. In Figure 4.11 c.1, one chip (without parylene coating) is presented after the deposition of the bottom electrode. The electrical connection with the respective pad is accomplished during the ALD process. The second pad is opened after removing the mask by mechanical scraping and isopropanol (IPA)-soaked wipes. The layer stack in the highlighted areas is illustrated using the schematic cross-sections at the pad for the bottom electrode layer in Figure 4.11 b.1 and at the released pad for the top electrode layer in Figure 4.11 c.1.
In Figure 4.11 b.2 and c.2, comparable substrates were photographed after the deposition of the ALD composite and the opening of the pad for the top electrode layer by laser ablation (see schematic cross-sections). On the parylene coated substrate, defects at the chip corners are still visible, even though the composite layer encloses even Ru-free areas.

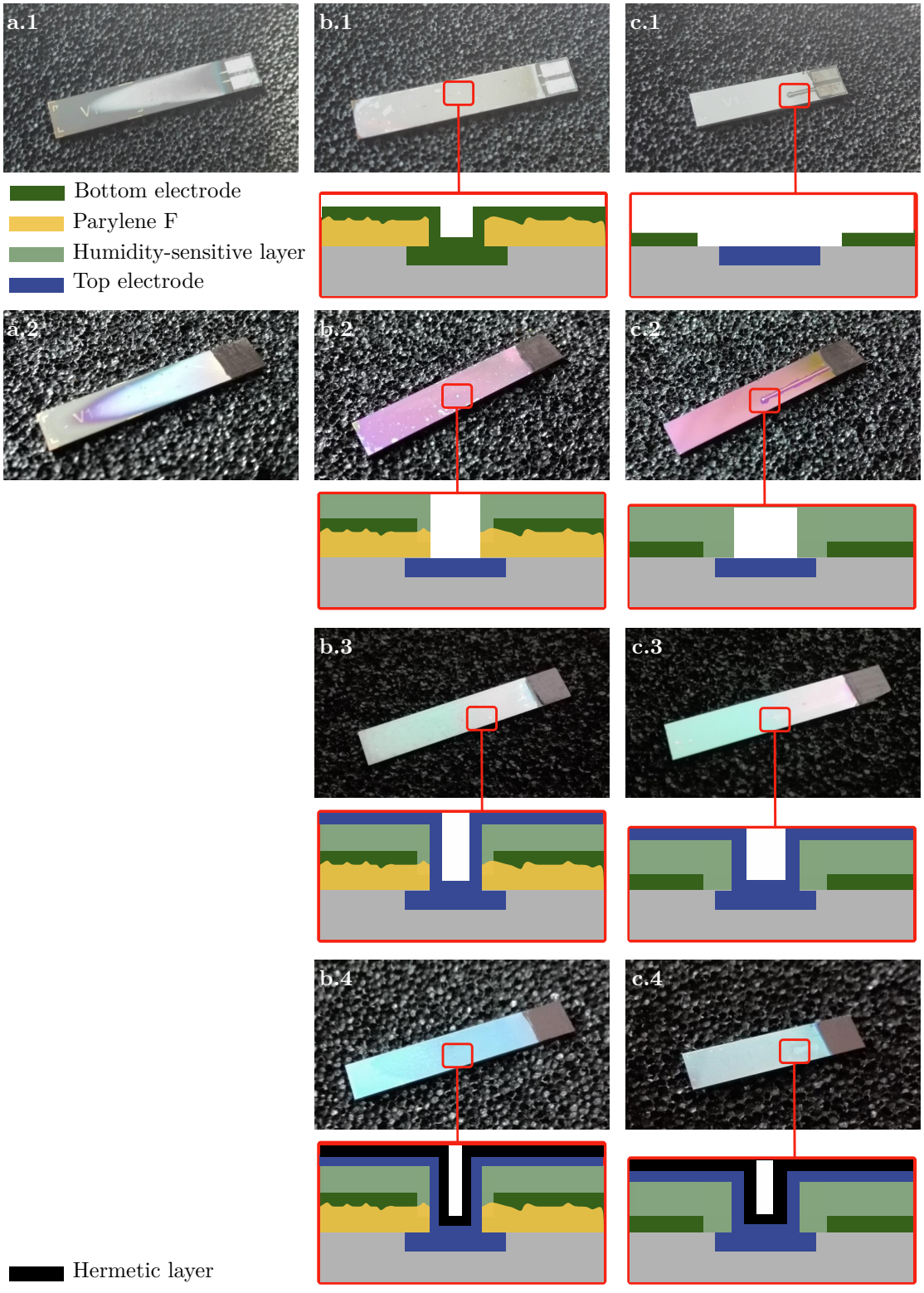

Figure 4.11: Photographs of Si circuit boards: a. and b. present parylene F-coated chips with massive cracks in the chip edges, especially in a.; c. presents a chip without parylene coating. Subordinate figures represent the 3D encapsulation stack in various progress steps: 1 with bottom electrode layer, 2 with the humidity-sensitive ALD composite, 3 with top electrode layer and 4 with hermetic Ta_2O_5-layer.

In Figure 4.11 b.3 and c.3, the ALD of the top electrode layer and the simultaneous electrical ILC with the respective pad on the circuit board are achieved. The growth of Ru is more successful in this process step, since the ALD composite serves as a adequate adhesion layer. Finally, a hermetic Ta_2O_5 sealing layer is applied to all substrates on top of the top electrode layer.

In order to prove the isotropic growth of the single ALD layers, SEM investigations after specific process steps were performed with parylene-coated and parylene-free substrates. Figure 4.12 presents SEM images which reveal the growth of each encapsulation layers at different positions of a parylene-coated substrate. In a., b. and c., the growth behaviour of Ru as the bottom electrode on top of the parylene F is shown. Even though a very thin Al_2O_3 film was applied as an adhesion layer, the sufficient growth of Ru is limited to the substrate surface and the upper chip edges. On the substrate backside, only partial Ru deposition can be seen. Nevertheless, the humidity-sensitive ALD composite encloses the surface, the backside and both side walls of the substrate, sufficiently.

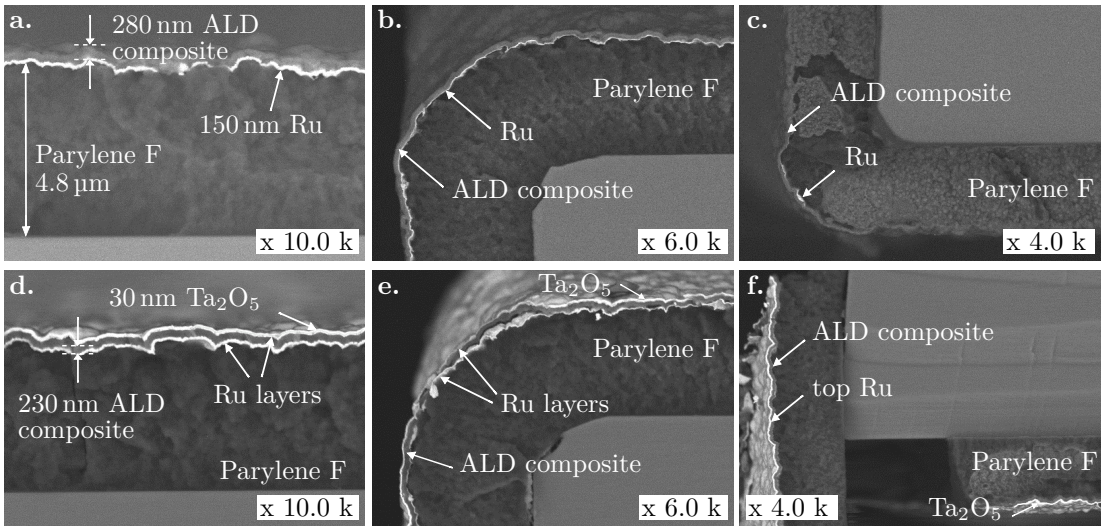

Figure 4.12: SEM investigations of a parylene-coated substrate after the deposition of the bottom electrode layer and the humidity-sensitive ALD composite at the substrate surface (a.), at the edge (b.) and at the backside (c.). Additional depositions of the top electrode layer and the hermetic Ta_2O_5-layer were accomplished and investigated at comparable positions in the figures d., e. and f..

In Figure 4.12 d., e. and f., cross-sections after the additional deposition of the top electrode layer and the hermetic Ta_2O_5-layer are presented. The second

Ru layer grew more successfully. As the ALD composite obviously worked better as an adhesive layer, the top electrode layer can be found on each side wall of the substrate. The growth of the ≈ 30 nm Ta_2O_5-layer is barely visible on top of the Ru due to the small layer thickness and the bright colour (very similar to the brightness of Ru) in the SEM investigations.
Nevertheless, the extraordinary high process temperature of above 360 °C leads to degradations in the parylene layer (see Figure 4.12 c.). Due to the thermal stress, the parylene cracks which leads to delamination, as illustrated in Figure 4.12 f.

Figure 4.13 presents SEM images which reveal the growth of each encapsulation layers at different positions of a parylene-free substrate. Since the degradation problem of the parylene layer at elevated process temperatures is not relevant here, deposition results of Ru as bottom electrode layer are more successful regarding three-dimensionality and reproducibility. As represented in 4.13 b. and e., even the edges of the substrate are sufficiently coated with each of the applied ALD thin films.

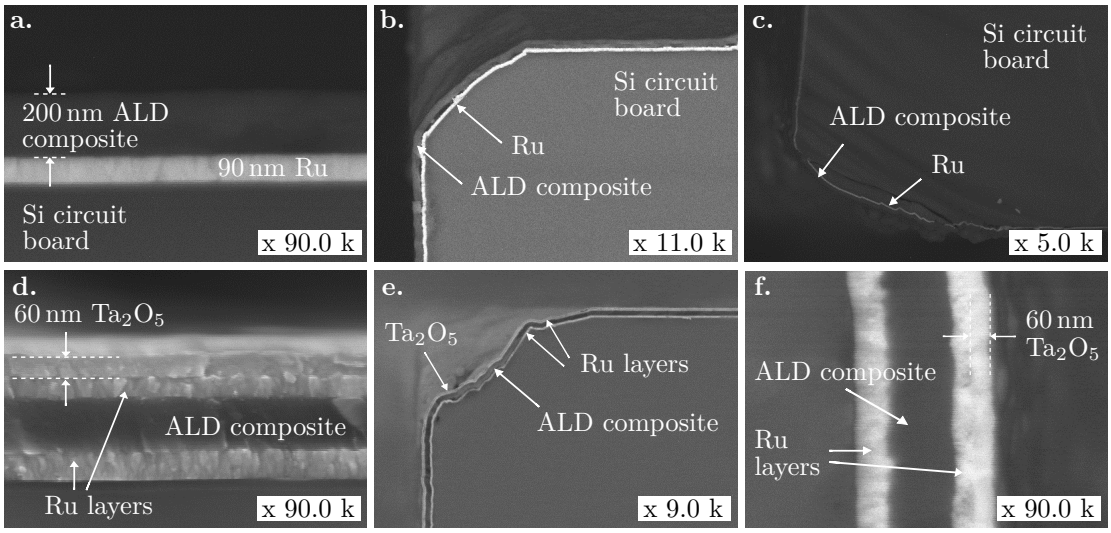

Figure 4.13: SEM investigations of a parylene-pree substrate after the deposition of the bottom electrode layer and the humidity-sensitive ALD composite at the substrate surface (a.), at the edge (b.) and at the backside (c.). Additional depositions of the top electrode layer and the hermetic Ta_2O_5-layer were applied and investigated, also at the surface (d.), edge (e.) and side wall (f.) of the substrate.

Thus, the implementation of the developed encapsulation stack, consisting of four functional layers, was achieved on a three-dimensional substrate. Unexpected

hardware problems in the ALD system did not allow for successful deposition of Ru at process temperatures below the maximum operating temperature of parylene F (350 °C). The elevated process temperatures over several hours lead to the formation of cracks as a result of the parylene degradation. After the first deposition of Ru as the bottom electrode layer, most parylene-coated samples were difficult or not coatable at all, which made further procession impractical. The parylene-free circuit boards, which were used as a back-up solution, served as useful substrates for the implementation of the three-dimensional encapsulation stack, even though manual masking was required before the first electrode layer could be applied.

Opening specific materials in order to guarantee functioning ILC at the contact pads for the electrode layers was achieved by laser ablation, as developed in Chapter 3.2.2. The actual laser ablation parameters used during the implementation of the 3D encapsulation stack are listed in Table 4.5.

Table 4.5: Actual laser ablation parameters used during the 3D implementation of the encapsulation stack.

	Material	Thickness in nm	Trigger mode	Energy level	Cut size in µm x µm	Objective (magnification)
Green laser	Ru	≈ 90	Burst 10x	High, 46	50 x 50	50 x
UV laser	Parylene F	≈ 3500	Burst 3x	High, 30	40 x 40	100 x
	$ZnO+Al_2O_3$	220	single shot	High, 24	100 x 100	100 x
	$ZnO+Al_2O_3$ and Parylene F	≈ 3700	single shot	High, 76	100 x 100	100 x

4.2.3 Measuring Environment

Testing of the 3D encapsulations were accomplished in a test set-up within a climate chamber from *CTS*. A constant level of relative humidity (50 %) and a predetermined temperature of 37 °C, which represents the usual temperature of the

human body, were chosen. For measuring the initial resistances of the humidity-detecting layer within the encapsulation, each encapsulated circuit board was equipped with wires. As an adhesive, conductive silver paste (*EPO-TEK H20E-frozen* by *Polytec*) was used. Resistances of structures under test were measured by a 4-wire measurement with a digital multimeter *Keysight Technologies 3458A*. A micro-controller alternately selected each substrate to be measured through relays, so that three substrates could be tested at the same time. All components in the test set-up are controlled by a *LabVIEW* program with a specific measurement sequence which allowed for an automatic measuring procedure. An additional reference sensor monitors RH levels and temperatures within the climate chamber during the tests. The set-up is schematically presented in Figure 4.14.

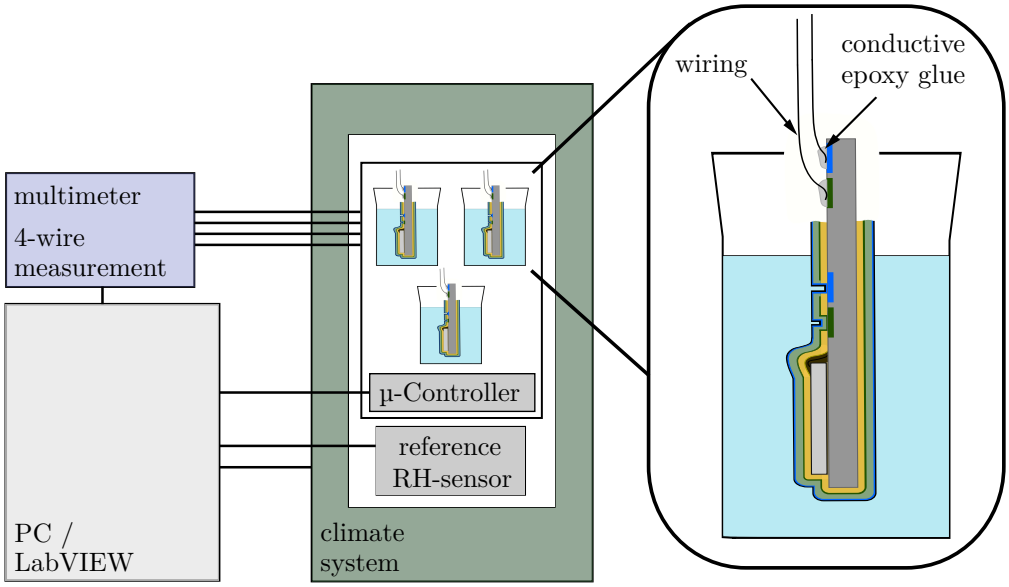

Figure 4.14: Automatic set-up for testing the implemented 3D encapsulations: 3 structures, which are alternately selected by a micro-controller, are placed into a climate and temperature system with an additional reference sensor for humidity and temperature. A 4-wire resistance measurement is performed by a multimeter outside the climate chamber. Measurements at constant humidity level and temperature are performed automatically by a *LabVIEW* software and specific measurement sequence.

First, initial resistances of the substrates under test, which were fixed perpendicularly on a carrier plate with the help of capton tape, were measured in the dry state (at 37 °C and 50 % RH). After a certain time period, the substrates were immersed in containers containing a 0.9 % NaCl-solution which were also tempered to 37 °C in the climatic chamber (see Figure 4.15). For each structure

tested, the resistance valued did not change by only immersing into the NaCl-solution. Hence, the substrates were pulled out and scratched manually with tweezers or a scalpel in order to destroy the upper thin film layers of the encapsulation stack. This preparation step exposes the sensitive ALD composite to the aqueous NaCl-solution so that interactions, which decrease the resistance of the composite, can occur when the substrate is immersed again into the container.

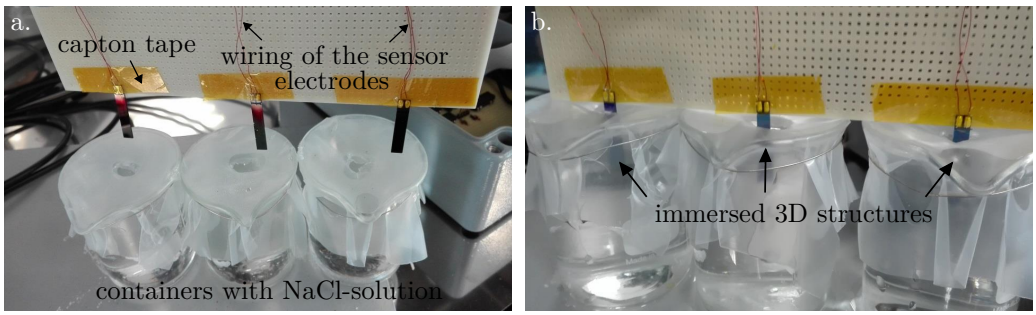

Figure 4.15: Set-up within the climate chamber presenting three 3D-encapsulated and wired structures which are perpendicularly fixed on a carrier plate with the help of electrically isolating capton tape. In a. the structures are measured in the "dry state", while in b. the structures are immersed into containers filled with 0.9 % NaCl-solution and measured in the "wet state". The containers are provided with a flexible and moisture-resistant film (perforated in the middle) which prevents immediate evaporation of the solution.

Influences by light are suppressed by light shielding while influences by temperature are negligible due to tempered NaCl-solutions in each container which are preserved in the climate chamber. Thus, changes in resistance may only result from the contact of aqueous solution and the sensitive film through the consciously applied defect. These macroscopic defects are investigated by SEM at a fracture right across such a scratch on a 3D substrate with a "ZnO+Al_2O_3 3:6 170SC" composite film. One examined scratch is presented in Figure 4.16 in which the left inlet shows a tilted view on the edge of the scratch and the right inlet demonstrates the cross-section directly at the fracture itself, revealing the stack of applied ALD-films which are two 50 nm thick Ru layers, the 170 nm ALD composite and about 40 nm of Ta_2O_5.

Neither optical (by SEM) nor electrical investigations revealed any short-circuits between the electrode layers of the encapsulation stack, caused by scratching the surface of the structure. In order to expose even more of the sensitive

ALD composite, structures with scratched surfaces, which did not show a positive response to the immersion into NaCl-solution, have additionally been broken.

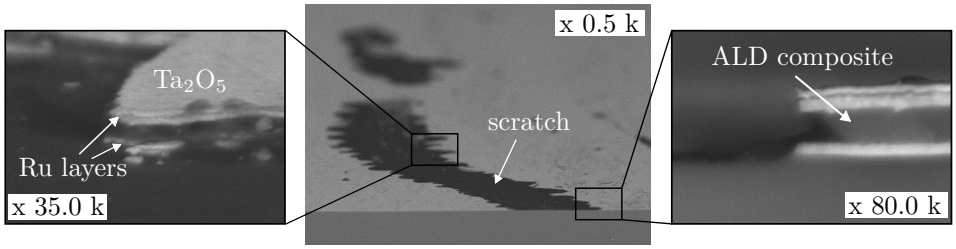

Figure 4.16: Consciously applied scratch on the surface of the encapsulated 3D substrate in order to expose the sensitive ALD composite: left inlet shows a tilted view on the edge of the scratch while the right inlet presents the cross-section at the right edge, revealing the stack of applied ALD films.

Hence, a larger area of the composite was exposed at the cross-section of the specific structure. Although this method does not represent a real scenario, it has been applied several times per structure in order to find a sensitive spot of the composite. The 3D structures have been broken from bottom to top, piece by piece, until the contact pads for the electrode layers (rp and rn) were reached. Representative results are presented in the following chapter.

4.2.4 Results and Discussion

Before tests with and without the use of NaCl-solutions started, inherent resistances of each 3D structure were measured. Thus, structures with resistances with smaller than 800 Ω were sorted out. These small values indicate defects in the initially isolating composite films between the electrode layers. For comparison, intact composite layers in the test structures in Chapter 4.1, even with smaller thickness of about 70 nm to 85 nm, demonstrate higher resistances in the range of MΩ or GΩ (see curves presented in the appendix). Unfortunately, about half of all 3D structures had to be sorted out because of these defects. The high number of defective structures is due to the manual handling of the 3D structures during the 4-step ALD process flow which requires clamping and releasing from an aluminum bracket before and after each deposition step. Thereby, more particles and defects are brought onto the substrates so that the individual ALD layers are prevented from growing correctly which leads to uncoated spots during the composite deposition and thus to short circuits between the electrode layers.

Structures with resistances above 800 Ω have been investigated in the described measurement set-up. Here, big variations with regard to the initial resistance of each structure, which did not directly relate to the respective ALD composite, have been detected. These variations are based on process deviations on die-level which may be impurities in the composite layers or layer thickness irregularities, but were not taken into account for further characterisations.

In Figure 4.17 test results of two 3D structures with "2:8 150SC" composites are presented. The running-in behaviour of the signals at the beginning of the measurement cannot be seen due to the scaling of the x-axis.

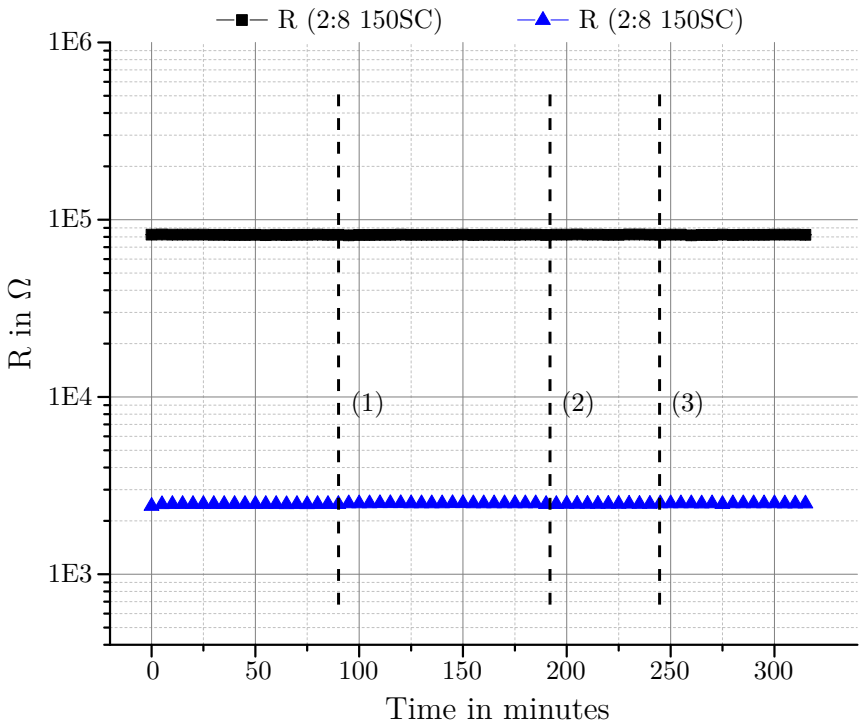

Figure 4.17: Testing of two 3D structures with "2:8 150SC" composite: measured resistances in the dry state, after immersing the structures into the tempered NaCl-solution (wet state) in (1), after scratching the surface and damaging the encapsulation in (2) and after immersing the scratched structures again in (3). There is no detectable change in the resistance signals for both structures.

Both structures were tested in the dry state first and immersed into tempered NaCl-solutions after 90 min (1). After a further 100 min (no signal drifts detectable), structures were taken out of the solution and scratched on the surface

by tweezers (2). The resistances were monitored for another 55 min, then the structures were immersed a second time (3). Contrary to expectations, the resistance values did not show any change after the exposed ALD composite was in direct contact with the aqueous solution.
In Figure 4.18 test results of three 3D structures with "3:9 180SC" and "3:6 170SC" composites are presented. Before starting the test, these structures were broken so that their cross-sections were exposed to the surround conditions. First, the structures were tested in the dry state first until they were immersed into tempered NaCl-solutions after 110 min (1). Here, again contrary to expectations, resistances of immersed structures did not change within the solution. After a further 85 min, structures were taken out of the solution (2). Monitored resistance values did not show any change.

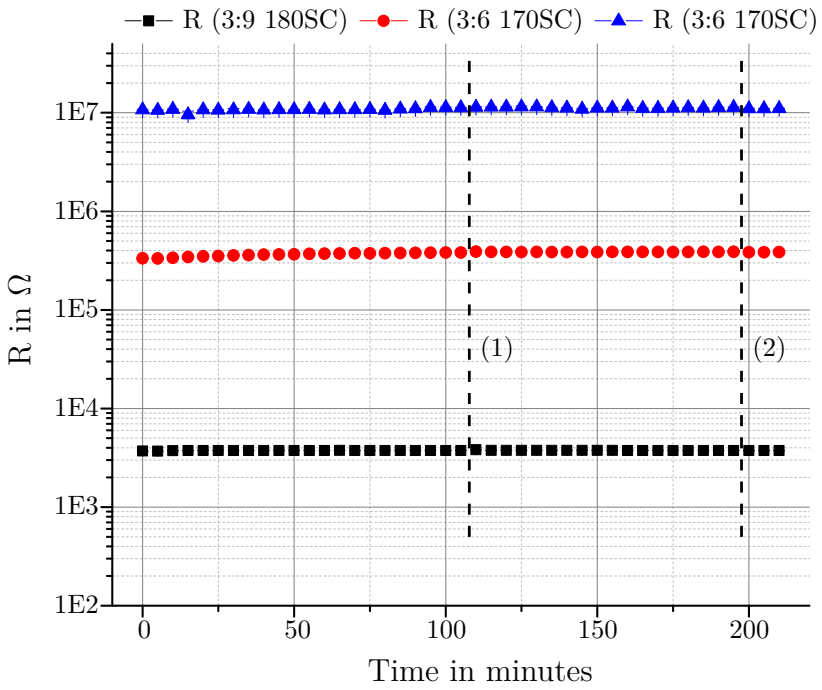

Figure 4.18: Testing of three already broken 3D structures with "3:9 180SC" and "3:6 170SC" composites (cross-sections are exposed to the ambient conditions): measured resistances in the dry state until immersing the broken structures into tempered NaCl-solution (wet state) in (1) and in the dry state again, after taking the structures out of the solution in (2). There is no detectable change in the resistance signals for tested structures.

These unsuccessful results can be explained regarding the yield of previously characterised sensor structures from wafers 1, 2, 3 and 4 with various ALD com-

posites. As presented in Figure 4.8, most structures with high initial resistances did not show a positive response to the application of a water droplet. Thus, a similar yield was expected in the characterisation of 3D structures. Based on the curves in Figures 4.17 and 4.18, it is assumed that the applied ALD composites of these structures demonstrate high initial resistances, but do not react sensitively to the aqueous solution. Thereby, the measured resistances remain unchanged during the tests.

An expected behaviour of the sensor signal, similar to the positive responses of sensitive sensor structures in Chapter 4.1.3, could be observed in Figure 4.19.

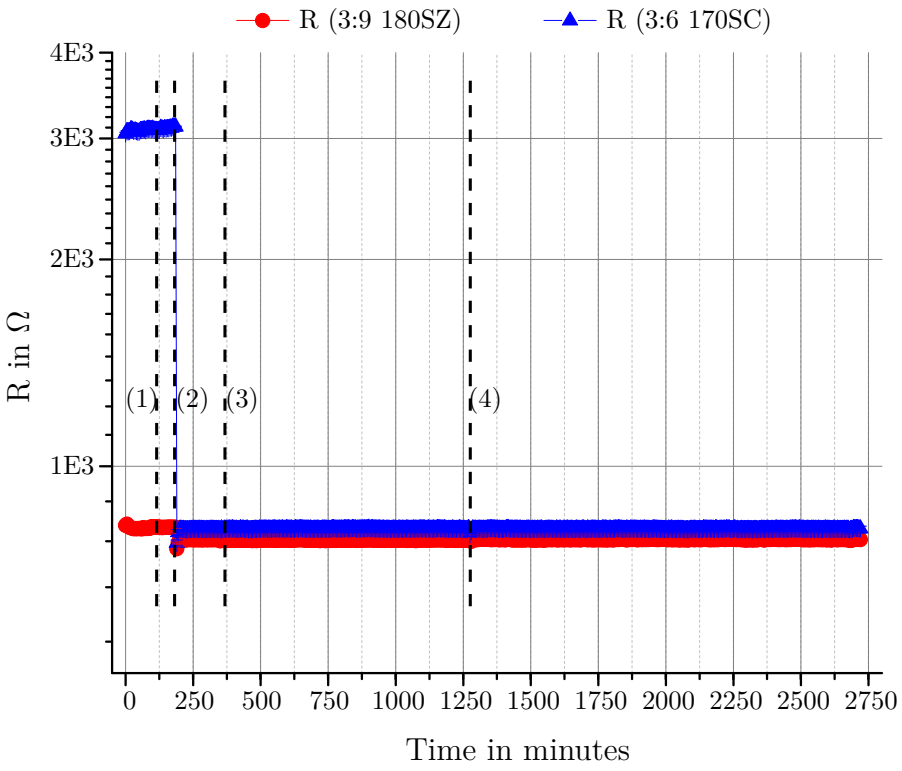

Figure 4.19: Testing of two 3D structures with "3:9 180SC" and "3:6 170SC" composites: measured resistances in the dry state, after immersing the structures into the tempered NaCl-solution (wet state) in (1) and after scratching the surface and directly immersing again in (2). After a certain period of time, the structures are taken out of the solution (3) and immersed again in (4). Both resistance values demonstrate steep decrease after immersion with damaged encapsulation. The resulting values do not change any more (independent of ambient conditions).

Further structures with with "3:9 180SC" (red curve) and "3:6 170SC" composites (blue curve) were tested in the dry state first and immersed into tempered NaCl-solutions after 120 min (1). After a further 60 min, structures were taken out of the solution, scratched on the surface by tweezers (2) and immediately immersed again into the NaCl-solution. A steep decrease of both curves could be monitored. For the red curve, the decrease amounts to 5 %. For the blue curve, the decrease even amounts to 74 %. These values remain after taking the structures out of the solution after 190 min (3) and also after immersing them again another 900 min later in (4).
The results presented in Figure 4.19 demonstrate more successful responses of the composite layers to the wet environment. The changes in resistance are expected in exactly this way. The stable values during the first immersion into the NaCl-solution confirms the sealing properties of the thin Ta_2O_5 layer. Only the intentional damaging of the encapsulation layers enables the interaction of sensitive composite and H_2O molecules within the solution. Also as expected, the resistance values remain low and do not increase again, even if the structures are subsequently stored and measured in the dry state. These few structures represent the sensor structures from Figure 4.8, which showed high initial resistances and also sensitivity in case of water droplet application.

Implementation of the developed encapsulation concept on 3D substrates has been successfully accomplished on several circuit boards (mostly without parylene F coating). Due to the complex handling of the single structures, which needed to be clamped and released from an aluminum bracket for each deposition step of the process flow, process errors, such as impurities and resulting defective layer growth occurred. These errors resulted in short circuits between the electrode layers characterised by too small initial resistances (below 800 Ω). As a result, many structures had to be sorted out.
Only structures with initial resistances above 800 Ω were considered for further investigations in the presented test set-up in which they have been tested both in the dry and wet state, as well as with and without damaged encapsulations. According to the yield of previously tested sensor structures (see Chapter 4.1.3), the 3D structures also demonstrated negative and positive responses to the immersion into NaCl-solution with exposed ALD composite. Resistance curves of

structures in Figure 4.17 and 4.18 did not show any changes despite interaction of aqueous solution with exposed composite layers, while resistance curves of structures in Figure 4.19 demonstrated clear and irreversible sensitivity.
Two sensitive structures with "3:9" and "3:6" composites layers were found in the final characterisation. None of the structures with the "2:8" composite showed an appropriate sensitivity even though this composite demonstrated the best yield during the characterisation of sensor structures (see Figure 4.8). That is why the non-sensitivity of structures with the "2:8" composite is justified with processing issues and the overall poor yield. A reliable comparison of which composite reacted most sensitively cannot be made because of the small number of tested structures and even smaller number of structures which showed expected sensitivity.

These results prove the successful implementation of a three-dimensional encapsulation stack with an integrated humidity-detecting ALD composite layer between two electrode layers. In case of a defect in the encapsulation, so that aqueous solutions can interact with the humidity-sensitive composite, the conductivity of the composite increases significantly which can be detected by monitoring the resistance and can be interpreted as a sign of incipient degradation of the encapsulation.

5 Conclusion and Outlook

5.1 Conclusion

In this thesis an advanced 3D concept for the encapsulation of active implants was developed. The advanced concept is based on a component level encapsulation in order to guarantee minimised encapsulation volume. The encapsulation consists of a stack of CVD and ALD thin film layers. For the first time the integration of an all-round enclosing humidity sensor layer which serves for immediate detection of moisture within the encapsulation stack has been demonstrated. Thus, the encapsulation provides self-monitoring of its own quality.

Main developments of this thesis are the three-dimensional application of thin films, contacting two 3D metal layers with the implant circuit board without using photo-lithographic structuring and the implementation of a humidity-sensitive ALD composite.

The deposition of a 3 to 5 µm thick parylene F film by a highly isotropic CVD process isolated the electronic components and smoothed sharp edges on the surface of the substrate. Coating tests on simplified silicon circuit boards, partly equipped with ASICs, have shown an all-around encapsulation of the three-dimensional substrate. Successful tape-tests have proven sufficient adhesion of the parylene F on the substrate surface.

Contacting the 3D electrode layers was achieved by sequential forming of via openings in the dielectric layers (directly on top of corresponding contact pads on the circuit board) and isotropic ALD of the electrode material. Thus, ILCs are achieved automatically between the exposed contact pads and the conductive electrode layers. As photo-lithographic structuring was not possible on die level, a single laser ablation process with a UV laser was utilised for local removal of dielectric material. The via opening procedures (with various laser wavelengths and

cut sizes) are integrated into the whole process flow of the encapsulation concept. Comparable ILC at via openings, which were generated by photo-lithographic structuring and etching processes, were fabricated and evaluated. Although ILC-resistances at laser ablated via openings were higher by a factor of almost 2000, these resistances are still appropriate considering the later application of monitoring the sensor layer paramaters.

The development of a humidity-sensitive ALD film required compositions of dielectric Al_2O_3 and semiconducting ZnO grains which can be formed by the island growth behaviour of ALD processes with small numbers of deposition cycles. The increasing conductivity of the semiconducting ZnO in case of water molecule adsorption was detected through the increasing current and decreasing resistance of the composite between two electrode layers. The limiting number of deposition cycles for island growth was determined using TOF-SIMS. Additionally, the GPC of the composites was estimated by cross-sectional SEM. The homogeneity of the distribution of dielectric Al_2O_3 and semiconducting ZnO grains was determined by sheet resistance measurements. Sensor structures with two electrodes enclosing various ALD composites were fabricated and tested in a test set-up with a constant test voltage in which the sensor current was monitored in the dry state and during the application and the evaporation of a water droplet. Four various ALD recipes were tested in which the grain sizes of ZnO and Al_2O_3 grains varied and the ratios 1 : 2, 1 : 1, 1 : 3 and 1 : 4 were chosen. The application of the water droplet on the perforated top electrode allowed the adsorption of water molecules at the ZnO grain boundaries of the composite resulting in a change of the current (and also resistance) by one to five orders of magnitude. The first wafer (with a ZnO to Al_2O_3 ratio of 1 : 2) demonstrated only five sensitive sensor structures while the second wafer (ratio 1 : 1) did not show any sensitive structures at all. This poor yield could be improved by decreasing the ratio to 1 : 3 on wafer 3 and 1 : 4 on wafer 4 which both demonstrated twice the number of sensitive structures.

In the implementation of the encapsulation stack on three-dimensional circuit boards, with and without parylene F coating, the recipes with ratios 1 : 2, 1 : 3 and 1 : 4 were considered. Cross-sectional SEM presented sufficient step coverage of each applied encapsulation layer at various positions of the 3D substrates. Finally, the encapsulated substrates were tested in the dry state and in the wet state

in which they were immersed into tempered NaCl-solution. Each encapsulated 3D structure demonstrated unchanged resistance values in both states. Additionally, intentional damaging of the thin ALD layers by scratching the surface with tweezers in the dry state was performed so that the sensitive composites were exposed. A second immersion into NaCl-solution resulted in a significant and irreversible decrease of the measured resistance (up to about 70 % of the initial value) for two encapsulated 3D substrates utilising the composite with the ZnO to Al_2O_3 ratios 1 : 2 and 1 : 3. This work demonstrated the feasibility of implementing an advanced implant encapsulation concept which not only consists of a hermetic thin film sealing but also a humidity detecting and all-around enclosing sensor layer for real time monitoring of the encapsulation quality.

5.2 Outlook

The feasibility of a hermetic implant encapsulation with humidity-detecting function as self-monitoring feature is proven successfully. The functionality of the developed encapsulation can be further improved by the following aspects.

1. Increasing the yield of the functional 3D structures
2. Complete encapsulation of the implantable device (without exposed interface to measuring instruments)
3. Wireless readout of the sensor parameters, required for implantation

For the implementation of point 1, the process flow of the encapsulation stack needs to be improved. In this work, the structures were handled manually before and after the parylene F coating, for clamping and releasing from the aluminum bracket before and after each ALD step and for each laser ablation step for opening the contact pads for the bottom and top electrodes. If these steps could be unexceptionally performed in the clean room, only one bracket and one clamping and releasing step would be necessary for the whole implementation without any need for further manual handling. This would reduce the level of contamination and the number of mechanically generated defects on the 3D substrate. Additionally, the homogeneity of the ALD composites needs to be improved so that more sensitive areas can be fabricated. The circular arrangement of precursor lines of

the here used ALD system used and the associated inflexible flow rates during each deposition cycle is assumed to cause the observed inhomogeneity. Therefore, the saturation of the substrate surface with precursor molecules should be achieved in a more uniform way, for example by laminar flow from top to bottom onto the substrate (possibly through a perforated plate). A homogeneous distribution of ZnO and Al_2O_3 grains leads to larger sensitive areas of the composite. At least, technical obstacles which occurred during this work, need to be overcome. Mainly, issues regarding ALD process deviations, such as deposition temperatures and growth behaviour of Ru, and also inadequate temperature stability of the parylene F have to be solved for future work.
For the implementation of point 2, the number of CVD and ALD processes in the process flow needs to be at least doubled. Areas, which served to fix the 3D substrates within the process chambers are uncoated after the first deposition step and need be coated in a second step. Although this will lead to varying thicknesses of the single layers at different positions of the substrate, it would not hinder the application and functionality of the developed encapsulation stack.
For the implementation of point 3, the sensor structure needs to be connected to a signal processing ASIC, so that resistance measurements can be done without additional external measuring devices. In case of a wireless communication with the implant, information about the degradation of the implant encapsulation could be send to an extracorporeal reading unit.

If point 1, 2 and 3 can be solved, the newly presented concept for a 3D implant encapsulation with self-monitoring function and wireless readout can find use on two-dimensional ASIC surfaces or three-dimensional devices which need hermetic sealing in various applications fields, such as the biomedical, automotive or consumer industry.

Appendix

Some sensors on the wafers 1, 2, 3 and 4 showed small leakage currents and corresponding resistances in the upper GΩ-range even up to 24 V during the first characterisations by means of IV measurements.

In Figure 5.1, all presented sensors show leakage currents of up to 10 nA below 5 V. An increase in currents above the nA range can only be detected from 17 V onwards. Corresponding resistances are in the range of GΩ.

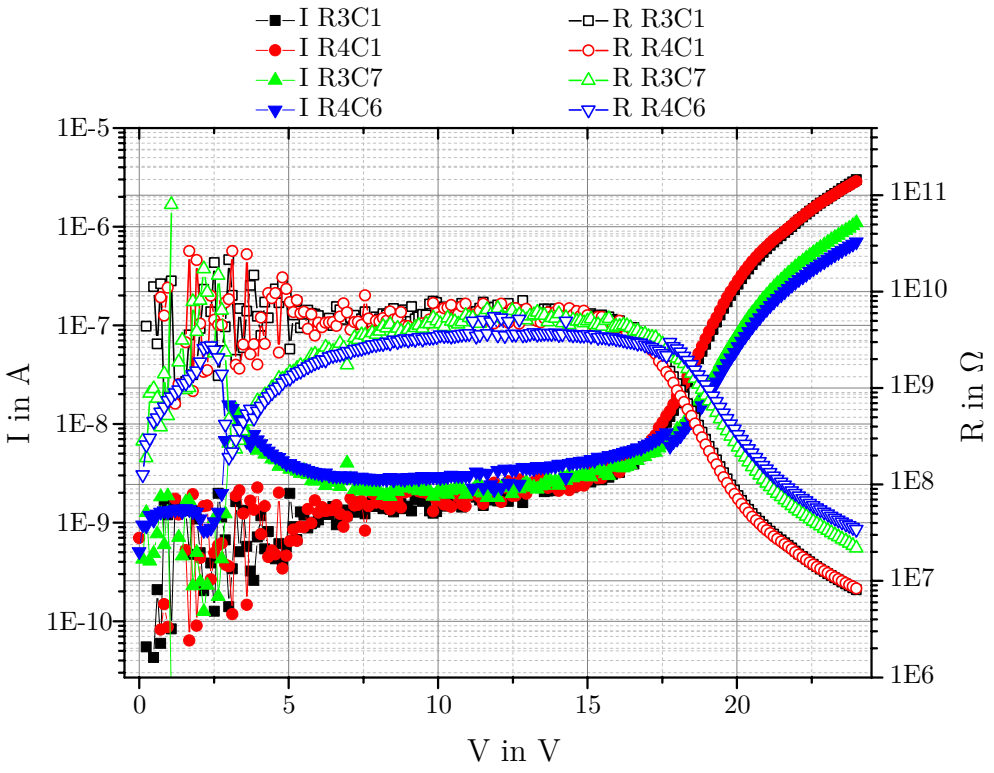

Figure 5.1: Examples of successfully tested sensors (with ALD composite "ZnO+Al_2O_3 3:6 85SC") in the IV measurements with a voltage sweep of up to 24 V. Below 17 V, leakage currents (presented in the left y-axis) are in the range of nA, while calculated resistances (presented in the right y-axis) are in the range of 3 GΩ to 10 GΩ.

In Figure 5.2, up to 15 V, leakage currents do not exceed 6 nA which results in corresponding resistances of up to 10 GΩ. The gradients of the currents at elevated voltages (above 15 V) are almost identical, which suggests a very comparable composition of the humidity-sensitive layers between the electrodes in the first column.

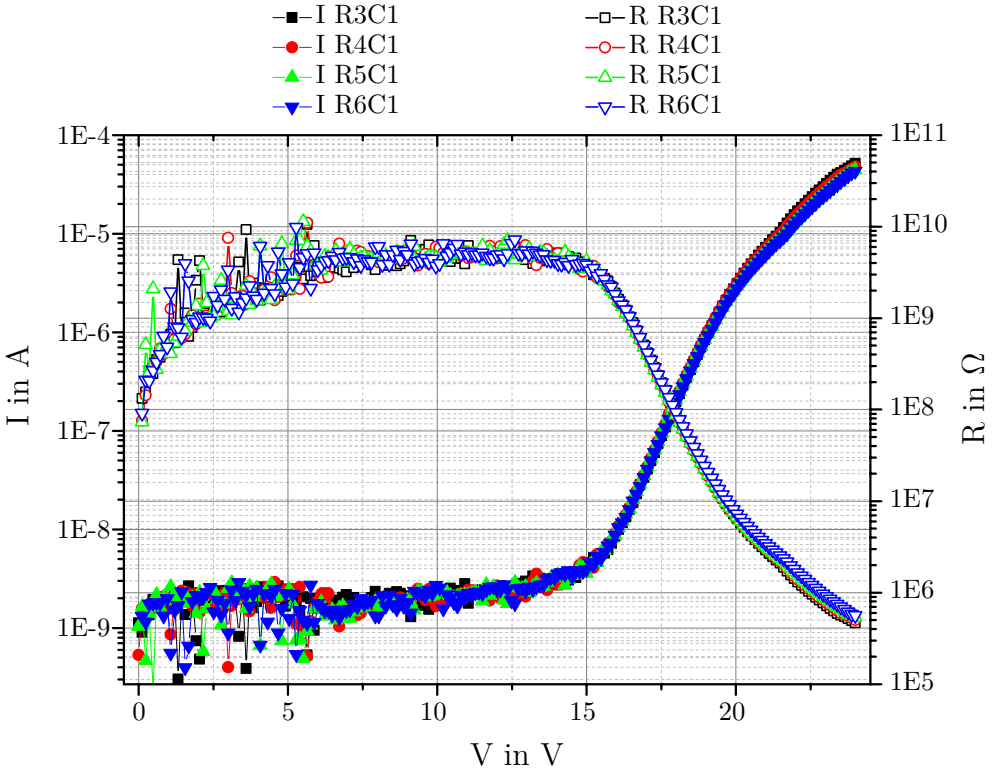

Figure 5.2: Examples of successfully tested sensors (with ALD composite "ZnO+Al_2O_3 4:4 92SC") in the IV measurements with a voltage sweep of up to 24 V. Below 16 V, leakage currents (presented in the left y-axis) are in the range of nA, while calculated resistances (presented in the right y-axis) are in the range of 2 GΩ to 8 GΩ.

By increasing the amount of Al_2O_3 grains, and respectively decreasing the amount of ZnO grains, the monitored current curves with respect to increasing test voltages demonstrate a smaller positive gradient. This leads to leakage current of only several nA at voltages up to 18 V for the positive sensor examples of the wafer with the ALD composite "ZnO+Al_2O_3 3:9 75SC", presented in Figure 5.3.

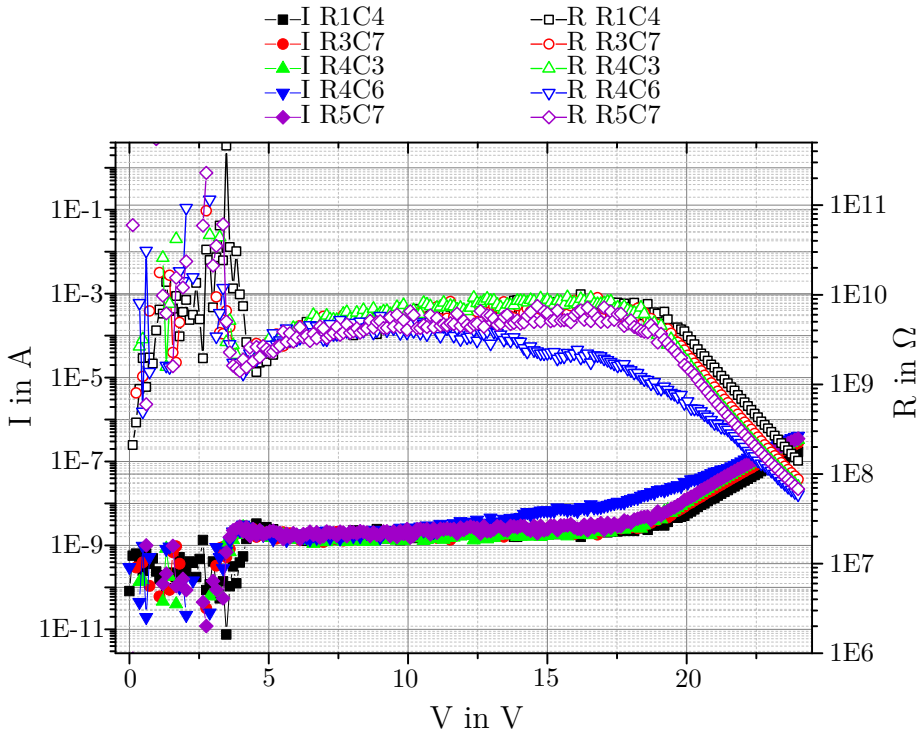

Figure 5.3: Examples of successfully tested sensors (with ALD composite "ZnO+Al_2O_3 3:9 75SC") in the IV measurements with a voltage sweep of up to 24 V. Below 18 V, leakage currents (presented in the left y-axis) are in the range of nA, while calculated resistances (presented in the right y-axis) are in the range of 2 GΩ to 10 GΩ.

The observation made in Figure 5.3 can also be seen in Figure 5.4. The even smaller ratio of ZnO grains to Al_2O_3 grains in the tested composite "ZnO+Al_2O_3 2:8 90SC" leads to leakage currents of below 10 nA at voltages up to even 22 V. The gradients of measured current and calculated resistance curves are clearly smaller than in the previous graphics.

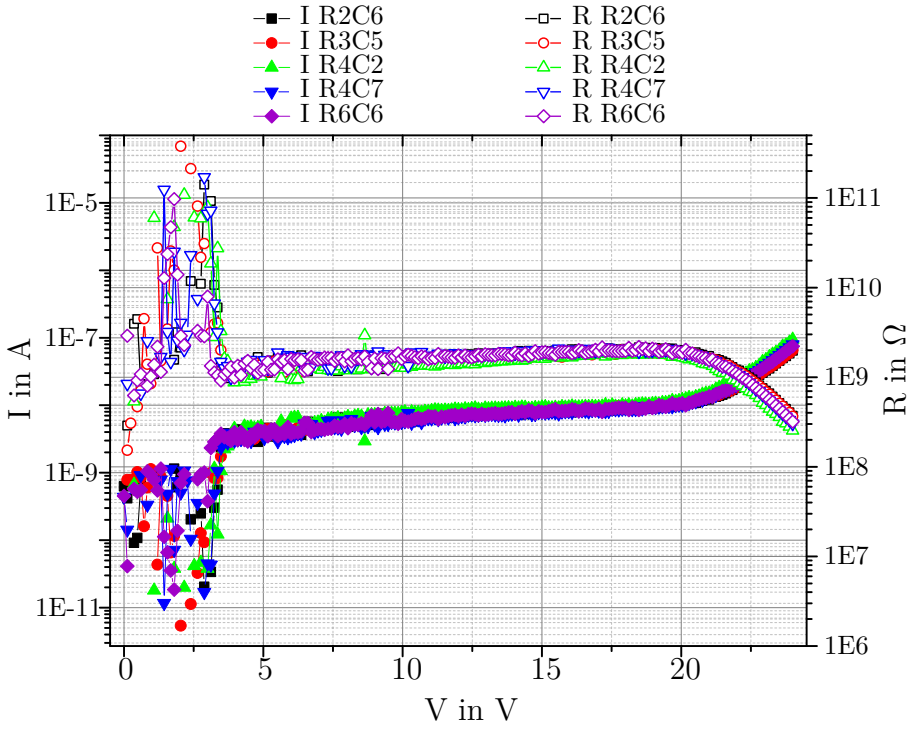

Figure 5.4: Examples of successfully tested sensors (with ALD composite "ZnO+Al_2O_3 2:8 90SC") in the IV measurements with a voltage sweep of up to 24 V. Below 22 V, leakage currents (presented in the left y-axis) are in the range of nA, while calculated resistances (presented in the right y-axis) are in the range of 1 GΩ to 3 GΩ.

Even though numerous sensor structures with all types of ALD composite showed high initial resistances, most of these structures, both sensitive and non-sensitive ones, failed a second IV measurement after the application of a water droplet. After initially demonstrating very low leakage currents at test voltages of up to 24 V, these structures now show currents in the range of mA at already 1 V and cannot be used as a humidity detecting sensor. Some examples are presented in 5.5 and 5.6 for sensors of wafer 1 and 2 and in 5.7 and 5.8 for sensors of wafer 3 and 4. All of these sensors are previously tested ones which showed high resistances and small leakage currents in the dry state before the water droplet was applied. The demonstrated changes of sensor structure characteristics could not be reversed by drying process, such as tempering at 100 °C for two hours. The irreversible change of the electrical properties of the composites tested can be explained by the reduction of semiconducting ZnO grains to more conductive Zn particles during the droplet application. For more detailed description of the chemical reactions see Chapter 4.1.3.

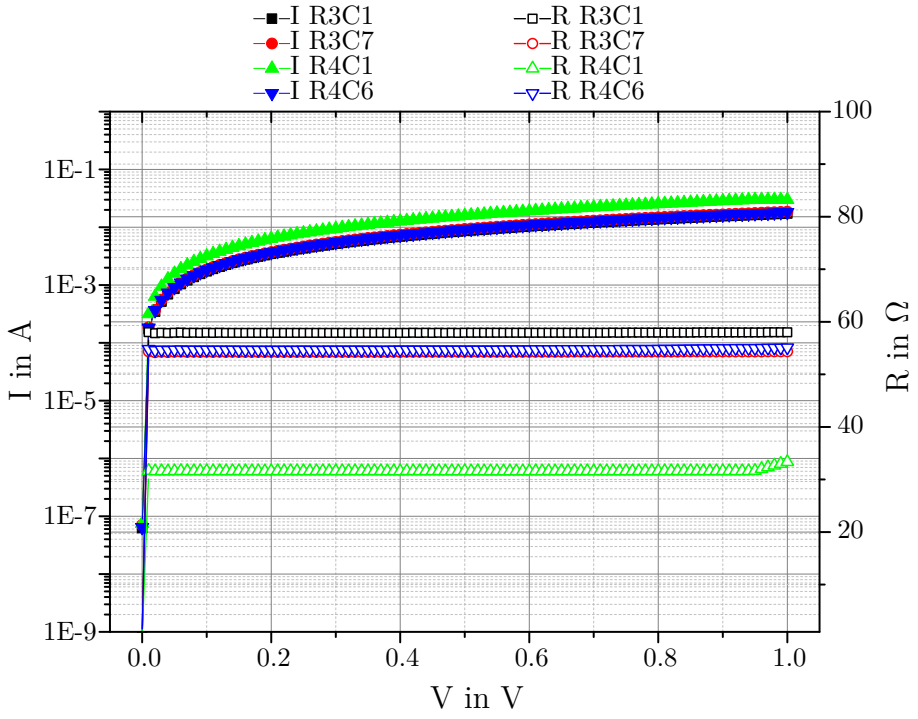

Figure 5.5: IV curves of sensor structures (3:6 85SC) with previously high-ohmic behaviour, presenting leakage currents up to several mA at only 1 V after the water droplet test.

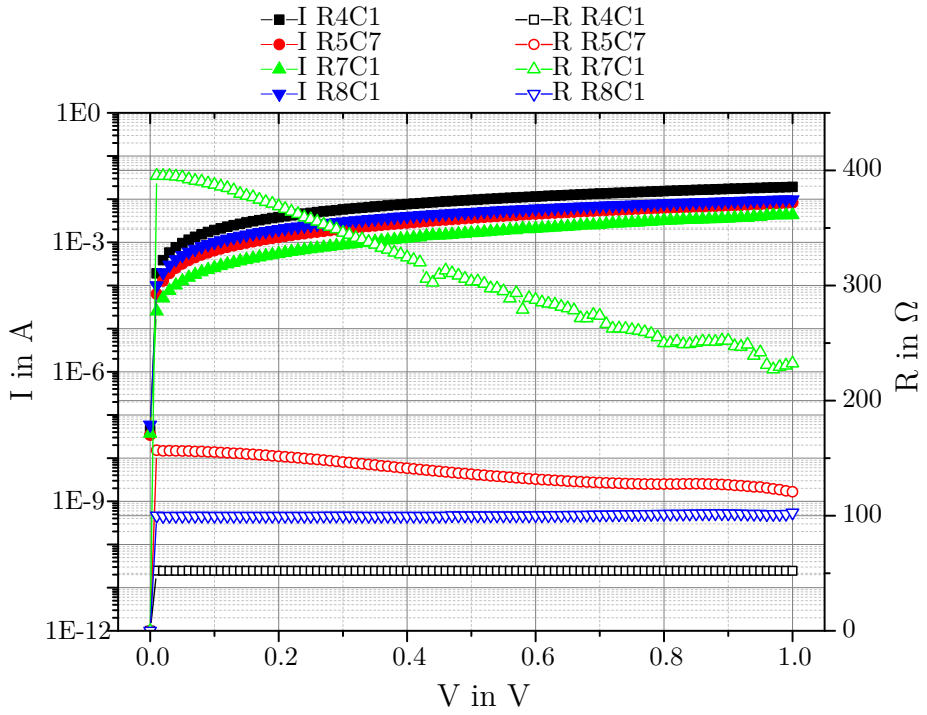

Figure 5.6: IV curves of sensor structures (4:4 92SC) with previously high-ohmic behaviour, presenting leakage currents up to several mA at only 1 V after the water droplet test.

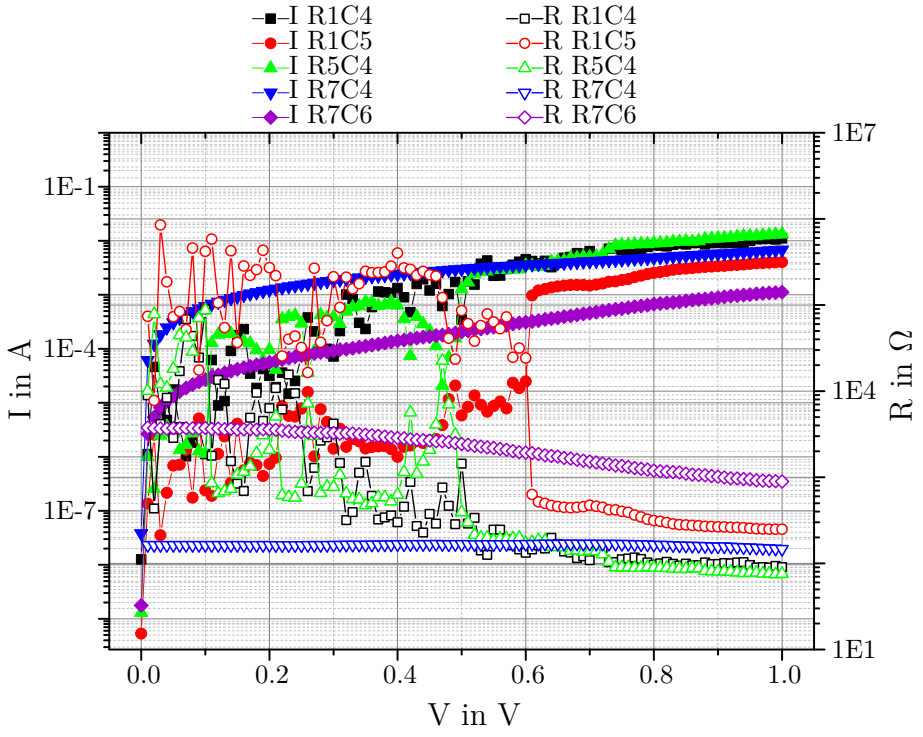

Figure 5.7: IV curves of sensor structures (3:9 75SC) with previously high-ohmic behaviour, presenting leakage currents up to several mA at only 1 V after the water droplet test.

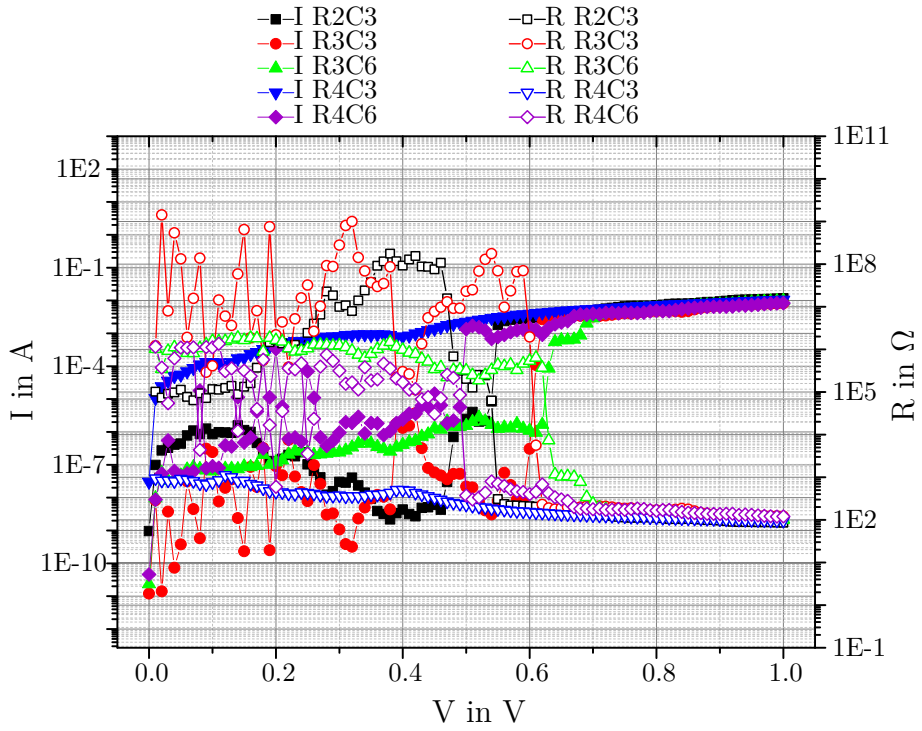

Figure 5.8: IV curves of sensor structures (2:8 90SC) with previously high-ohmic behaviour, presenting leakage currents up to several mA at only 1 V after the water droplet test.

Own Publications

Peer-Reviewed Journal Articles

Ö. Dogan, C. Walk, J. Weidenmüller, P. Gembaczka, A. Stanitzki, M. Görtz, 'Development of a System Concept for Miniaturized Cardiovascular Multi Sensor Implants', *Procedia Engineering*, 168 (2016) 159 - 162.

J. Weidenmüller, **Ö. Dogan**, C. Walk, P. Gembaczka, A. Stanitzki, M. Görtz, 'Telemetric Multi-sensor system for Medical Applications - The Approach', *tm - Technisches Messen*, 84 (1) (2017) 53 - 58.

J. Weidenmüller, **Ö. Dogan**, A. Stanitzki, M. Baum, T. Schröder, T. Wünsch, M. Görtz, A. Grabmaier, 'Implantable Multi Sensor System for Hemodynamic Controlling', *tm - Technisches Messen*, 85 (5) (2018) 359 - 365.

Ö. Dogan, A. Buschhausen, C. Walk, W. Mokwa, H. Vogt, 'Development of a post-CMOS compatible Nanoporous Thin Film Layer based on Al_2O_3', *IOP Conf. Ser.: Mater. Sci. Eng.*, 350 (2018) 012001.

Conference Proceedings

Ö. Dogan, W. Mokwa, L. Mai, A. Devi, H. Vogt, 'Die-Level Patterning of Parylene F by Laser-Ablation for Further Processing with ALD Functional Films', *Smart Systems Integration (SSI), Proc.*, 12 (2018) Dresden, 392 - 395.

C. Walk, **Ö. Dogan**, M. Görtz, W. Mokwa, H. Vogt, 'Post-CMOS MEMS Capacitive Pressure Sensor: Porous ALD Membrane for Sacrificial Layer Release and Diaphragm Sealing', *Smart Systems Integration (SSI), Proc.*, 12 (2018) Dresden, 86 - 93.

Ö. Dogan, M. Görtz, W. Mokwa, H. Vogt, '3D applicable ALD Film for Humidity Detection', *Smart Systems Integration (SSI), Proc.*, 13 (2019) Barcelona, 309 - 312.

Ö. Dogan, N. Schierbaum, J. Weidenmüller, M. Baum, T. Schröder, D. Wünsch, M. Görtz, K. Seidl, 'Miniaturized Multi Sensor Implant for monitoring of Hemodynamic Parameters', *Annual International Conference of the IEEE Engineering in Medicine and Biology Society (EMBC)*, 41 (2019) Berlin, 3823 - 3826.

Bibliography

[1] Mouly, J. ; Siri, A.: Connected medical devices 2017 - The internet of medical things (From Technologies to market). In: *Yole Developement Reports* (2017)

[2] Dudaicevs, H. ; Kandler, M. ; Manoli, Y. ; Mokwa, W. ; Spiegel, E.: Surface micromachined pressure sensors with integrated CMOS readout electronics. In: *Sensors and Actuators A: Physical* 43 (1994), Nr. 1-3, S. 157163

[3] Trieu, H. ; Knier, M. ; Koster, O. ; Kappert, H. ; Schmidt, M. ; Mokwa, W.: Monolithic integrated surface micromachined pressure sensors with analog on-chip linearization and temperature compensation. In: *Micro Electro Mechanical Systems (MEMS 2000), The Thirteenth Annual International Conference*, 2000, S. 547–550

[4] Trieu, H. ; Kordas, N. ; Mokwa, M.: Fully CMOS compatible capacitive differential pressure sensors with on-chip programmabilities and temperature compensation. In: *Proc. of IEEE Sensors, vol. 2*, 2002, S. 1451 – 1455

[5] Walk, C. ; Göhlich, A. ; Giese, A. ; Vogt, H. ; Kraft, M.: Investigation of diaphragm deflection of an absolute MEMS capacitive polysilicon pressure sensor. In: *Proc. SPIE, vol. 9517*, 2015, S. 95170

[6] Betz, W.: *Flexible mikroelektromechanische Implantate für den chronischen Einsatz: Verkapselungskonzepte und Testverfahren für die Materialcharakterisierung*, Universität Duisburg Essen, Diss., 2011

[7] Vogt, M. ; Hauptmann, R.: Plasma-deposited passivation layers for moisture and water protection. In: *Surface and Coatings Technology* 74 (1995), Nr. 1-3, S. 676681

[8] Wiberg, N. ; Hollemann, A. F. ; E., Wiberg: *Lehrbuch der anorganische Chemie, 102nd ed.* Gruyter, 2007. – ISBN 3110177706

[9] Treager, R.: Nonhermeticity of Polymeric Lid Sealants. In: *IEEE Transactions on Party, Hybrids, and Packaging* 13 (1977), S. 147–152. http://dx.doi.org/https://doi.org/10.1109/TPHP.1977.1135193. – DOI https://doi.org/10.1109/TPHP.1977.1135193

[10] Jiang, G. ; Zhou, D. D. ; Zhou, D. (Hrsg.) ; Greenbaum, E. (Hrsg.): *Implantable Neural Prostheses 2 - Technology Advances and Challanges in Hermetic Packaging for Implantable Medical Devices*. Springer, 2010. – 27–61 S. http://dx.doi.org/10.1007/978-0-387-98120-8. http://dx.doi.org/10.1007/978-0-387-98120-8

[11] Medtronic: *Micra Transcatheter Pacing System.* http://www.medtronic.com/de-de/patienten/produkte-therapien/pacemaker/micra-kleiner-herzschrittmacher-elektroden.html : online, March 2016

[12] Loeb, G. E. ; Peck, R. A. ; Singh, J. ; Kim, Y.-H. ; Deshpande, S. ; Baker, L. L. ; Bryant, J. T.: Mechanical loading of rigid intramuscular implants. In: *Biomedical Microdevices* 9 (2007), Dec, Nr. 6, 901–910. http://dx.doi.org/10.1007/s10544-006-9031-5. – DOI 10.1007/s10544–006–9031–5. – ISSN 1572–8781

[13] MEDEL: *PULSAR Cochlear Implant.* http://www.medel.com/history/ : online, 2004

[14] Mokwa, W. ; Görtz, M.: Intelligente Implantate Geringere Abmessungen bei höherer Komplexität und Funktionalität. In: *Technik in Bayern - Mikrosystemtechnik* (2017), September, S. 16–17

[15] Todani, A. ; Behlau, I. ; Fava, M. A. ; Cade, F. ; Cherfan, D. G. ; Zakka, F. R. ; Jakobiec, F. A. ; Gao, Y. ; Dohlman, C. H. ; Melki, S. A.: Intraocular Pressure Measurement by Radio Wave Telemetry. In: *Investigative Ophthalmology and Visual Science* 52 (2011), Nr. 13, S. 9573. http://dx.doi.org/10.1167/iovs.11-7878. – DOI 10.1167/iovs.11–7878

[16] Stieglitz, Thomas: Manufacturing, assembling and packaging of miniaturized neural implants. In: *Microsystem Technologies* 16 (2010), May, Nr. 5, 723-734. http://dx.doi.org/10.1007/s00542-009-0988-x. – DOI 10.1007/s00542–009–0988–x. – ISSN 1432–1858

[17] Betz, W. ; Trieu, H.K. ; Vogt, H.: Microelectromechanical Implants: Encapsulation Concepts and Test Procedures. In: *Biomedical Engineering/Biomedizinische Technik* 57 (2012), Nr. SI-1 Track-D, S. 914–914

[18] Gembaczka, P.: Encapsulation of implantable integrated MEMS pressure sensors using polyimide epoxy composite and atomic layer deposition. In: *Journal of Sensors and Sensor Systems* 3 (2014), S. 335–347

[19] Xie, X. ; Rieth, L. ; Merugu, S. ; Tathireddy, P. ; Solzbacher, F.: Plasma-assisted atomic layer deposition of Al2O3 and parylene C bi-layer encapsulation for chronic implantable electroncs. In: *Allpied Physics Letters* 101 (2012), August, S. 093702–1 – 093702–5. http://dx.doi.org/http://dx.doi.org/10.1063/1.4748322. – DOI http://dx.doi.org/10.1063/1.4748322

[20] Kuppusami, S. ; Oskouei, R. H.: Parylene coatings in medical devices and implants: a review. In: *Univ. J. Biomed. Eng* 3 (2015), 9–14. http://dx.doi.org/10.13189/ujbe.2015.030201. – DOI 10.13189/ujbe.2015.030201

[21] Weinmann, M. ; Nisch, W. ; Stett, A. ; Bucher, V. ; Urban, G.: Langzeitstabile Verkapselungsschichten mit integriertem Feuchtesensor für aktive Mikroimplantate. In: *WOMag* (2012), December. http://dx.doi.org/10.7395/2012/Weinmann1. – DOI 10.7395/2012/Weinmann1

[22] Weinmann, M. ; Huck, J.: Flexible Verkapselungsschichten für elektrisch aktive Mikroimplantate. In: *Galvanotechnik* 2 (2014), S. 254–262

[23] Weinmann, M. ; Nisch, W.: Monitored Water Vapour Barrier Coatings for Flexible Micro-Implants. In: *Biomed Tech*, 2013

[24] Martin, D. ; Silmy, K.: Neue Technologien zum Korrosionsschutz von Medizinprodukten. In: *Journal für Oberflächentechnik* 55 (2015), S. 53–55

[25] Dokmeci, M. ; Najafi, K.: A high-sensitivity polyimide capacitive relative humidity sensor for monitoring anodically bonded hermetic micropackages. In: *Microelectromechanical Systems, Journal of* 10 (2001), Jun, Nr. 2, S. 197–204. http://dx.doi.org/10.1109/84.925735. – DOI 10.1109/84.925735. – ISSN 1057–7157

[26] Harpster, T. J. ; Hauvespre, S. ; Dokmeci, M. R. ; Najafi, K.: A passive humidity monitoring system for in situ remote wireless testing of micropackages. In: *Microelectromechanical Systems, Journal of* 11 (2002), Feb, Nr. 1, S. 61–67. http://dx.doi.org/10.1109/84.982864. – DOI 10.1109/84.982864. – ISSN 1057–7157

[27] Harpster, T. J. ; Nikles, S.A. ; Dokmeci, M. R. ; Najafi, K.: Long-term hermeticity and biological performance of anodically bonded glass-silicon implantable packages. In: *Device and Materials Reliability, IEEE Transactions on* 5 (2005), Sept, Nr. 3, S. 458–466. http://dx.doi.org/10.1109/TDMR.2005.854374. – DOI 10.1109/TDMR.2005.854374. – ISSN 1530–4388

[28] Metzen, R.P. von ; Stieglitz, T.: A Wireless System for Monitoring Polymer Encapsulations. In: *Engineering in Medicine and Biology Society, 2007. EMBS 2007. 29th Annual International Conference of the IEEE*, 2007. – ISSN 1557–170X, S. 6600–6603

[29] Dogan, Ö. ; Walk, C. ; Weidenmüller, J. ; Gembaczka, P. ; Stanitzki, A. ; Görtz, M.: Development of a system concept for miniaturized cardiovascular multi sensor implants. In: *Eurosensors 2016 - Procedia Engineering*, Elsevier Open Access Journal, September 2016, S. 159 162

[30] Weidenmüller, J. ; Walk, C. ; Dogan, Ö. ; Gembaczka, P. ; Stanitzki, A. ; Görtz, M.: Telemetric multi-sensor system for medical applications - the approach. In: *TM - Technisches Messen* 1 (2017), S. 53 – 58. http://dx.doi.org/10.1515/teme-2016-0036. – DOI 10.1515/teme–2016–0036

[31] Weidenmüller, J. ; Dogan, Ö. ; Stanitzki, A. ; Baum, M. ; Schröder, T. J. ; Wünsch, D. ; Görtz, M. ; Grabmaier, A.: Implantable multi sensor system for hemodynamic controlling. In: *Technisches Messen* 5

(2016), S. 359 365. http://dx.doi.org/10.1515/teme-2017-0116. – DOI 10.1515/teme–2017–0116

[32] Kulwicki, B. M.: Humidity Sensors. In: *Journal of the American Ceramic Society* 74 (1991), Nr. 4, 697–708. http://dx.doi.org/10.1111/j.1151-2916.1991.tb06911.x. – DOI 10.1111/j.1151–2916.1991.tb06911.x. – ISSN 1551–2916

[33] Traversa, E.: Ceramic sensors for humidity detection: the state-of-the-art and future developments. In: *Sensors and Actuators B: Chemical* 23 (1995), Nr. 2, 135 - 156. http://dx.doi.org/https://doi.org/10.1016/0925-4005(94)01268-M. – DOI https://doi.org/10.1016/0925–4005(94)01268–M. – ISSN 0925–4005. – The workshop on new developments in semiconducting gas sensors

[34] Chen, Z. ; Lu, C.: Humidity Sensors: A Review of Materials and Mechanisms. In: *Sensor Letters* 3 (2005), July, S. 274–295

[35] Farahani, H. ; Wagiran, R. ; Hamidon, M. N.: Humidity Sensors Principle, Mechanism, and Fabrication Technologies: A Comprehensive Review. In: *Sensors* 14 (2014), Nr. 5, 7881. http://dx.doi.org/10.3390/s140507881. – DOI 10.3390/s140507881. – ISSN 1424–8220

[36] Yamazoe, N. ; Shimizu, Y.: Humidity sensors: Principles and applications. In: *Sensors and Actuators* 10 (1986), Nr. 3, 379 - 398. http://dx.doi.org/http://dx.doi.org/10.1016/0250-6874(86)80055-5. – DOI http://dx.doi.org/10.1016/0250–6874(86)80055–5. – ISSN 0250–6874

[37] Korotcenkov, G.: *Handbook of Gas Sensor Materials: Properties, Advantages and Shortcomings for Applications Volume 2: New Trends and Technologies*. Springer New York, 2013 (Integrated Analytical Systems). https://books.google.de/books?id=kC28BAAAQBAJ. – ISBN 9781461473886

[38] Seiyama, T. ; Yamazoe, N. ; Arai, H.: Ceramic humidity sensors. In: *Sensors and Actuators* 4 (1983), 85 - 96. http://dx.doi.org/http://dx.doi.org/10.1016/0250-6874(83)85012-4. – DOI http://dx.doi.org/10.1016/0250–6874(83)85012–4. – ISSN 0250–6874

[39] Hertl, W. ; Hair, M. L.: Hydrogen bonding between adsorbed gases and surface hydroxyl groups on silica. In: *The Journal of Physical Chemistry* 72 (1968), Nr. 13, 4676-4682. http://dx.doi.org/10.1021/j100859a053. – DOI 10.1021/j100859a053

[40] Thiel, P. A. ; Madey, T. E.: The interaction of water with solid surfaces: Fundamental aspects. In: *Surface Science Reports* 7 (1987), Nr. 6, 211 - 385. http://dx.doi.org/https://doi.org/10.1016/0167-5729(87)90001-X. – DOI https://doi.org/10.1016/0167–5729(87)90001–X. – ISSN 0167–5729

[41] Nitta, T. ; Hayakawa, S.: Ceramic Humidity Sensors. In: *IEEE Transactions on Components, Hybrids, and Manufacturing Technology* 3 (1980), S. 237 – 243

[42] Agmon, Noam: The Grotthuss mechanism. In: *Chemical Physics Letters* 244 (1995), Nr. 5, 456 - 462. http://dx.doi.org/https://doi.org/10.1016/0009-2614(95)00905-J. – DOI https://doi.org/10.1016/0009–2614(95)00905–J. – ISSN 0009–2614

[43] Wraight, Colin A.: Chance and design - Proton transfer in water, channels and bioenergetic proteins. In: *Biochimica et Biophysica Acta (BBA) - Bioenergetics* 1757 (2006), Nr. 8, 886 - 912. http://dx.doi.org/https://doi.org/10.1016/j.bbabio.2006.06.017. – DOI https://doi.org/10.1016/j.bbabio.2006.06.017. – ISSN 0005–2728. – Proton Transfer Reactions in Biological Systems

[44] Wang, C. ; Yin, L. ; Zhang, L. ; Xiang, D. ; Gao, R.: Metal Oxide Gas Sensors: Sensitivity and Influencing Factors. In: *Sensors* 10 (2010), March, Nr. 3, S. 2088–2106. http://dx.doi.org/10.3390/s100302088. – DOI 10.3390/s100302088

[45] Boyle, J. F. ; Jones, K. A.: The effects of CO, water vapor and surface temperature on the conductivity of a SnO2 gas sensor. In: *Journal of Electronic Materials* 6 (1977), Nov, Nr. 6, 717–733. http://dx.doi.org/10.1007/BF02660346. – DOI 10.1007/BF02660346. – ISSN 1543–186X

[46] Advani, G. N. ; Nanis, L.: Effects of humidity on hydrogen sulfide detection by SnO2 solid state gas sensors. In: *Sensors and Actuators* 2 (1981), Nr. Supplement C, 201 - 206. http://dx.doi.org/https://doi.org/10.1016/0250-6874(81)80039-X. – DOI https://doi.org/10.1016/0250–6874(81)80039–X. – ISSN 0250–6874

[47] Nenov, T. G. ; Yordanov, S. P.: *Ceramic Sensors: Technology and Applications*. Technomic Publishing Company, Inc., 1996. – 15 – 69 S. – Chapter 2: Physical-Chemical and Technoogical Principles of Ceramic Sensors

[48] Morrison, S. R.: Semiconductor gas sensors. In: *Sensors and Actuators* 2 (1981), 329 - 341. http://dx.doi.org/https://doi.org/10.1016/0250-6874(81)80054-6. – DOI https://doi.org/10.1016/0250–6874(81)80054–6. – ISSN 0250–6874

[49] Liang, Q. ; Xu, H. ; Zhao, J. ; Gao, S.: Micro humidity sensors based on ZnO-In2O3 thin films with high performances. In: *Sensors and Actuators B: Chemical* 165 (2012), Nr. 1, 76 - 81. http://dx.doi.org/http://dx.doi.org/10.1016/j.snb.2012.02.019. – DOI http://dx.doi.org/10.1016/j.snb.2012.02.019. – ISSN 0925–4005

[50] O'Halloran, G. M. ; Sarro, P. M. ; Groeneweg, J. ; Trimp, P. J. ; French, P. J.: A bulk micromachined humidity sensor based on porous silicon. In: *Solid State Sensors and Actuators, 1997. TRANSDUCERS '97 Chicago., 1997 International Conference on* Bd. 1, 1997, S. 563–566 vol.1

[51] O'Halloran, G.M.: *Capacitive Humidity Sensor based on Porous Silicon*, Technische Universiteit Delft, Diss., September 1999

[52] Puurunen, R. L. ; Putkonen, M. ; Tilli, Markku (Hrsg.): *Handbook of Silicon Based MEMS Materials and Technologies*. Elsevier Science, 2015. – 154 – 163 S.

[53] Ritala, M. ; Niinisto, J. ; Krumdieck, S. ; Chalker, P. ; Aspinall, H. ; Pemble, M. E. ; Gladfelter, W. L. ; Leese, B. ; Fischer, R. A. ; Parala, H. ; Kanjolia, R. ; Dupuis, R. D. ; Alexandrov, S. E. ; Irvine, S.

J. C. ; Palgrave, R. ; Parkin, I. P. ; Jones, Anthony C. (Hrsg.) ; Hitchman, Michael L. (Hrsg.): *Overview of Chemical Vapour Deposition*. The Royal Society of Chemistry, 2009. – 1–36 S. http://dx.doi.org/10.1039/9781847558794. http://dx.doi.org/10.1039/9781847558794. – ISBN 978–0–85404–465–8

[54] Parylene, VSi: *Parylene thin film coating process*. https://vsiparylene.com/parylene-advantages/process/ : online, January 2018

[55] Gorham, William F.: A New, General Synthetic Method for the Preparation of Linear Poly-p-xylylenes. In: *Journal of Polymer Science Part A-1: Polymer Chemistry* 4 (1966), Nr. 12, 3027–3039. http://dx.doi.org/10.1002/pol.1966.150041209. – DOI 10.1002/pol.1966.150041209. – ISSN 1542–9350

[56] Rodger, D. C. ; Li, W. ; Weiland, J. D. ; Humayun, M. S. ; Tai, Y.-C. ; Takahata, K. (Hrsg.): *Advances in Micro/Nano Electromechanical Systems and Fabrication Technologies*. InTech, 2013. – 1 – 40 S. http://dx.doi.org/10.5772/55308. http://dx.doi.org/10.5772/55308

[57] Puurunen, Riikka L.: Surface chemistry of atomic layer deposition: A case study for the trimethylaluminum/water process. In: *Journal of Applied Physics* 97 (2005), Nr. 12, -. http://dx.doi.org/http://dx.doi.org/10.1063/1.1940727. – DOI http://dx.doi.org/10.1063/1.1940727

[58] Ritala, Mikko ; Niinistö, Jaako ; Jones, A. C. (Hrsg.) ; Hitchman, M. L. (Hrsg.): *Atomic Layer Deposition*. Royal Society of Chemistry, 2009. – 158–206 S.

[59] Bohr, M. T. ; Chau, R. S. ; Ghani, T. ; Mistry, K.: The High-k Solution. In: *IEEE Spectrum* 44 (2007), Oct, Nr. 10, S. 29–35. http://dx.doi.org/10.1109/MSPEC.2007.4337663. – DOI 10.1109/MSPEC.2007.4337663. – ISSN 0018–9235

[60] Puurunen, R. L. ; Vandervorst, W.: Island growth as a growth mode in atomic layer deposition: A phenomenological model. In: *Journal of Ap-*

plied Physics 96 (2004), Nr. 12, 7686-7695. http://dx.doi.org/10.1063/1.1810193. – DOI 10.1063/1.1810193

[61] Muneshwar, T. ; Cadien, K.: Probing initial-stages of ALD growth with dynamic in situ spectroscopic ellipsometry. In: *Applied Surface Science* 328 (2015), 344 - 348. http://dx.doi.org/http://dx.doi.org/10.1016/j.apsusc.2014.12.044. – DOI http://dx.doi.org/10.1016/j.apsusc.2014.12.044. – ISSN 0169–4332

[62] Assaud, L. ; Hanbücken, M. ; Santinacci, L.: Atomic Layer Deposition of TiN/Al2O3/TiN nanolaminates for capacitor applications. In: *ECS Transactions 50* 13 (2012), S. 151–157

[63] Ghazaryan, L. ; Kley, E.-B. ; Tünnermann, A. ; Szeghalmi, A.: Nanoporous SiO2 thin films made by atomic layer deposition and atomic etching. In: *Nanotechnology* 27 (2016), Nr. 25, 255603. http://stacks.iop.org/0957-4484/27/i=25/a=255603

[64] Mane, A. U. ; Elam, J. W.: Nanostructured composite thin films with tailored resistivity by atomic layer deposition. In: *Proc.SPIE* 8818 (2013), 8818 - 8818 - 7. http://dx.doi.org/10.1117/12.2024482. – DOI 10.1117/12.2024482

[65] Dietz, Dorothee: *Entwicklung eines Hochtemperatur-Trench-Kondensators mit Hilfe von Methoden der Atomlagenabscheidung*, Universität Duisburg-Essen, Diss., June 2017

[66] Fischer, A. C. ; Mäntysalo, M. ; Niklaus, F. ; Tilli, Markku (Hrsg.): *Handbook of Silicon Based MEMS Materials and Technologies*. Elsevier Science, 2015. – 550 – 564 S.

[67] Leitz, K.-H. ; Redlingshöfer, B. ; Reg, Y. ; Otto, A. ; Schmidt, M.: Metal Ablation with Short and Ultrashort Laser Pulses. In: *Physics Procedia* 12 (2011), 230 - 238. http://dx.doi.org/https://doi.org/10.1016/j.phpro.2011.03.128. – DOI https://doi.org/10.1016/j.phpro.2011.03.128. – ISSN 1875–3892. – Lasers in Manufacturing 2011 - Proceedings of the Sixth International WLT Conference on Lasers in Manufacturing

[68] Martyniuk, J. ; Corbett, S. ; Loeb, G.: Innovative Laser System for Ultraviolet Laser-Based Micromachining. In: *Medical Device & Dignostic Industry* (1994), October, S. 110–121

[69] Schmidt, E. M. ; Bak, M. J. ; Christensen, P.: Laser exposure of Parylene-C insulated microelectrodes. In: *Journal of Neuroscience Methods* 62 (1995), Nr. 1, 89 - 92. http://dx.doi.org/https://doi.org/10.1016/0165-0270(95)00060-7. – DOI https://doi.org/10.1016/0165–0270(95)00060–7. – ISSN 0165–0270

[70] Schmiedel, C. ; Schmiedel, A. ; Viöl, W.: Combined Plasma Laser Removal of Parylene Coatings. In: *International Symposium on Plasma Chemistry* Bd. 19, 2009

[71] Sedky, S. ; Witvrouw, A. ; Bender, H. ; Baert, K.: Experimental determination of the maximum post-process annealing temperature for standard CMOS wafers. In: *IEEE Transactions on Electron Devices* 48 (2001), Feb, Nr. 2, S. 377–385. http://dx.doi.org/10.1109/16.902741. – DOI 10.1109/16.902741. – ISSN 0018–9383

[72] Takeuchi, H. ; Wung, A. ; Sun, X. ; Howe, R. T. ; King, T. J.: Thermal budget limits of quarter-micrometer foundry CMOS for post-processing MEMS devices. In: *IEEE Transactions on Electron Devices* 52 (2005), Sept, Nr. 9, S. 2081–2086. http://dx.doi.org/10.1109/TED.2005.854287. – DOI 10.1109/TED.2005.854287. – ISSN 0018–9383

[73] Polytec PT GmbH (Hrsg.): *Polytec EP 642-frozen*. EttlingerStraße 30 , 76307 Karlsbad , Germany: Polytec PT GmbH, January 2017

[74] Plasma Parylene Systems (PPS) GmbH (Hrsg.): µ *Parylene Coatings*. https://www.plasmaparylene.de/index.php: Plasma Parylene Systems (PPS) GmbH, 2011

[75] Para Tech (Hrsg.): *Parylene Properties*. parylene.com: Para Tech, 2017

[76] Specialty Coating Systems (SCS) (Hrsg.): *SCS Parylene Properties*. https://scscoatings.com/de/: Specialty Coating Systems (SCS), 2015

[77] Meng, E. ; Li, P.-Y. ; Tai, Y.-C.: Plasma removal of Parylene C. In: *Journal of Micromechanics and Microengineering* 18 (2008), February, Nr. 045004. http://dx.doi.org/10.1088/0960-1317/18/4/045004. – DOI 10.1088/0960–1317/18/4/045004

[78] Xie, X. ; Rieth, L. ; Caldwell, R. ; Diwekar, M. ; Tathireddy, P. ; Sharma, R. ; Solzbacher, F.: Long-term bilayer encapsulation performance of atomic layer deposited Al2O3 and Parylene C for biomedical implantable devices. In: *IEEE Trans Biomed Eng.* 60(10) (2013), S. 2943–2951

[79] Heicks, Rudolf: *Parylene Coating.* Am Schwarzen Weg 25-31, 59590 Geseke, Germany : online, 2017

[80] New Wave Research (Hrsg.): *EzLaze II - Laser Cutting System for Semiconductor Failure Analysis.* New Wave Research Co. Ltd., Suite B Oak Park Business Centre Alington Road Eynesbury, St Neots Cambs PE19 6WA, England, UK: New Wave Research

[81] Lee, C.-Y. ; Lin, C.-H. ; Fu, L.-M. ; Leondes, Cornelius T. (Hrsg.): *MEMS/NEMS: Handbook Techniques and Applications.* Boston, MA : Springer US, 2006. – 1055–1084 S. http://dx.doi.org/10.1007/0-387-25786-1_27. http://dx.doi.org/10.1007/0-387-25786-1_27. – ISBN 978–0–387–25786–0

[82] Nenov, T. G. ; Yordanov, S. P.: *Ceramic Sensors: Technology and Applications.* Technomic Publishing Company, Inc., 1996. – 71 – 131 S. – Chapter 3: Cermic Humidty Sensors

[83] Wang, H. A. ; Kröger, F. A.: Pore formation during oxidative annealing of Al2O3-:Fe and slowing of grain growth by precipitates and pores. In: *Journal of Materials Science* 15 (1980), Aug, Nr. 8, 1978–1986. http://dx.doi.org/10.1007/BF00550623. – DOI 10.1007/BF00550623. – ISSN 1573–4803

[84] Furlan, K. P. ; Pasquarelli, R. M. ; Krekeler, T. ; Ritter, M. ; Zierold, R. ; Nielsch, K. ; Schneider, G. A. ; Janssen, R.:

Highly porous alpha-Al2O3 ceramics obtained by sintering atomic layer deposited inverse opals. In: *Ceramics International* 43 (2017), Nr. 14, 11260 - 11264. http://dx.doi.org/http://dx.doi.org/10.1016/j.ceramint.2017.05.176. – DOI http://dx.doi.org/10.1016/j.ceramint.2017.05.176. – ISSN 0272–8842

[85] Malm, J. ; Sahramo, E. ; Perälä, J. ; Sajavaara, T. ; Karppinen, M.: Low-temperature atomic layer deposition of ZnO thin films: Control of crystallinity and orientation. In: *Thin Solid Films* 519 (2011), Nr. 16, 5319 - 5322. http://dx.doi.org/http://dx.doi.org/10.1016/j.tsf.2011.02.024. – DOI http://dx.doi.org/10.1016/j.tsf.2011.02.024. – ISSN 0040–6090

[86] Pal, D. ; Singhal, J. ; Mathur, A. ; Singh, A. ; Dutta, S. ; Zollner, S. ; Chattopadhyay, S.: Effect of substrates and thickness on optical properties in atomic layer deposition grown ZnO thin films. In: *Applied Surface Science* 421 (2017), S. 341 – 348. http://dx.doi.org/https://doi.org/10.1016/j.apsusc.2016.10.130. – DOI https://doi.org/10.1016/j.apsusc.2016.10.130. – ISSN 0169–4332. – 7th International Conference on Spectroscopic Ellipsometry

[87] Mross, Stefan: *Integrated Multi-Sensor System for Parallel In-Situ Monitoring of Biotechnological Processes*, Universität Duisburg-Essen, Diss., 2016

[88] Herrán, J. ; Fernández, I ; Ochoteco, E. ; Cabañero, G ; Grande, H.: The role of water vapour in ZnO nanostructures for humidity sensing at room temperature. In: *Sensors and Actuators B: Chemical* 198 (2014), 239 - 242. http://dx.doi.org/http://dx.doi.org/10.1016/j.snb.2014.03.043. – DOI http://dx.doi.org/10.1016/j.snb.2014.03.043. – ISSN 0925–4005

[89] Qi, Q. ; Zhang, T. ; Yu, Q. ; Wang, R. ; Zeng, Y. ; Liu, L. ; Yang, H.: Properties of humidity sensing ZnO nanorods-base sensor fabricated by screen-printing. In: *Sensors and Actuators B: Chemical* 133 (2008), Nr. 2, 638 - 643. http://dx.doi.org/http://dx.doi.org/10.1016/j.snb.2008.03.035. – DOI http://dx.doi.org/10.1016/j.snb.2008.03.035. – ISSN 0925–4005

[90] Matero, R. ; Ritala, M. ; Leskelä, M. et a.: Atomic layer deposited thin films for corrosion protection. In: *J. Phys. IV France* 09 (1999), 493-499. http://dx.doi.org/10.1051/jp4:1999862. – DOI 10.1051/jp4:1999862

[91] Hartsough, L.D.: Resistivity of bias-sputtered TiW films. In: *Thin Solid Films* 64 (1979), Nr. 1, 17 - 23. http://dx.doi.org/https://doi.org/10.1016/0040-6090(79)90536-4. – DOI https://doi.org/10.1016/0040–6090(79)90536–4. – ISSN 0040–6090. – International Conference on Metallurgical Coatings, San Diego, 1979-Part III

[92] Li, H. ; Farmer, D. B. ; Gordon, R. G. ; Lin, Y. ; Vlassak, J.: Vapor Deposition of Ruthenium from an Amidinate Precursor. In: *Journal of The Electrochemical Society* 154 (2007), S. 642–647. http://dx.doi.org/10.1149/1.2789294. – DOI 10.1149/1.2789294

[93] Dogan, Ö. ; Mokwa, W. ; Mai, L. ; Devi, A. ; Vogt, H.: Die-Level Patterning of Parylene F by Laser-Ablation for further Processing with ALD Functional Layers. In: *Smart System Integration (SSI) 2018 - Conference Proceedings*, 2018

[94] Dogan, Ö. ; Buschhausen, A. ; Walk, C. ; Mokwa, W. ; Vogt, H.: Development of a Post-CMOS Compatible Nanoporous Thin Film layer Based on Al2O3. In: *IOP Conference Series: Materials Science and Engineering* 350 (2018), Nr. 1, 012001. http://stacks.iop.org/1757-899X/350/i=1/a=012001

[95] Shackelford, James F. et a. ; Shackelford, James F. (Hrsg.) ; Alexander, W. (Hrsg.): *Materials Science and Engineering Handbook, p.565*. CRC Press LLC, 2001. – 565 S.

[96] Shetty, Amitha ; Nanda, Karuna K.: Synthesis of zinc oxide porous structures by anodization with water as an electrolyte. In: *Applied Physics A* 109 (2012), Oct, Nr. 1, 151–157. http://dx.doi.org/10.1007/s00339-012-7023-2. – DOI 10.1007/s00339–012–7023–2. – ISSN 1432–0630

[97] Warzecha, Marek: *Energie & Umwelt*. Bd. 207: *Zinkoxid: Einfluss von Dotierung und Legierung auf elektro-optische Eigenschaften, auf das*

Ätzverhalten und auf die Tempernachbehandlung. Forschungszentrum Jülich GmbH, 2014. – 26 – 27 S.

[98] In: VANÝSEK, Petr: *Electrochemical Series*. 93. Chemical Rubber Company, 2012, S. 5 – 80